RL-TR-93-34
Final Technical Repor
April 1993

AD-A267 052

ALTERNATIVE OPTICAL ARCHITECTURES FOR MULTICHANNEL ADAPTIVE OPTICAL PROCESSING

Dynetics, Inc.

R.J. Berinato, M.C. Zari, and M.C. Budge, Jr.

DTIC
ELECTE
JUL 20 1993
S E D

APPROVED FOR PUBLIC RELEASE; DISTRIBUTION UNLIMITED.

93-16350

Rome Laboratory
ir Force Materiel Command
iiss Air Force Base, New York

This report has been reviewed by the Rome Laboratory Public Affairs Office (PA) and is releasable to the National Technical Information Service (NTIS). At NTIS it will be releasable to the general public, including foreign nations.

RL-TR-93-34 has been reviewed and is approved for publication.

APPROVED: Christopher W. Keefer

CHRISTOPHER W. KEEFER, Captain, USAF
Project Engineer

FOR THE COMMANDER:

JAMES W. YOUNGBERG, Lt Col, USAF
Deputy Director
Surveillance and Photonics Directorate

If your address has changed or if you wish to be removed from the Rome Laboratory mailing list, or if the addressee is no longer employed by your organization, please notify RL (OCPA) Griffiss AFB NY 13441. This will assist us in maintaining a current mailing list.

Do not return copies of this report unless contractual obligations or notices on a specific document require that it be returned.

REPORT DOCUMENTATION PAGE

Form Approved
OMB No. 0704-0188

Public reporting burden for this collection of information is estimated to average 1 hour per response, including the time for reviewing instructions, searching existing data sources, gathering and maintaining the data needed, and completing and reviewing the collection of information. Send comments regarding this burden estimate or any other aspect of this collection of information, including suggestions for reducing this burden, to Washington Headquarters Services, Directorate for Information Operations and Reports, 1215 Jefferson Davis Highway, Suite 1204, Arlington, VA 22202-4302, and to the Office of Management and Budget, Paperwork Reduction Project (0704-0188), Washington, DC 20503.

1. AGENCY USE ONLY (Leave Blank)	2. REPORT DATE	3. REPORT TYPE AND DATES COVERED
	April 1993	Final Jan 92 - Oct 92

4. TITLE AND SUBTITLE
ALTERNATIVE OPTICAL ARCHITECTURES FOR MULTICHANNEL ADAPTIVE OPTICAL PROCESSING

5. FUNDING NUMBERS
C - F30602-92-C-0026
PE - 62702F
PR - 4600
TA - P1
WU - PG

6. AUTHOR(S)
R.J. Berinato, M.C. Zari, M.C. Budge, Jr.

7. PERFORMING ORGANIZATION NAME(S) AND ADDRESS(ES)
Dynetics, Inc.
P.O. Drawer B
Huntsville AL 35814-5050

8. PERFORMING ORGANIZATION REPORT NUMBER
TR-92-RL-0026-184

9. SPONSORING/MONITORING AGENCY NAME(S) AND ADDRESS(ES)
Rome Laboratory (OCPA)
25 Electronic Parkway
Griffiss AFB NY 13441-4515

10. SPONSORING/MONITORING AGENCY REPORT NUMBER
RL-TR-93-34

11. SUPPLEMENTARY NOTES
Rome Laboratory Project Engineer: Capt Christopher W. Keefer/OCPA/(315)330-2944.

12a. DISTRIBUTION/AVAILABILITY STATEMENT
Approved for public release; distribution unlimited.

12b. DISTRIBUTION CODE

13. ABSTRACT (Maximum 200 words)

This final report describes the continued design and hardware implementation of an acousto-optic (AO) multichannel adaptive optical processor (MADOP) for application to the cancellation of multipath jamming interference in advanced surveillance radars. The work described in this report was performed for the Photonics Center at Rome Laboratory and represents the second year of Dynetics support on this project. The objective of this effort was the continued fabrication and performance characterization of a multichannel adaptive system that can perform cancellation of multiple wideband (10 MHz) interference sources in the presence of multipath. Specific activities included 1) the simulation of convergence performance of the MADOP algorithms against a variety of multipath conditions, 2) the reconfiguration of the multichannel AO time-integrating correlator for improved stability, 3) the refinement of the AO tapped delay line to achieve better frequency response, 4) the development of the radio frequency interface between the two AO subsystems, and 5) the design and development of a single-loop electronic canceller for improved phase stability after the AO tapped delay line system.

14. SUBJECT TERMS
adaptive processing, acousto-optics, optical signal processing

15. NUMBER OF PAGES 154

16. PRICE CODE

17. SECURITY CLASSIFICATION OF REPORT	18. SECURITY CLASSIFICATION OF THIS PAGE	19. SECURITY CLASSIFICATION OF ABSTRACT	20. LIMITATION OF ABSTRACT
UNCLASSIFIED	UNCLASSIFIED	UNCLASSIFIED	UNLIMITED

TABLE OF CONTENTS

Page

1. INTRODUCTION 1-1

2. ALGORITHM SIMULATION AND RESULTS 2-1

   2.1 BLOCK-LEAST MEAN SQUARE (LMS) SIMULATION 2-1

   2.2 OPTICAL JAMMING CANCELLER (OJC) SIMULATION MODIFICATIONS 2-7

   2.3 IMPLICATIONS TO THE MADOP DESIGN 2-10

3. MADOP IMPLEMENTATION PROGRESS 3-1

   3.1 TIME-INTEGRATING CORRELATION FOR WEIGHT FUNCTION CALCULATION 3-1

   3.2 AOTDL FILTER 3-17

4. MADOP SYSTEM TESTING 4-1

   4.1 MULTIPATH SIGNAL SIMULATION FOR SINGLE-STEP, OPEN-LOOP OPERATION 4-1

   4.2 CANCELLATION PERFORMANCE 4-1

   4.3 SYSTEM STABILIZATION WITH A SINGLE-LOOP ELECTRONIC CANCELLER 4-14

   4.4 RECOMMENDED WEIGHT FUNCTION CALCULATION ALGORITHM 4-19

5. CONCLUSIONS AND RECOMMENDATIONS 5-1

APPENDIX A. ANALOG DESIGNS FOR SINGLE-LOOP ELECTRONIC CANCELLER A-1

   A.1 ANALOG SINGLE-LOOP ELECTRONIC CANCELLER A-1

   A.2 TUNABLE LPF DESIGN A-6

APPENDIX B. APPLIED OPTICS DRAFT PAPER B-1

APPENDIX C. MATLAB SOFTWARE C-1

REFERENCES R-1

LIST OF ILLUSTRATIONS

Figure	Title	Page
2-1	Model of the Multipath Scenario	2-2
2-2	Cancellation for Multipath in Main Channel But Not Auxiliary Channel	2-4
2-3	Cancellation for Multipath in Auxiliary Channel But Not in Main Channel	2-5
2-4	IIR Filtering	2-6
3-1	Preliminary Multichannel Time-Integrating Correlator Layout	3-2
3-2	Signal Distribution Network	3-4
3-3	Noise Autocorrelation	3-5
3-4	Signal Generation/Distribution Network for Multipath Simulation $\Delta\tau_1 = -0.1\ \mu s$, $\Delta\tau_2 = +0.4\ \mu s$, $\Delta\tau_3 = +1.0\ \mu s$	3-6
3-5	Multichannel Correlation with Multipath	3-8
3-6	Multichannel Time-Integrating Correlator Layout	3-9
3-7	Distorted Correlation Pattern for 80-MHz Tone	3-10
3-8	Acoustic Aperture Arrangements Resulting in Distorted Correlation Fringes	3-10
3-9	Correlation Fringes After AO Cell Angular Adjustments	3-11
3-10	Dynamic Range Test Signal Generation Layout	3-13
3-11	Dynamic Range Testing	3-14
3-12	Range Window Calibration with Two-Tone DSB-SC Correlation (f = 2.15 MHz)	3-16
3-13	System Frequency Response for Various AOSLM Input Frequencies	3-17
3-14	Simulated Two-Tap System Frequency Response	3-19
3-15	Measured Two-Tap System Frequency Response	3-20
3-16	Measured AOTDL Delay Versus AOSLM Frequency	3-21
3-17	Diffracted AOSLM Beams for Longitudinal TeO_2 (Aperture = 21.1 × 22.2 mm)	3-22
3-18	Diffracted AOSLM Beams for Slow-Shear TeO_2 (Aperture = 15.4 × 26.0 mm)	3-23
4-1	Single-Step, Open-Loop Signal Generation	4-2

LIST OF ILLUSTRATIONS (Concluded)

Figure	Title	Page
4-2	AOTDL Input Path Response	4-3
4-3	Two-Tone Signal Input	4-4
4-4	AOTDL Input Path Spectrum for Two-Tone Signal Input Shown in ***Figure 4-3***	4-5
4-5	Manual Cancellation Performance	4-7
4-6	Splitter/Combiner Cancellation Performance	4-10
4-7	Pulse Cancellation (τ = 500 ns, PRI = 3 µs, A = 200 mVp-p, 100 mV Offset)	4-11
4-8	Pulse Cancellation (τ = 200 ns, PRI = 3 µs, A = 200 mVp-p, 100 mV Offset)	4-12
4-9	Pulse Cancellation (τ = 100 ns, PRI = 3 µs, A = 200 mVp-p, 100 mV Offset)	4-13
4-10	Single-Step, Open-Loop Operation - Reference + AOTDL Output (~30 dB Cancellation at 82.15 MHz)	4-15
4-11	Phase Stability Effects on Signal Cancellation	4-16
4-12	Classical Single-Weight LMS Loop	4-17
4-13	Implementation of a Complex Weight	4-18
4-14	Single-Loop Electronic Canceller to Cancel Effects of Carrier Drift	4-18
4-15	Simulink Structure for Single-Loop Electronic Canceller Simulation	4-20
4-16	Simulated Single-Loop Electronic Canceller Performance	4-21
4-17	Enhanced Peak Picking Results	4-23
4-18	Noisy Peak Picking Results	4-24
A-1	Canceller Block Diagram	A-2
A-2	Circuit Diagram of Canceller	A-3
A-3	Circuit Diagram of Canceller as Implemented by Photonics Center Personnel	A-4
A-4	Error Signal Circuit	A-5
A-5	MF6CN-50 Diagrams	A-7
A-6	LH0033G Connection Diagram	A-10
A-7	LPF Design	A-10

LIST OF TABLES

Table	Title	Page
3-1	Differential Delays (BAW Devices)	3-3
A-1	Pin Descriptions	A-9

DTIC QUALITY INSPECTED 5

Accesion For
NTIS CRA&I ☒
DTIC TAB ☐
Unannounced ☐
Justification

By
Distribution /

Availability Codes

Dist	Avail and / or Special
A-1	

(Reverse Blank)

LIST OF ABBREVIATIONS

ac	alternating current
AGC	automatic gain control
AO	acousto-optic
AOSLM	AO spatial light modulator
AOTDL	AO tapped delay line
AR	autoregressive
BAW	bulk acoustic wave
CCD	charge-coupled device
CMOS	complementary metal oxide semiconductor
CVDL	continuously variable delay line
dc	direct current
DSB/SC	double sideband/suppressed carrier
ESE	Expert in Science and Engineering
FFT	fast Fourier transform
FIR	finite impulse response
i&Q	in-phase and quadrature
IF	intermediate frequency
IIR	infinite impulse response
LMS	least mean square
LPF	low-pass filter
MA	moving average
MADOP	Multichannel Adaptive Optical Processor
OCPA	Photonics Center - Rome Laboratory
OJC	optical jamming canceller
RF	radio frequency
S/N	signal to noise
TDL	tapped delay line
TTL	transistor-transistor logic

Units of Measure

A/W	amps per watt
dB	decibels
dBm	decibels referenced to one milliwatt
°/deg	degrees
ft	feet
Hz	hertz
in	inches
kHz	kilohertz
kΩ	kilohms
m	meters
mA	milliamps
MHz	megahertz
mm	millimeters
ms	milliseconds
m/s	meters per second
μF	microFarads
μs	microseconds
mW	milliwatts

LIST OF ABBREVIATIONS (Concluded)

ns	nanoseconds
Ω	ohms
pF	picoFarads
rad	radians
s	seconds
V	volts

1. INTRODUCTION

This final report describes the continued design and hardware implementation of an acousto-optic (AO) multichannel adaptive optical processor (MADOP) for application to the cancellation of multipath jamming interference in advanced surveillance radars. This Expert in Science and Engineering (ESE) effort is a continuation of an ongoing program within the Rome Laboratory Photonics Center (References 1 through 5). Approximately half of the Dynetics effort was performed on-site at Rome Laboratory, Griffiss Air Force Base, NY. This work was accomplished in conjunction with Photonics Center personnel: Capt. M. Ward, Capt. C. Keefer, and 1Lt. H. Andrews under the in-house Project 4600P107. All the work described in this report was performed under ESE Contract F30602-92-C-0026 during the period of 1 February 1992 to 31 October 1992.

The objective of this effort was the continued fabrication and performance characterization of a multichannel adaptive system that can perform cancellation of multiple wideband (10 MHz) interference sources in the presence of multipath. The MADOP system is composed of three primary subsystems:

1. A multichannel AO time-integrating correlator performs a correlation between the residual cancellation error and each of the auxiliary omnidirectional antennas to arrive at updates for each of the adaptive weight functions.

2. A digital interface accepts this update information and generates the appropriate adaptive weight functions for performing auxiliary channel filtering.

3. A multichannel AO tapped delay line (AOTDL) filter system accepts these weight functions through an AO spatial light modulator (AOSLM) and taps the auxiliary channel inputs to form the estimate of the interference signal in the main receiver channel. This interference signal estimate is then subtracted from the main receiver channel at the system intermediate frequency (IF) to form the residual cancellation error for input to the multichannel time-integrating AO correlator, thereby closing the adaptive loop.

The emphasis of this effort was the achievement of open- and closed-loop operation of the MADOP using laboratory-generated test signals. The radio frequency (RF) interfacing of the two AO subsystems was supported by the development (by 1Lt. Andrews) of the software required to estimate tap weight positions and amplitudes from correlator output data and to control a frequency generator via GPIB to provide this tap signal to the AOSLM. Because of the long correlator integration times, resulting in good estimates of the interference environment, single-step cancellation in an open-loop configuration was emphasized.

This technical report is organized as follows. The MADOP algorithm simulation and results are presented in Section 2. The continued design, hardware implementation, and characterization of

the AO subsystems are presented in Section 3. Section 4 provides details on the MADOP open- and closed-loop testing and system performance, together with the design of a post-filtering adaptive electronic cancellation system for improved performance. Conclusions and recommendations are presented in Section 5, followed by appendices containing additional design details, a draft technical paper, and software listings.

2. ALGORITHM SIMULATION AND RESULTS

The simulation of various algorithmic approaches to the MADOP system was continued to assess the benefits of a variety of architectural variants. The software package used for numerical analysis was MATLAB, put out by Math Works, and the simulations developed are documented in Appendix C. Background material on the adaptive radar system's operational configuration is provided in Reference 1.

2.1 BLOCK-LEAST MEAN SQUARE (LMS) SIMULATION

A MATLAB simulation of the Block-LMS algorithm was developed as a modification of a previously developed LMS software routine. A version of this Block-LMS simulation is shown as "lmsRLcorr" in Appendix C. This algorithm is the same as the LMS algorithm except that the weight update calculation is integrated over a block of data before actually implementing a change in the weights. In the software, this is performed in the loop beginning if (n-1)/100 =k, where the block size is 100 and the weight vector is updated only when the iteration number (n-1) is a multiple of 100. For this simulation, a single interference source, x, modeled as white noise (using a random number generator) is passed through two finite impulse response (FIR) filters to simulate multipath. No other signals are present in the simulation. The two FIR filters are defined by delay increments and amplitudes for both the main and auxiliary channels. For example, in the "lmsRLcorr" software in Appendix C, the main channel is created by delaying x by 60 samples and weighting it by 0.631, while the auxiliary channel is composed of three weighted and delayed versions of x. FIR filters are sometimes also referred to as moving average (MA) filters (Reference 6).

Figure 2-1 shows the interference cancellation scenario, where $n_1(t)$ through $n_p(t)$ represent p independent interference sources. The main channel receives the signal, d (t), composed of the target return, s(t), plus each interference source after multipath filtering (modeled by FIR filters $G_{ij}(t)$). The R auxiliary channels receive each interference source after multipath filtering. Due to the omnidirectional beam of the auxiliary antennas and the low signal-to-noise (S/N) ratio in the directional main channel, it is assumed that s(t) is not present in the auxiliary channels. Each auxiliary channel is filtered with the FIR filters represented by the weight functions $w_1(t)$ through $w_R(t)$ to form an estimate, dest(t), of the main channel signal, d(t). The residual error is then used to adaptively update the weight functions to achieve convergence of the system to a minimum mean-square error.

Referring to the cancellation scenario presented in ***Figure 2-1***, notice that multipath can be modeled by the FIR filters $G_{ij}(t)$, which can be thought of as tapped delay line (TDL) filters. For a single channel, the goal of the adaptive filter is to cancel the effects of multipath in the auxiliary channel,

$G_{11}(t)$, and implement the effects of multipath in the main channel, $G_{10}(t)$, thereby accurately estimating the interference in the main channel signal d(t). Thus, the transfer function of the adaptive filter, $W_1(f)$, must be given as:

$$W_1(f) = \frac{G_{10}(f)}{G_{11}(f)}. \tag{2-1}$$

Because the FIR filters by definition have only zeros and no poles, in general $W_1(f)$ will have poles due to $G_{11}(t)$ and zeros due to $G_{10}(t)$. Thus, to exactly estimate the required filter function, an infinite impulse response (IIR) filter must be employed (both poles and zeros). Because a TDL architecture, as employed in the MADOP and other AO adaptive filters, implements only FIR filters, it appears that cancellation cannot be obtained. However, a sufficiently long FIR can be used to approximate an IIR filter response.

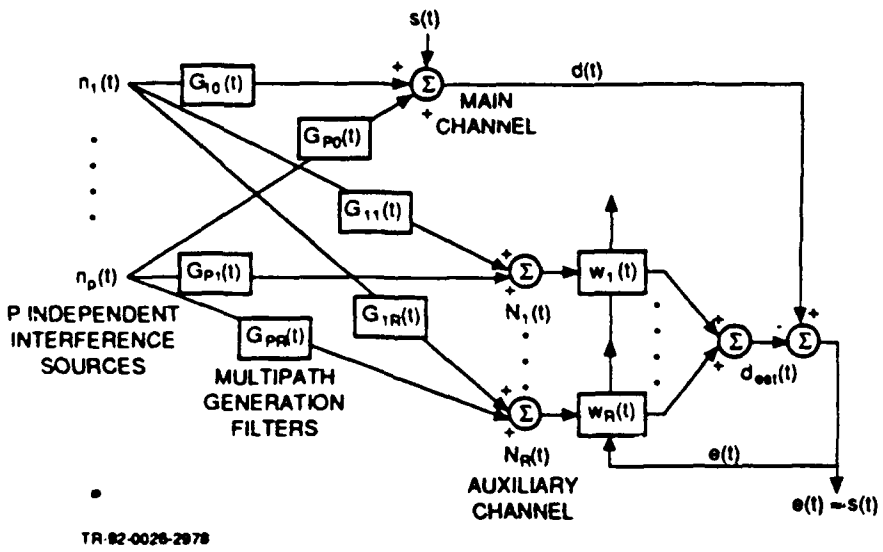

Figure 2-1. Model of the Multipath Scenario

A stable IIR filter will have an impulse response that decays to a very small value after some period of time. The length of the impulse response for a FIR filter is the length of the filter. Therefore, if the FIR filter is made long enough, the IIR filter impulse response can be well approximated. As the FIR filter is shortened, convergence to the ideal solution will always be bounded by the residual error

resulting from the inability to simulate the long-time behavior of the IIR filter impulse response. However, cancellation can still be performed. This is one benefit of implementing a 5-μs delay window in the MADOP even if the multipath delay is much less than 5 μs.

Results of the simulation for several different conditions are described below. ***Figure 2-2*** shows the results for cancellation of severe multipath in the main channel when no multipath is in the auxiliary channel. In this case, the functions defining the delays were given as:

delays = [1, 8, 12, 15, 25, 28, 48],
num(delays) = [0.231, 0.384, 0.58, 0.69, 0.69, 0.504, 0.102],
delays2 = [1], and
num2(delays2) = [0.251],

where the "delay" vectors represent the tap positions and the "num" vectors represent the tap amplitudes. As anticipated, since the ideal filter for this example has only zeros (see Equation 2-1 with $G_{11}(t) = 1$), the adaptation is quite efficient and the resulting weight vector closely matches the tap structure required to implement $G_{10}(t)$. The opposite case, and a more likely scenario when a directional main antenna is employed, is one in which the number of multipath delays in the auxiliary channel is larger than that in the main channel. ***Figure 2-3*** shows results for such a scenario. In this example, the delays were given as:

delays = [20],
num(delays) = [0.23],
delays2 = [1, 5], and
num2(delays2) = [0.251, 0.69].

It can be seen here that cancellation results in this example, but approximately 20 dB less than the simpler case above. The weight vector shown has effectively implemented a FIR filter estimate of Equation 2-1 when $G_{10}(t) = 1$ (an IIR filter). Such an all-pole filter is also known as an autoregressive (AR) model filter (Reference 6). It can be seen that the weight vector is bipolar and does not resemble the multipaths present in the scenario. To implement bipolar weights, complex weights must, in effect, be implemented at the IF of the MADOP processor (i.e., shift the phase of the IF carrier while leaving the envelope relatively unchanged).

Understanding the effects of FIR filter implementation of IIR filter estimates suggests a possible improvement to the AO adaptive filters. Using feedback in an AO system, it may be possible to implement a class of IIR filters, thereby perhaps generating better estimates with finite length filters. One possible architecture for performing IIR filtering is shown schematically in ***Figure 2-4(a)***, and an AO implementation is shown in ***Figure 2-4(b)***. The equation describing this arbitrary IIR filter is:

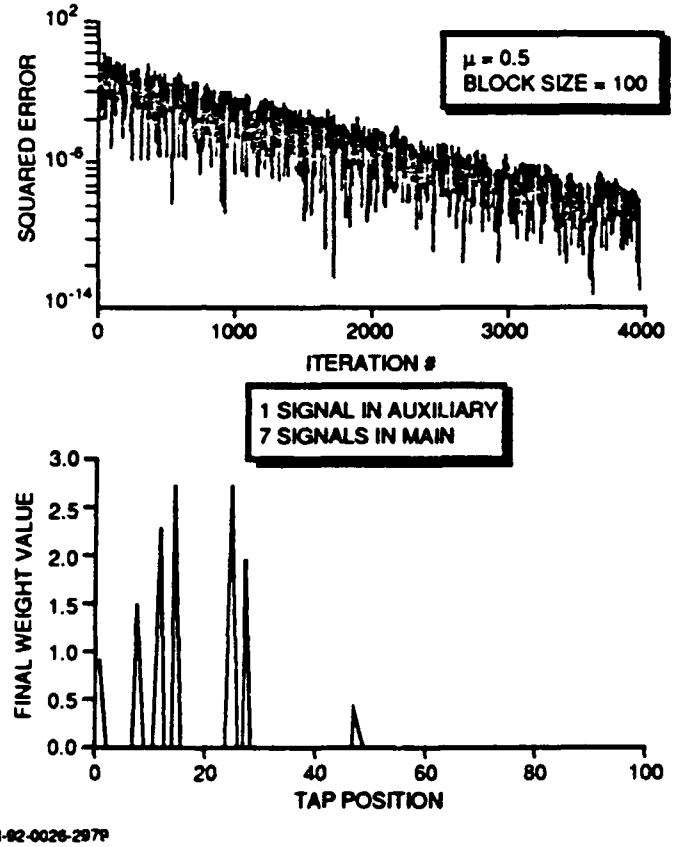

Figure 2-2. Cancellation for Multipath in Main Channel But Not Auxiliary Channel

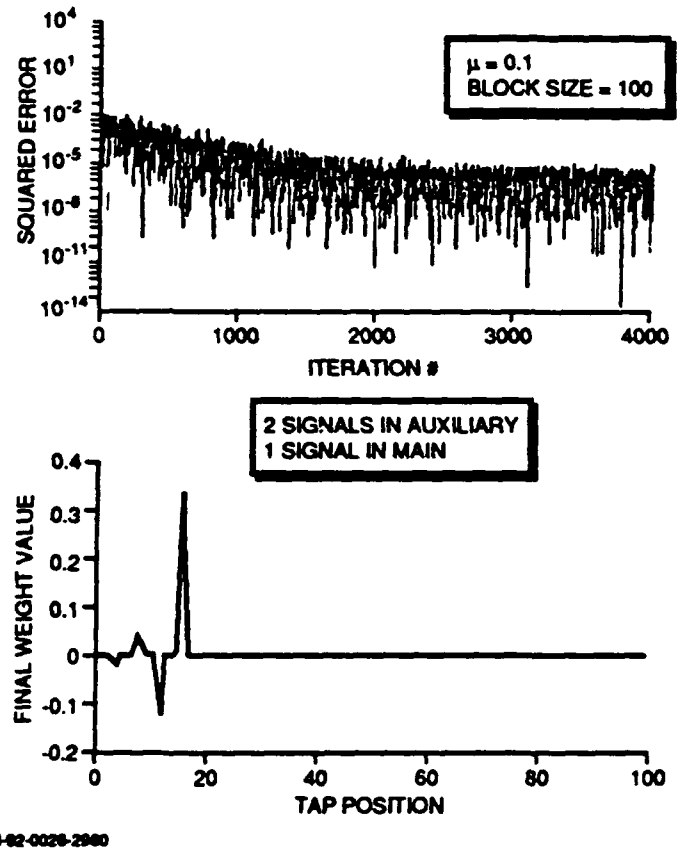

Figure 2-3. Cancellation for Multipath in Auxiliary Channel But Not in Main Channel

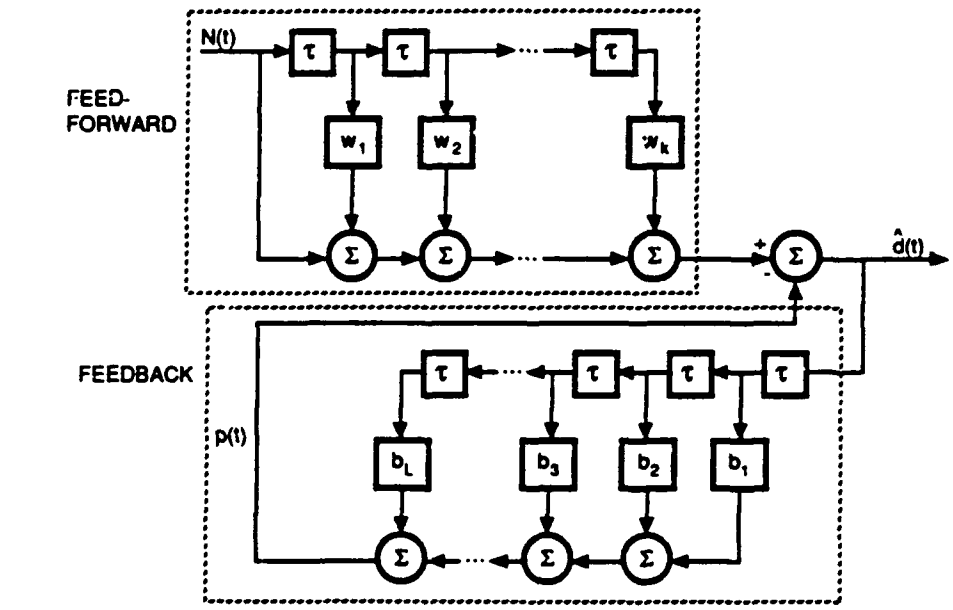

(a) IIR Filter Architecture

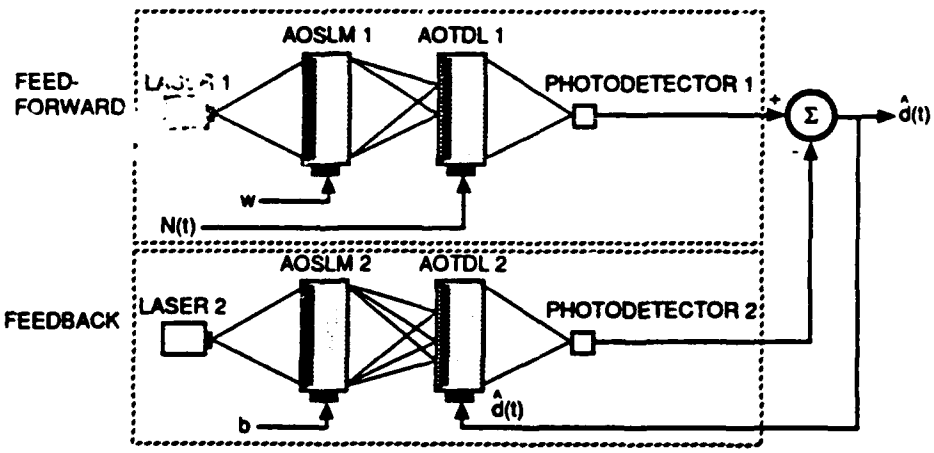

(b) AO IIR Filter Implementation

TR-92-0026-2981

Figure 2-4. IIR Filtering

$$\hat{d}(t) = N(t) + \sum_{i=1}^{K} w_i N(t - i\tau) - p(t) = N(t) + \sum_{i=1}^{K} w_i N(t - i\tau) - \sum_{j=1}^{L} b_j \hat{d}(t - j\tau) \qquad (2\text{-}2)$$

where K and L are the lengths of the feed-forward and feedback filters, τ is an increment of time, N(t) is the filter input, $\hat{d}(t)$ is the filter output, and w_i and b_j are the feed-forward and feedback filter weights, respectively. For this architecture, an optical implementation as shown in ***Figure 2-4 (b)*** requires two separate AOTDL subsystems that can share a common laser but cannot share a common detector. In addition to the added complexity, the gradient algorithm for IIR filters is more complex than for FIR filters and must take into consideration the possibility of unstable filter response. These issues should be further studied before implementation to assess applicability to severe multipath environments and resulting benefits.

2.2 OPTICAL JAMMING CANCELLER (OJC) SIMULATION MODIFICATIONS

The computer model used to study the operation of the MADOP, named the OJC (Reference 1), was modified to more closely resemble the system being constructed in the lab. The modifications involved increasing the integration time of the correlator from 5 to 450 µs. In the hardware the integration is 2 ms, but a 2-ms integration time was not used in the OJC model because of computer time and memory limitations. The second modification was to change the model so the weights computed during the kth computation cycle of the OJC were applied to the signal during the $(k+1)^{th}$ computation cycle. This is the manner in which the hardware will function because of the lags in the computer. Finally, the model now uses new interference signals during every computation cycle, as would occur in the hardware. The old model used the same jamming signal on the various computation cycles to eliminate the effect of new jammer signals on convergence of the algorithm. The modified model was then used to study properties of the MADOP to further the understanding of its operation and to attempt to define how the MADOP should be used in a radar system.

Preliminary results obtained from the OJC model are encouraging. Most notable is the fact that the longer integration time provides better weight computation, thus better jammer cancellation. This was an expected result since the longer integration time provides a better estimate of the interference environment. This, in turn, stems from the fact that the longer integration time means that the time averaged correlation is a closer approximation to the statistical correlation it represents. A negative impact of the longer integration time is that the interference environment must be sufficiently stable during this time and after the weight vector is updated to achieve cancellation.

Several test cases were run using the new OJC model. These led to some valuable observations concerning the performance of the MADOP under different conditions. The observations are discussed below. In all of the model runs it was assumed that there was only one jamming source

and that the MADOP had only one cancellation channel, which is equivalent to having only one auxiliary antenna. However, several of the following observations will hold for the case of n jamming sources and n MADOP cancellation channels.

When there is only a direct path jamming signal in the auxiliary channel, the MADOP is very effective in cancelling both direct and multipath jamming signals in the main channel. Cancellation ratios in excess of 50 dB were often observed in the OJC model. It was also noted that the use of the longer integration times resulted in rapid convergence of the OJC weight computation. In several cases, the weights converged to a value very close to their final value within one computation cycle. It is not clear, however, that the convergence time of the new model is any better than one that used a shorter integration time and shorter computation cycle. This is an area that should be investigated further since it could have an impact on how weight computation is performed by the hardware. It is expected that the tradeoffs will lie in the areas of hardware requirements, convergence time, stability of the weight computation process, and overall performance of the canceller.

Another area that needs to be investigated is whether the convergence parameter, a, should be adaptively computed or fixed. It was found that if the adaptive method was used, the weights often converged very rapidly. This would be very useful in a changing jamming environment. However, a negative aspect of the adaptive method was that it caused the weight computation to diverge in several cases, which is very undesirable in a tactical environment. When a fixed convergence parameter was used, there was no problem with divergence, but the convergence was slower than with an adaptive convergence parameter.

The ability of the MADOP to cancel interference when the signals into the auxiliary and main channels have multipath as well as direct components depends upon the relative magnitudes and delays of the direct and multipath components. This can be explained as follows.

Let $n_m(k)$, $n_a(k)$, and $w(k)$ represent the main channel signal, the auxiliary channel signal, and the weight vector, respectively. Sampled data analysis is used here for ease of explanation. While the actual signals are not true sampled data signals, they are similar, thus the conclusions based on considering sampled data signals will apply to the actual signals. The desired (target) part of the main channel signal will be ignored, without any loss of generality. Let $N_m(z)$, $N_a(z)$, and $W(z)$ represent the Z-transforms of the above. If one casts the interference cancellation as a transfer-type filter problem, the ideal cancellation condition is that:

$$W(z)N_a(z) - N_m(z) = 0 \tag{2-3}$$

must be satisfied. This yields an ideal $W(z)$ as:

$$W(z) = \frac{N_m(z)}{N_a(z)} \tag{2-4}$$

Given that $n_m(k)$ and $n_a(k)$ derive from the same jamming source, n(k) (with Z-transform N(z)), $N_m(z)$ and $N_a(z)$ will be of the form:

$$N_m(z) = \left(\sum_{l=0}^{M} a_l z^{-l}\right) N(z) \tag{2-5}$$

and

$$N_a(z) = \left(\sum_{r=0}^{N} b_l z^{-r}\right) N(z) \tag{2-6}$$

which yields:

$$W(z) = \frac{\sum_{l=0}^{M} a_l z^{-l}}{\sum_{r=0}^{N} b_r z^{-r}} . \tag{2-7}$$

The first thing noted is that the ideal W(z) is in the form of an IIR filter. However, in the actual MADOP, the W(z) is a FIR filter. If the MADOP is to achieve good cancellation, the impulse response of the FIR filter should closely approximate that of the ideal IIR filter. If the impulse response of the IIR filter (ideal W(z)) decays within the duration of the AOTDL (±2.5 μs), then the impulse response of the actual FIR W(z) will provide a good approximation to the impulse response of the ideal IIR W(z) and will provide good cancellation. If the impulse response of the ideal IIR W(z) extends significantly beyond the length of the AOTDL, the actual FIR W(z) probably will not perform well.

The duration of the response of the ideal IIR W(z) is primarily governed by its poles. The response will have a long duration if the poles are close to the unit circle of the Z-plane. If the poles are fairly far removed from the unit circle, the response will decay rapidly. The poles will be located well away from the unit circle if the delays between the direct and multipath returns (in the auxiliary channel) are short and the amplitude of the multipath returns is smaller than the direct return. This assumes the direct return arrives before the multipath return, which will be the case in practice. To be more specific, the requirement is that the amplitude of the multipath return relative to the direct return decrease as the delay between them increases.

Suppose that:

$$n_{a1}(k) = n(k) + 0.9n(k-1) \tag{2-8}$$

and

$$n_{a2}(k) = n(k) + 0.2n(k-1). \tag{2-9}$$

In Equation 2-8, W(z) will have one pole with a magnitude 0.9 and its impulse response will decay in about 45 samples. On the other hand, the W(z) for Equation 2-9 will have a single pole with a magnitude of 0.2 and its impulse response will decay in 4 to 5 samples. If the delay of Equation 2-9 is increased to 16 samples, rather than one, i.e.

$$n_{a3}(k) = n(k) + 0.2n(k-16) \tag{2-10}$$

the associated W(z) will have 16 poles with a magnitude of about 0.9. Thus, its response will decay in about 45 samples, as with the first example.

How well the delay versus magnitude condition can be satisfied will depend on the characteristics of the target geometry and terrain. This should be studied. It is expected that, for air defense scenarios consisting of low-altitude targets in a diffuse multipath environment (grass and trees in dry weather), the above requirements can be satisfied. For targets over water and sand, the requirements may not be satisfied because these represent specular multipath environments.

The main channel direct and multipath signals also play a role in the impulse response of the IIR filter but to a lesser extent than the auxiliary channel multipath. If the delay of the direct and/or multipath main channel signal is significantly different from the delay of the auxiliary channel direct path signal, the impulse response of the ideal W(z) could be delayed such that the transients do not settle within the limits of the AOTDL. Preliminary thoughts on this are that the relative delays will be driven by the location of the auxiliary antennas. If the auxiliary antennas are close to the main antenna, the main channel delays relative to the auxiliary channel should be small.

2.3 IMPLICATIONS TO THE MADOP DESIGN

Some thoughts on implementation of the MADOP in an actual radar follow. For sake of this discussion it is considered that the MADOP will be implemented in a pulsed-Doppler, phased-array, air defense radar. This type of radar normally operates on a dwell basis wherein the antenna beam is directed to a fixed position and a burst of pulses is generated and processed. The dwell time would be from 3 to 10 ms, and typical spacing between pulses would be 10 µs. The pulsewidth would be between 0.5 and 2.0 µs and could have modulation to extend the bandwidth to between 5 and 10 MHz. In this scenario, the objective of the MADOP is to cancel the jamming signal within the first one-fourth to one-

third of the dwell time. The remaining part of the dwell would be needed to perform signal processing to eliminate clutter returns and provide S/N improvement. As an alternative, the dwell could be extended when jamming is present to allow for jammer cancellation. In practice, one could probably expect to have 2 to 3 ms that could be allotted to jammer cancellation.

Since the radar beam is dwelling in a fixed position it is reasonable to expect that, during the time that the MADOP is computing its weights and cancelling the jamming signal, the jamming environment is remaining fairly constant. A standoff jammer moving at 300 m/s will move 1 m in 3.33 ms, which is probably a high velocity for a standoff jammer. It would seem that such a small amount of motion would have very little effect on the direct and multipath environment. If this is true, it would mean that the MADOP would have a very good chance of achieving satisfactory jammer cancellation. If one assumes the integration time of the MADOP is 500 μs and that the weights could be updated every 500 μs, it would be possible to perform four to six iterations during the time allotted to jammer cancellation. Studies using the OJC model indicate that this should be adequate to provide 30 to 50 dB of jammer cancellation in reasonable jamming environments. With an efficient acceleration parameter computation routine it may be possible to obtain even more cancellation.

The sequence of steps in the implementation of the MADOP would be as follows:

1. During the first 2 to 3 ms of the dwell, the OJC would compute the weight. The output of the MADOP would not be used in the radar signal processor during this interval.

2. During the remainder of the dwell, the MADOP would continue to update its weights and perform jammer cancellation. The output of the MADOP would be used in the radar signal processor during this time period.

3. The MADOP would be essentially reset at the start of each dwell. This is necessary since the jamming environment will change dramatically from dwell to dwell. Also, when one thinks of dwell-type, phased-array radars from a signal processing viewpoint, one normally considers each dwell to be a separate event unrelated to other dwells.

The primary advantage of the MADOP is cancellation of multipath delays much greater than the inverse signal bandwidth, which negates the effectiveness of classical sidelobe canceller systems. Because of our studies using the Block-LMS and OJC simulations, we feel that there is significant potential for the MADOP system in realistic scenarios. This is especially true when the environment is predominantly stationary over millisecond timeframes. In these cases, the single-step open-loop approach (residual error is not fed back to the correlator) should offer satisfactory cancellation performance due to the accurate estimates of the multipath delays and resulting tap positions. For severe multipath environments consisting of significantly greater multipath in the auxiliary channels than in the main channel, cancellation will be difficult for any adaptive system.

3. MADOP IMPLEMENTATION PROGRESS

During the performance of this effort, the optical subsystems of the MADOP were tested and enhanced. Previous test results and a detailed theoretical development of the processors are provided in Reference 1. Appendix B also provides a detailed theoretical description of the AOTDL.

3.1 TIME-INTEGRATING CORRELATION FOR WEIGHT FUNCTION CALCULATION

The work performed on the time-integrating correlator concentrated on multichannel operation, system refinement, and enhancing the correlation performance and stability for an optimized MADOP system.

Utilizing a slightly modified hardware implementation of the two-path, time-integrating correlator as described in Reference 1, a multichannel correlator was assembled (by Capt. Ward) to include the insertion of a tilted beam splitter for optical beam replication. ***Figure 3-1*** illustrates the optical layout as modified through the addition of the new beam replication optics. This single-channel AO cell, together with the beam replication optics, was later replaced by a multichannel AO cell that is matched in terms of channel spacing, aperture, material, etc., to the one currently in the auxiliary antenna path of the interferometer. This second multichannel AO cell has been purchased from the same AO vendor (Brimrose) to obtain the best match between the two paths. The addition of the second multichannel AO cell is described later in this subsection.

Bulk acoustic wave (BAW) delay lines were used during correlator testing to provide differential delay between the error channel and the inputs to the multichannel AO cell. Each of the BAW devices provides a fixed delay whose value depends on the acoustic material used and the length of the AO crystal. The procured BAW delay lines provide delays between 5.0 and 10.1 μs. Thus, to realize a delay of less than 5.0 μs, two devices would be required that provide a differential delay equal to the desired value. For example, if a 1.1-μs delay is needed between two RF inputs, a 5.0-μs BAW device can be used to delay one input and a 6.1-μs BAW delay line to delay the other. In this fashion, differential delays on the order of the incremental BAW delays purchased can be realized. ***Table 3-1*** lists the differential delays obtainable with the current BAW devices. However, since insertion losses are typically high for BAW devices, additional amplification is required for each BAW device used. A continually variable delay line that would provide delays from 0.1 to 5.0 μs would be very useful for this purpose; only one device would be required to provide continuous range of delays (over the device delay window) and small delays could be accomplished, therefore eliminating the requirement of using multiple BAW devices for differential delay realization. The continuously variable delay line (CVDL) is such a device. The CVDL is made by Dynetics and provides user-selectable delays over a continuous

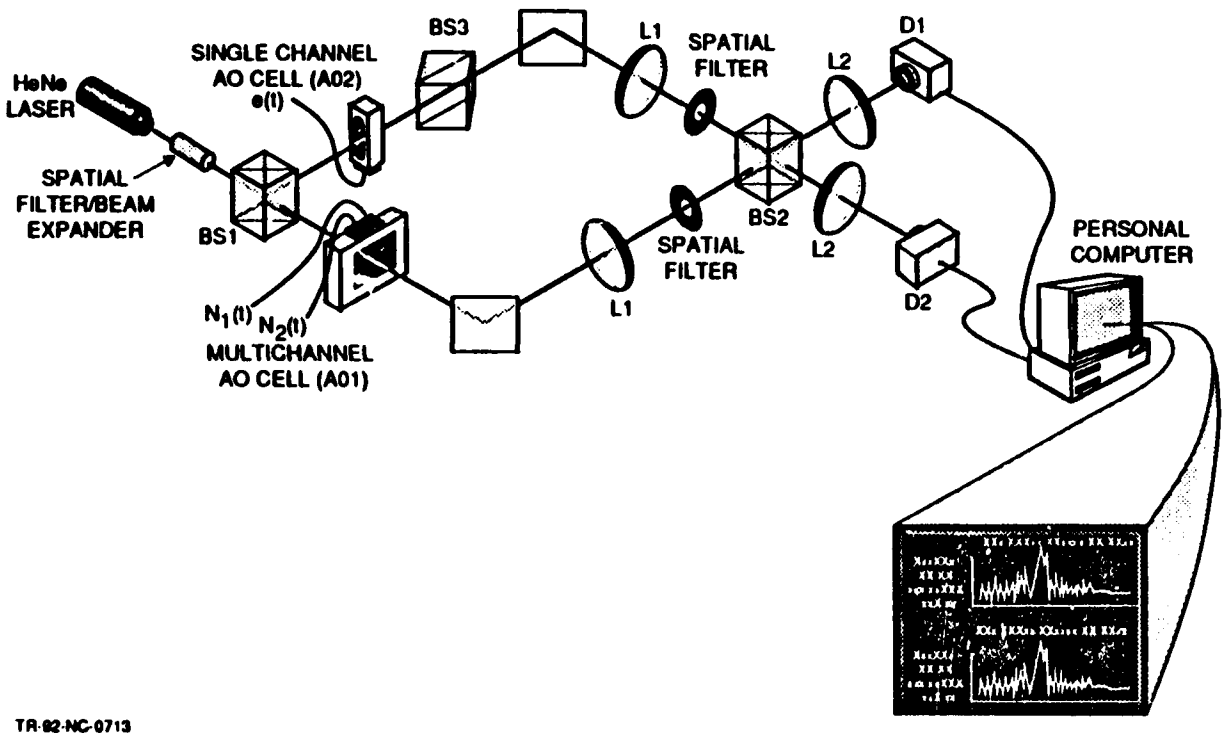

Figure 3-1. Preliminary Multichannel Time-Integrating Correlator Layout

range of delay. For example, model CVDL-80-10-5 provides user-selectable delays from 150 ns to 5 μs at 80 MHz with a 10-MHz bandwidth.

Table 3-1. Differential Delays (BAW Devices)

Delay 2 (μs) \ Delay 1 (μs)	5.00	5.10	5.25	5.35	5.50	5.60	6.00	6.10	7.50	7.60	10.00	10.10
5.00	0.00	0.10	0.25	0.35	0.50	0.60	1.00	1.10	2.50	2.60	5.00	5.10
5.10	-0.10	0.00	0.15	0.25	0.40	0.50	0.90	1.00	2.40	2.50	4.90	5.00
5.25	-0.25	-0.15	0.00	0.10	0.25	0.35	0.75	0.85	2.25	2.35	4.75	4.85
5.35	-0.35	-0.25	-0.10	0.00	0.15	0.25	0.65	0.75	2.15	2.25	4.65	4.75
5.50	-0.50	-0.40	-0.25	-0.15	0.00	0.10	0.50	0.60	2.00	2.10	4.50	4.60
5.60	-0.60	-0.50	-0.35	-0.25	-0.10	0.00	0.40	0.50	1.90	2.00	4.40	4.50
6.00	-1.00	-0.90	-0.75	-0.65	-0.50	-0.40	0.00	0.10	1.50	1.60	4.00	4.10
6.10	-1.10	-1.00	-0.85	-0.75	-0.60	-0.50	-0.10	0.00	1.40	1.50	3.90	4.00
7.50	-2.50	-2.40	-2.25	-2.15	-2.00	-1.90	-1.50	-1.40	0.00	0.10	2.50	2.60
7.60	-2.60	-2.50	-2.35	-2.25	-2.10	-2.00	-1.60	-1.50	-0.10	0.00	2.40	2.50
10.00	-5.00	-4.90	-4.75	-4.65	-4.50	-4.40	-4.00	-3.90	-2.50	-2.40	0.00	0.10
10.10	-5.10	-5.00	-4.85	-4.75	-4.60	-4.50	-4.10	-4.00	-2.60	-2.50	-0.10	0.00

For calibration of the correlation window, a 500-kHz sinusoid was double sideband/suppressed carrier (DSB/SC) modulated at 80 MHz and input into both AO cells. The expected autocorrelation is a sinusoid of the same frequency that is modulated by an optical spatial carrier. This frequency was chosen such that there would be 2.5 periods of the spatial carrier in the 5.0-μs correlation window. The correlation results showed that the 5.0-μs correlation window under-filled the charge- coupled device (CCD) array window. This was expected due to the magnification realized with the lens arrangement provided by the available lenses. As a result, the imaged correlation window appeared to be on the order of 5.25 μs.

To perform the multichannel autocorrelation of a wideband signal, the signal is power-split, delayed, and distributed to the appropriate AO cell channel. ***Figure 3-2*** illustrates the signal distribution layout for multichannel autocorrelation (with relative delays) with respect to the zero delay point in the correlation window. Given time delays of τ_0, τ_1, and τ_2, which are introduced by the insertion of the BAW delay lines, the differential delays for the two channels are given by:

$$\Delta\tau_1 = \tau_1 - \tau_0 \tag{3-1}$$

and

$$\Delta\tau_2 = \tau_2 - \tau_0. \tag{3-2}$$

In the above equations, τ_0 is the BAW delay for the error channel, and τ_1 and τ_2 are the BAW delays for the auxiliary antenna AO cell channels. Thus, $\Delta\tau_1$ and $\Delta\tau_2$ are delays relative to the error channel. Also noted in ***Figure 3-2*** are the additional amplifiers and attenuators required to compensate for BAW delay line insertion losses.

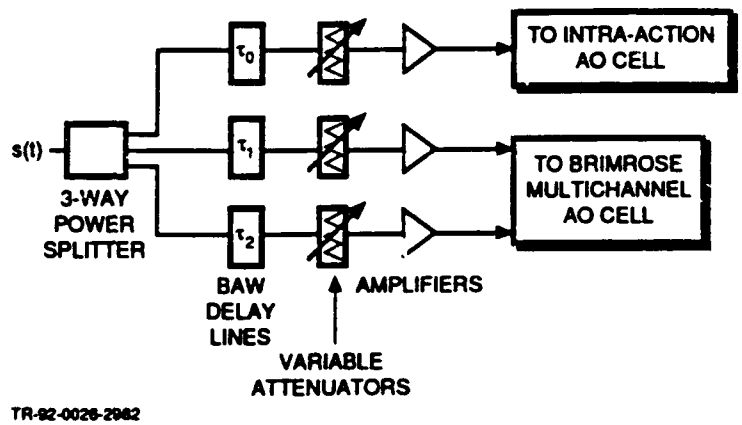

Figure 3-2. Signal Distribution Network

Experiments were performed using a 10-MHz noise source as the input to the correlator. By inserting different BAW delays into the signal distribution network, different differential delays can be realized. With reference to the following figures, a positive differential delay will cause the correlation to shift to the right of the zero delay point while a negative differential delay results in the correlation shifting to the left. ***Figure 3-3*** shows the autocorrelation of s(t) for $\Delta\tau_1$ = + 2.5 µs and $\Delta\tau_2$ = - 2.5 µs. This figure also supports the fact that greater than 5.0 µs of correlation window is being imaged onto the CCD arrays.

Multipath simulation was accomplished through the addition of another RF delay path to one of the auxiliary channels. ***Figure 3-4*** shows the signal generation and distribution network for the multipath simulation. Note that the power levels indicated in the figure are typical power level

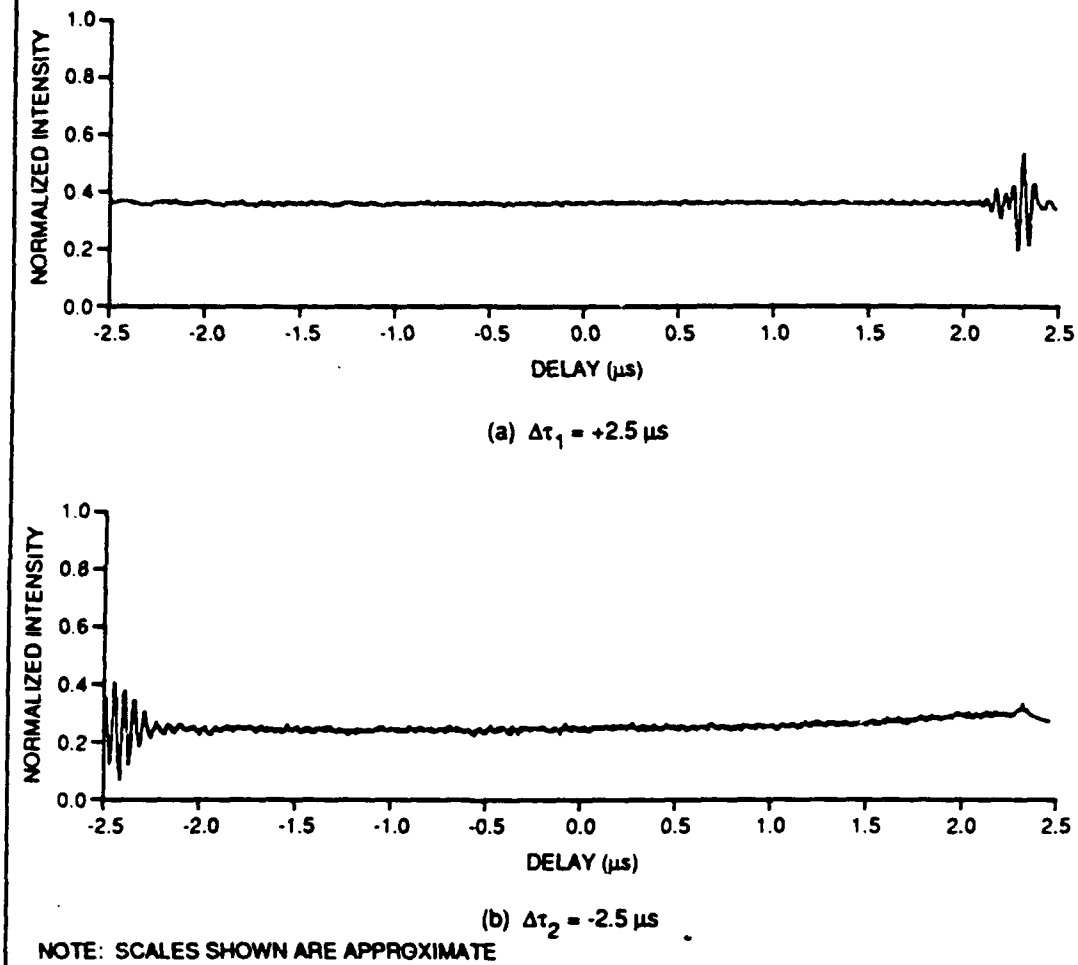

NOTE: SCALES SHOWN ARE APPROXIMATE

TR-92-0026-2983

Figure 3-3. Noise Autocorrelation

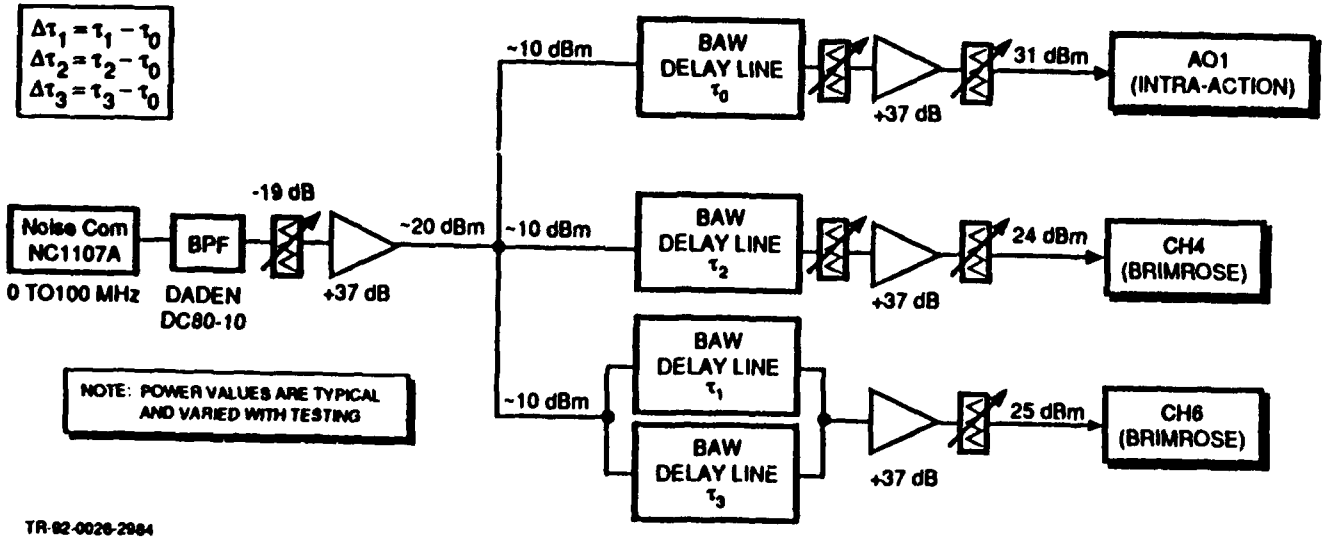

Figure 3-4. Signal Generation/Distribution Network for Multipath Simulation, $\Delta\tau_1$ = -0.1 μs, $\Delta\tau_2$ = +0.4 μs, $\Delta\tau_3$ = +1.0 μs

settings used for initial setup and are limited by individual device maximum allowable input power levels. As indicated in the setup, $\Delta\tau_3$ is the additional differential delay term that was added to the auxiliary channel with the $\Delta\tau_1$ differential delay. Differential delays of $\Delta\tau_1 = -0.1\ \mu s$, $\Delta\tau_2 = +0.4\ \mu s$, and $\Delta\tau_3 = +1.0\ \mu s$ were obtained with the available BAW delay lines. The resulting correlation peaks are shown in ***Figure 3-5***.

The multichannel time-integrating correlator for the weight function calculation was further developed through the transfer of the correlator to a 2-ft by 3-ft optical breadboard table. Other advancements in the architecture setup included the replacement of the two-lens imaging system by a one-lens imaging system, the placement of the imaging lens after the second beam splitter, and the reduction in optical axis height and interferometer path length through the selective use of available mounts. Also, the replacement of the single-channel AO cell with another multichannel AO cell (Brimrose) took place at this time. This addition alleviated the necessity of beam replication optics previously described. ***Figure 3-6*** shows the current optical setup. Motivation for these changes included increased stability of the interferometer architecture through minimizing path length and optical axis height and elimination of lenses prior to BS2.

Distortion of the correlation spatial fringes was observed and can be noted in ***Figure 3-7***. An 80-MHz tone was input into both AO cells and the resultant correlation was displayed on the computer monitor. As can be seen in the figure, the fringes appear to be S-shaped rather than the desired and expected straight fringe pattern. Adjustments were made to the final beam splitter, the imaging lens, and the AO cell height and distance from the imaging lens in an attempt to find the cause for this distortion and to correct it. These distortions would prevent the use of a cylindrical lens to collapse the correlation result onto the CCD array.

The source of the fringe distortions was determined to be the error channel AO cell, wherein the acoustic information traveling wave is not parallel to the bottom face of the AO cell housing. Since the housing is used as reference for the component mounting, the mounted AO cell in the correlator was counter-propagating at an offset angle with respect to the other AO cell. ***Figure 3-8*** illustrates this phenomenon. ***Figure 3-8(a)*** shows the preferred acoustic aperture arrangements for the two-path Mach-Zehnder correlator. ***Figure 3-8 (b)*** shows the acoustic aperture arrangement that contributed to the distorted fringes. To correct for the situation, the error channel AO cell was tilted such that its acoustic aperture would be counter-propagating and parallel to the auxiliary channel AO cell. This was accomplished through the utilization of a Klinger lab jack and the current mounting configuration. The lab jack was placed under one end of the AO cell. The raising of the lab jack caused the AO cell to be lifted on one end, causing the acoustic aperture to rotate through the desired angle.

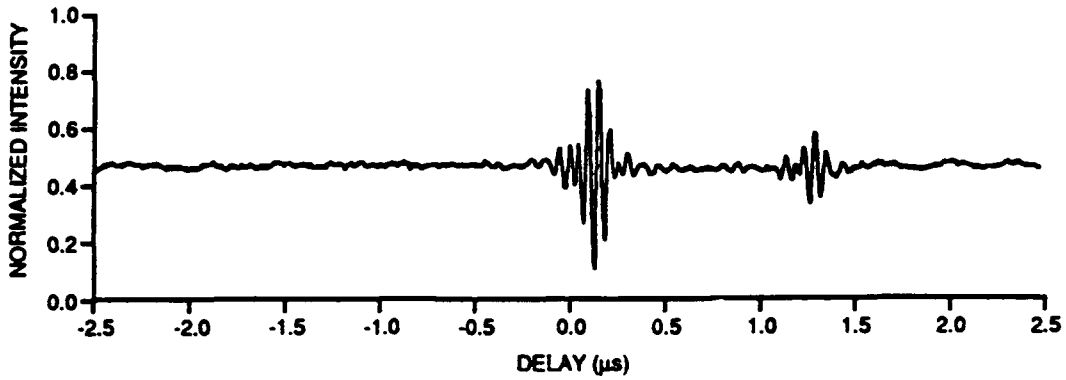

(a) $\Delta\tau_1 = -0.1\ \mu s$, $\Delta\tau_2 = +0.4\ \mu s$

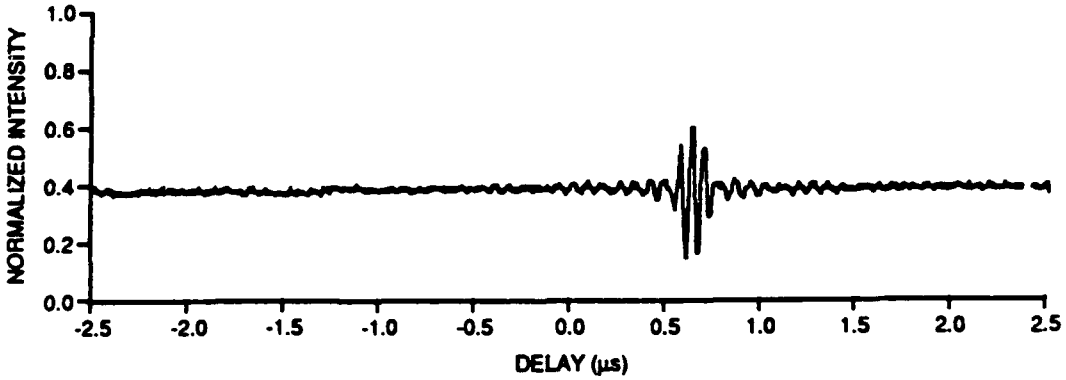

(b) $\Delta\tau_3 = +1.0\ \mu s$

NOTE: SCALES SHOWN ARE APPROXIMATE

TR-92-0026-2905

Figure 3-5. Multichannel Correlation with Multipath

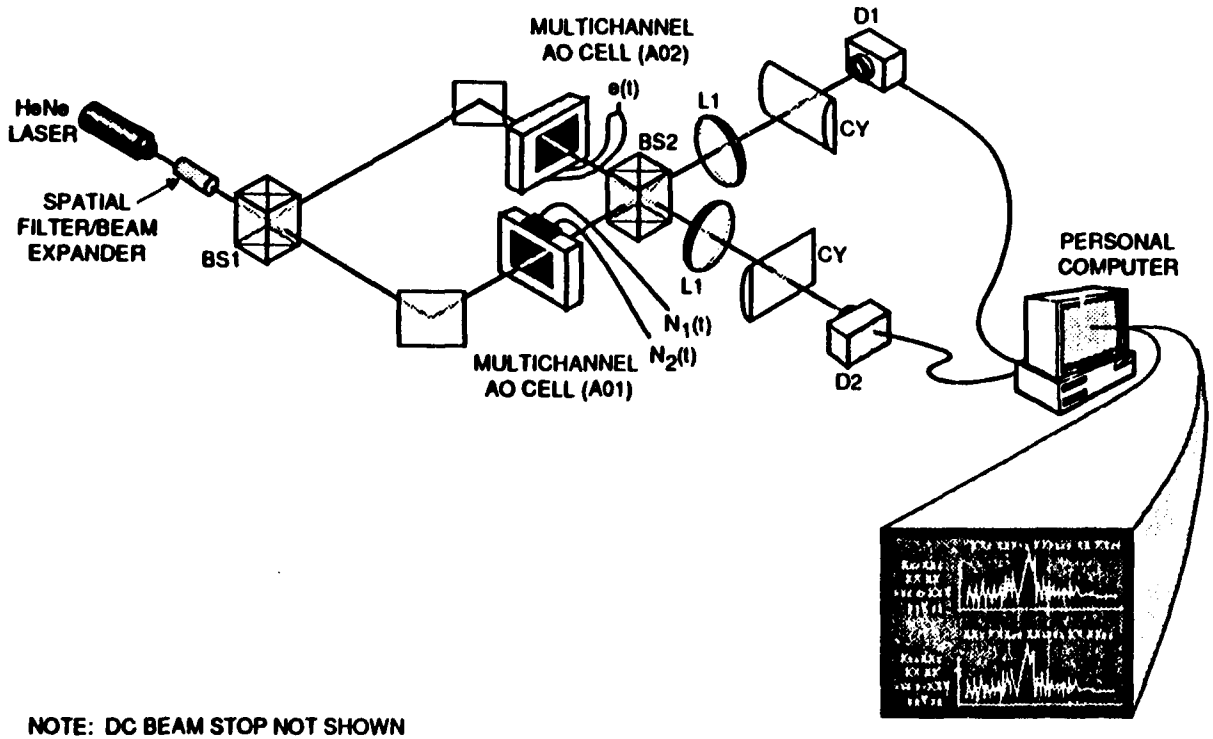

NOTE: DC BEAM STOP NOT SHOWN

TR-92-NC-0713A

Figure 3-6. Multichannel Time-Integrating Correlator Layout

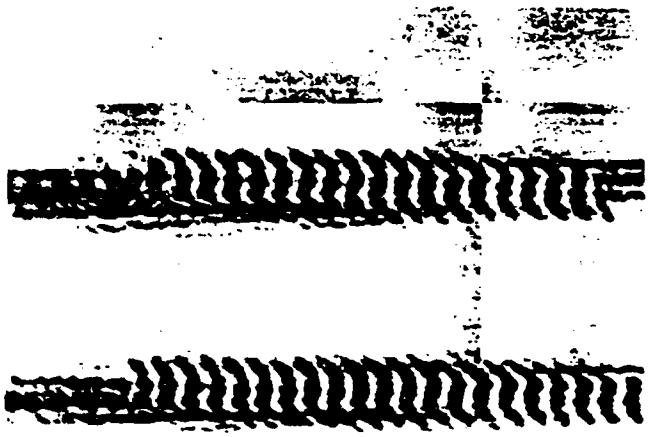

TR-92-0026-2986

Figure 3-7. Distorted Correlation Pattern for 80-MHz Tone

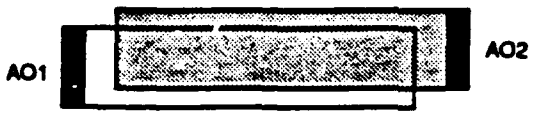

(a) Desired Aperture Arrangements

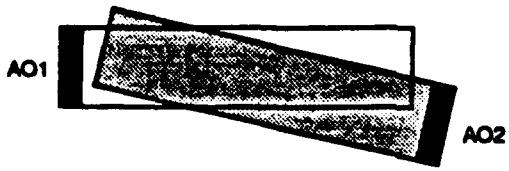

(b) Observed Aperture Arrangements

TR-92-0026-2987

Figure 3-8. Acoustic Aperture Arrangements Resulting in Distorted Correlation Fringes

After the desired angular rotation was achieved, as indicated by correlation fringe orientation, the AO cell was locked down through the existing clamps and AO cell mount.

Figure 3-9 shows the correlation fringes after compensation for the acoustic propagation orientation described above. Note that the remaining deviations seen in the fringe pattern are inherent in the acoustic diffraction pattern and the effects of this can be minimized with the use of a cylindrical lens to collapse the information orthogonal to the range window direction.

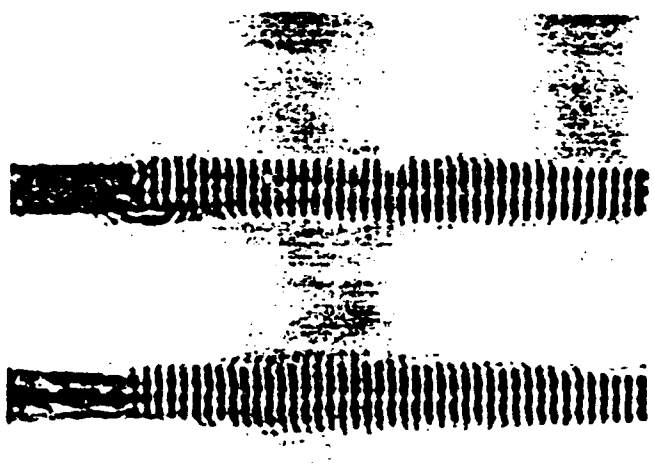

TR-92-0026-2968

Figure 3-9. Correlation Fringes After AO Cell Angular Adjustments

It was observed that the illumination geometry was not optimized for multichannel correlator operation with channels N and N+2. Essentially, the central uniform portion of the illumination beam was overlapping with channel N, and the aperture of channel N + 2 was off to one edge of the illumination beam. This caused some nonuniformities between the response of the two channels in terms of correlator outputs; for the same RF powers into the AO cell, different optical powers and power distributions were observed at the correlation plane. A simple solution was implemented without disturbing the correlator alignment. This included having a separate collimation/beam expansion optics section whose output would be a larger collimated beam. The collimated beam would be input to the Mach-Zehnder interferometer through the use of a beam-steering mirror. This mirror was used to get the desired illumination geometry for correlation without

having to realign the AO cells, the first beam splitter (BS1), or the mirrors in the interferometer. These changes were implemented with a 40X microscope objective and a 200-mm focal length achromat (D = 50 mm).

An important parameter of the correlator system is the range window uniformity, expressed by the correlation amplitude as a function of delay in the range window. One method to test the range window uniformity involves inputting a wideband signal into the AO cells, adding a relative delay between the two signals, and scanning the delay such that the correlation peak translates across the desired range window (5.0 μs). Ideally, the correlation amplitude would remain the same for all delays within the range window. Since a continuously variable delay line was not available, the BAW delay lines were used to implement discrete delays for the testing of the range window uniformity. ***Table 3-1*** lists the available BAW delays and the obtainable differential delays.

During the testing, the RF power into each of the AO cell channels was kept relatively constant at 250 mW. Amplifiers and attenuators were used to keep the power as close to 250 mW as allowed by the attenuation adjustments (0.5 dB). The test data were saved on the computer for analysis at a later time. The data files were saved on the computer hard drive under CHXYZ_ZZ, where X = channel number, 4 or 6, Y = positive or negative delay relative to zero delay, p or m, and Z_ZZ = the relative delay in microseconds. For example, the data file entitled CH4p2_50 is the data for channel four, given a relative delay of +2.5 μs. 1Lt. Andrews has written software that yields a flat spatial response from the output of the cameras for a given center frequency. However, tones and/or signals that are input to the correlator at a frequency other than at the optimized center frequency may not have a flat response across the range window. This may impact the performance of the MADOP in system operation.

Dynamic range testing has previously concentrated on lowering an input signal to one AO cell relative to the other AO cell and noting the decrease of the correlation output. For implementation of automatic gain control (AGC) in a system application, the input power to an AO cell would be maintained at a relatively constant value. A more systems-orientated dynamic range test was devised in which two wideband signals (separated in time) are input to one AO cell while only one wideband signal is input to the other AO cell. The output of the correlator is two correlations that are separated by the relative delay between the two signals input to the first AO cell. ***Figure 3-10*** illustrates the signal generation layout for the dynamic range testing. During the testing, the total power into both AO cells was held relatively constant at 220 mW. The signal generation setup allowed for the attenuation of one of the wideband signals into AO1 while maintaining a constant input power. ***Figure 3-11*** shows the dynamic range test results. As noted in the figure, the signal s(t + 0.5 μs) was

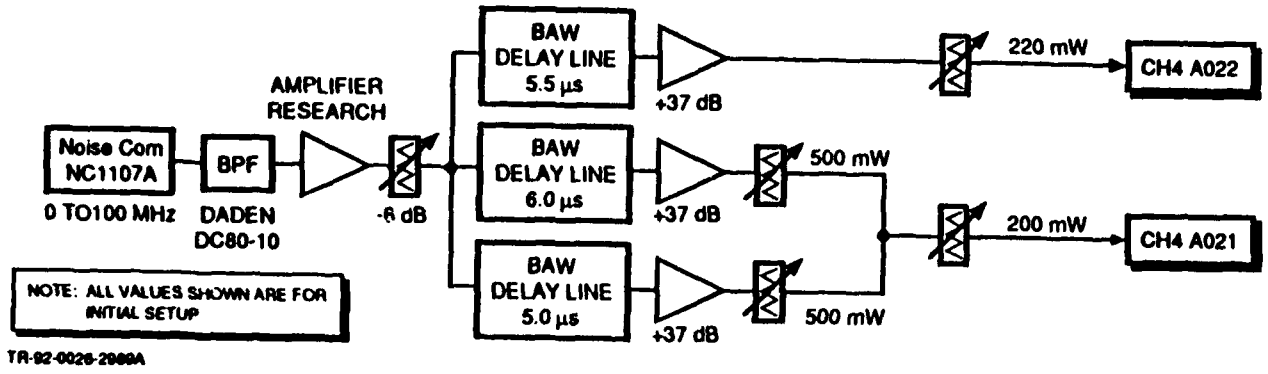

Figure 3-10. Dynamic Range Test Signal Generation Layout

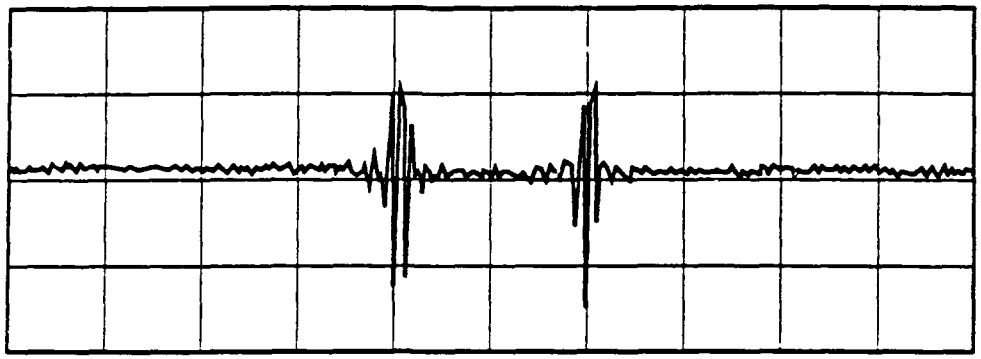

τ = -2.5 μs (a) s(τ + 0.5 μs) Attenuated by 0 dB τ = 2.5 μs

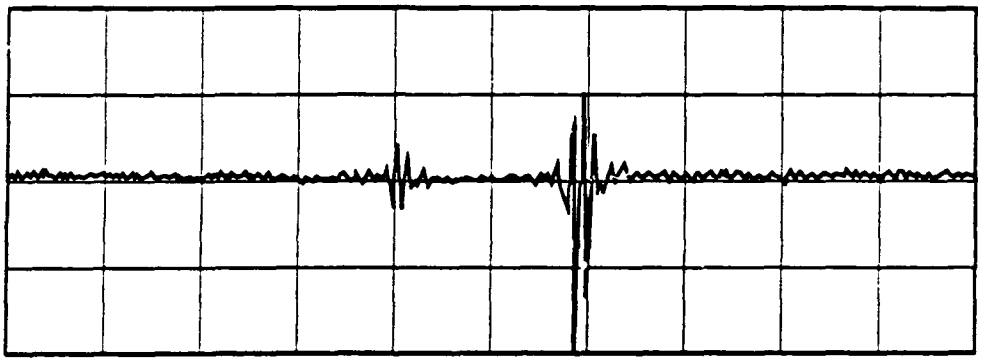

τ = -2.5 μs (b) s(τ + 0.5 μs) Attenuated by 20 dB τ = 2.5 μs

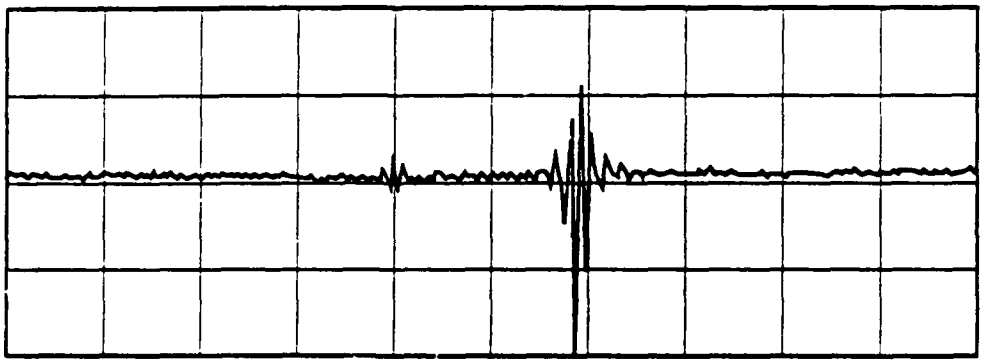

τ = -2.5 μs (c) s(τ + 0.5 μs) Attenuated by 26 dB τ = 2.5 μs

TR-92-0026-2990

Figure 3-11. Dynamic Range Testing

attenuated relative to the signal s(t - 0.5 μs). This testing resulted in an estimate of the dynamic range of >26 dB.

The optical time-integrating correlator subsystem was tra ·'erred to a 2-ft by 3-ft optical breadboard table. The optical components were restructured to redu.:e the optical footprint. Other advancements made in the architecture setup include the replacement of the two-lens imaging system by a one-lens imaging system, the placement of the imaging lens after the second beam splitter (BS2), and the reduction in optical axis height and interferometer path length through the selective use of available mounts. A new mounting technique for improved vibrational stability of BS2 was developed and implemented in the interferometer. It consisted of a flat plate on which the beam splitter was placed. Another flat plate was placed on top of the beam splitter. Long (~ 1.25 in.) 1/4-20 screws were used to clamp the top plate to the bottom plate, thus securing the beam splitter within the housing. This structure was fixed on top of a magnetic base for securing the orientation of the beam splitter after the spatial carrier had been properly set. Additional modifications made to component mounting included the insertion of the mini-jack and fork positioning mounts from New Focus. These components were used in place of the Klinger lab jack used to position the CCD camera. After all of these modifications were performed, it was observed that the correlation peak was more vibrationally stable. This will greatly aid the peak-picking algorithm for AOSLM frequency selection.

In addition to the enhancements made directly to the components on the breadboard table, the correlator optical system breadboard was moved onto the same optical bench as the AOTDL system. This allowed for the two optical subsystems to be enclosed on the optical bench through the installation of plexiglass windows. This enclosure helped reduce the sensitivity of the interferometric optical architecture to changes in optical path lengths due to air currents and other sources. In addition to the installation of the enclosure, vibration isolation was enhanced through the utilization of the floating table supports.

The 5-μs correlation window of the correlator was reduced to better match the 1-μs window of the AOTDL system. It was decided to reduce the aperture to approximately 3 μs, corresponding to imaging 1.5 μs (6.3 mm) of acoustic aperture. A magnification of 1.056 was required, and a 125-mm focal length biconvex lens was used for the imaging. In addition to the new imaging lens, a cylindrical (CY) lens (f = 62.5 mm) was used to collapse the correlation onto the CCD array. This resulted in a more uniform distribution across the array, lower AO cell RF drive powers needed for a given integration time, and helped compensate for the acoustic pattern overlap and spatial differences of the acoustic beam, which is a function of frequency. For example, a two-tone modulation was autocorrelated and the result was displayed on the monitor. With the integration time held constant, the amplitude of the correlation was observed for an input signal power of 250 mW both with and

without the cylindrical lens. After insertion of the cylindrical lens, the same correlation amplitude was accomplished with only 100 mW of RF power into the AO cells. ***Figure 3-6*** shows the current modifications made to the optical architecture.

Calibration of the correlation window was accomplished through the autocorrelation of two-tone DSB/SC modulation at an 80-MHz IF. The modulation frequency was changed until an integral number of half-cycles (correlation peaks) were observed across the array. The correlation window size, t, was determined using:

$$t = \frac{N}{2f} \quad [\mu s] \tag{3-3}$$

where N is the number of half-cycles (correlation peaks) and f is the modulation frequency into the correlator expressed in megahertz. A two-tone frequency of 2.15 MHz resulted in 13 correlation peaks, as noted in ***Figure 3-12***. Using the above formula, a correlation window of 3.0 μs was calculated. A two-tone frequency of 1.17 MHz resulted in a little more than seven correlation peaks, corresponding again to a 3.0-μs correlation window.

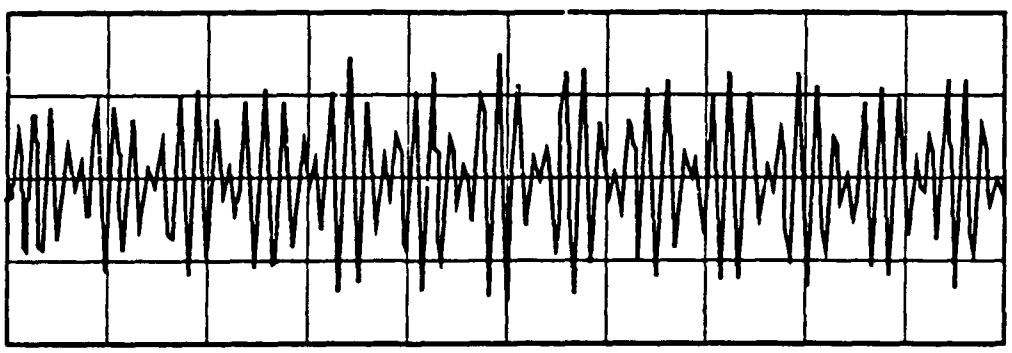

TR-92-0026-2001

Figure 3-12. Range Window Calibration with Two-Tone DSB-SC Correlation (f = 2.15 MHz)

3.2 AOTDL FILTER

The AOTDL architecture was further advanced and tested during this effort. Two new Brimrose AO cells were inserted, and a rotation stage was added to the AOTDL cell to better match the illumination cone of angles to the acoustic column to achieve better overlap of diffracted and undiffracted beams at the photodetector. Also, a translation stage was placed on the spherical Fourier transform lens between the two AO cells to better control the focus of the tap beam at the AOTDL, although this translation stage was found to be of little use in its current configuration because of the need to subsequently realign the photodetector.

Further frequency response measurements were taken on the system, as shown in ***Figure 3-13***. The response over the 10-MHz AOTDL bandwidth was flat to within 3 dB for tap frequencies from 60 to 100 MHz, although the insertion loss of the system varied by about 10 dB. It is possible to compensate for this insertion loss variation by weighting the frequency inputs to the AOSLM, but this will likely cause a reduction in the tap dynamic range. It is important to achieve good alignment of the photodetector both vertically and horizontally in order to get a flat frequency response and minimize insertion loss. Then translation of the photodetector in the focus direction is used to get the frequency response approximately uniform for all tap positions.

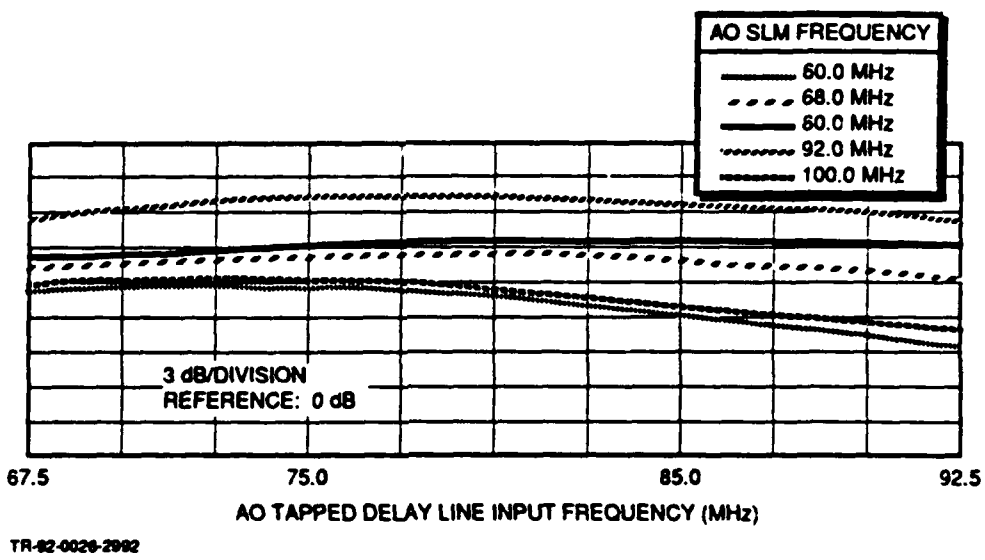

Figure 3-13. System Frequency Response for Various AOSLM Input Frequencies

As an additional test of the AOTDL performance, a two-tone input was provided to the AOSLM to provide a two-tap response. The theoretical effect of this is to weight the input signal with a sinusoidal frequency response (the Fourier transform of the sum of two delta functions representing the two delays). The larger the delay between the two signals, the higher will be the frequency of the sinusoidal frequency-domain weighting. This response was simulated in MATLAB with the program entitled "% AOTDL" (see Appendix C). The resultant frequency responses are shown in ***Figure 3-14*** for closely and widely spaced taps. The two-tap frequency response of the AOTDL was then measured using the network analyzer, and the results were in excellent agreement with the theory, as shown in ***Figure 3-15***.

Using the delay function of the network analyzer to compensate for the linear phase tilt and obtain a flat phase across the passband of the system, it was possible to measure the delay as a function of tap position. The measured values were used to generate the plot shown in ***Figure 3-16***. This information is useful in deriving the conversion factor from the detector position in the AO correlator to the input frequency in the AOTDL. It also shows that at 80 MHz, there are approximately 2.6 μs of delay, which is compensated for in closed-loop operation by using BAW delay lines.

Crosstalk for closely spaced taps was also investigated and found to be worse than the theory showed and worse than on previous contract visits (Reference 1). When tap separations were on the order of 1 to 2 MHz, the crosstalk terms at the IF ± (frequency difference) were within approximately 10 to 15 dB down from the peak at the IF. The reasons for this were not determined.

Measurements of the S/N ratio and insertion loss for the AOTDL system were also made. During the experiments, the noise floor was consistently at -105.7 dBm/Hz (equivalently -35.7 dBm in a 10-MHz bandwidth). Using the spectrum analyzer, the best achieved output signal level was measured to be +5 dBm, resulting in an output S/N ratio of 40.7 dB. This S/N ratio was for a tap frequency of 80 MHz and approximately 400 mW driving both the AOSLM and AOTDL. The insertion loss of the system can be calculated using the network analyzer by adding the displayed insertion loss to any gain provided in the system. Typical best-displayed insertion losses were on the order of 8 dB, and the system employed a 55-dB amplifier after detection, resulting in a 63-dB insertion loss.

A limit on the achievable insertion loss can be estimated by considering the optical tap power, heterodyne efficiency, and detector responsivity. For an AOTDL input power of +23 dBm, the following calculations were made. The tap power for a single tap was measured to be 7.9 mW using an optical power meter, and assuming that 10% of this power results in a heterodyne signal output, a heterodyne output power of $(7.9 \times 7.9 \times 0.1)^{1/2} = 2.5$ mW was obtained. For a 0.25-A/W detector responsivity, 0.62 mA of current is generated, which yields $10 \log [(0.00062)^2 \times 50\Omega \times 1000 \text{ mW/W}] = -17$ dBm. For

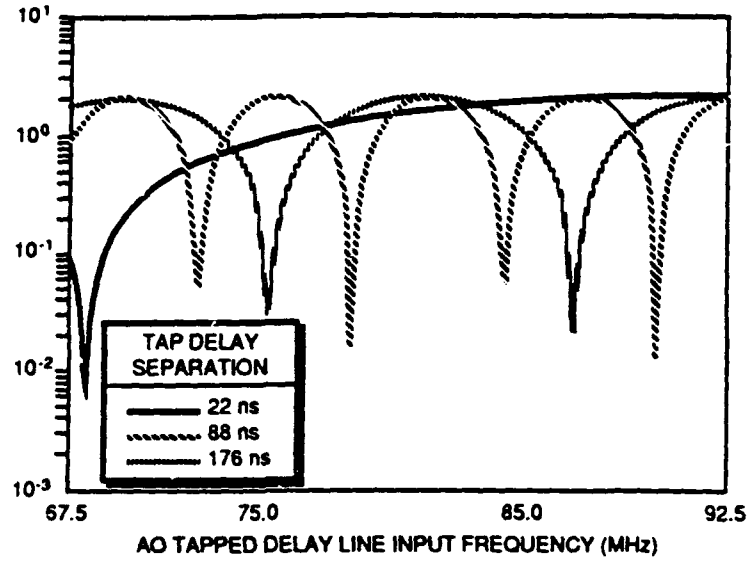

(a) Narrow Tap Separation

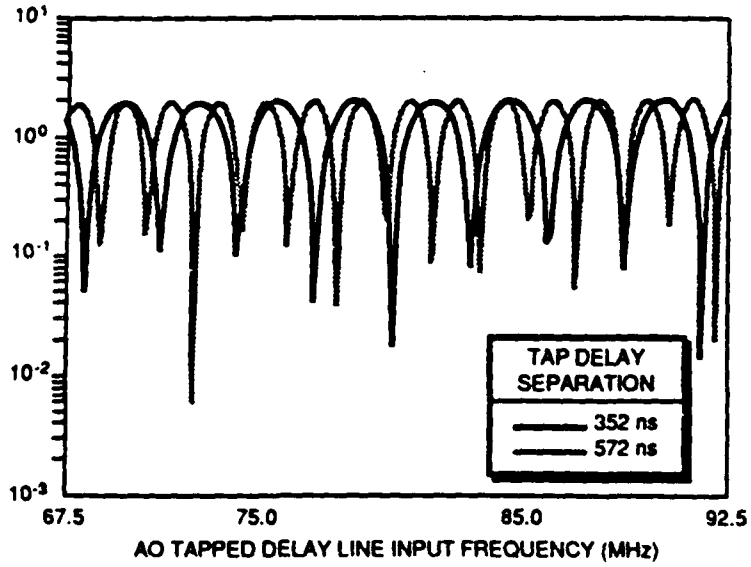

(b) Wide Tap Separation

TR-92-0026-2993

Figure 3-14. Simulated Two-Tap System Frequency Response

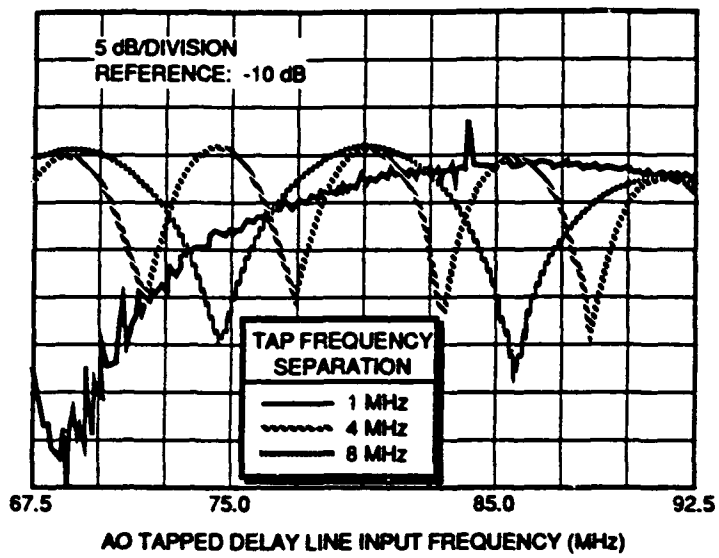

(a) Narrow Tap Separation

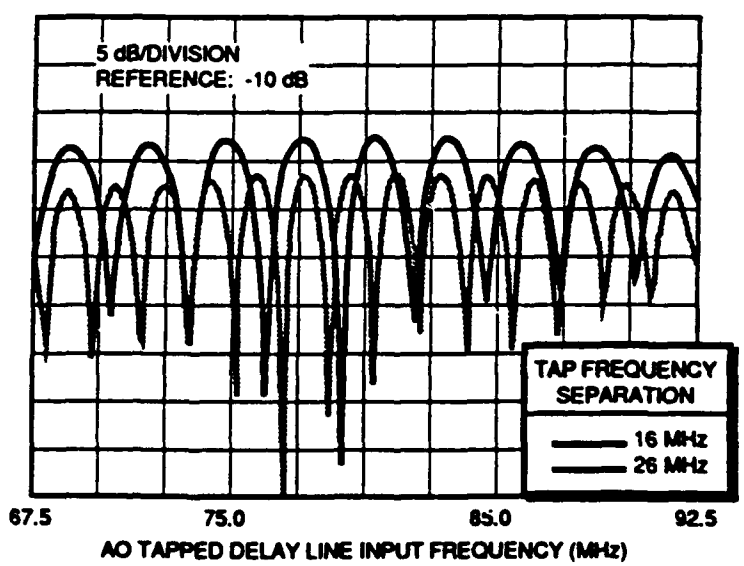

(b) Wide Tap Separation

TR-92-0026-2994

Figure 3-15. Measured Two-Tap System Frequency Response

the +23-dBm input, there is an optimistic theoretical best-insertion loss of 40 dB. Therefore, the system insertion loss may be improved by approximately 23 dB.

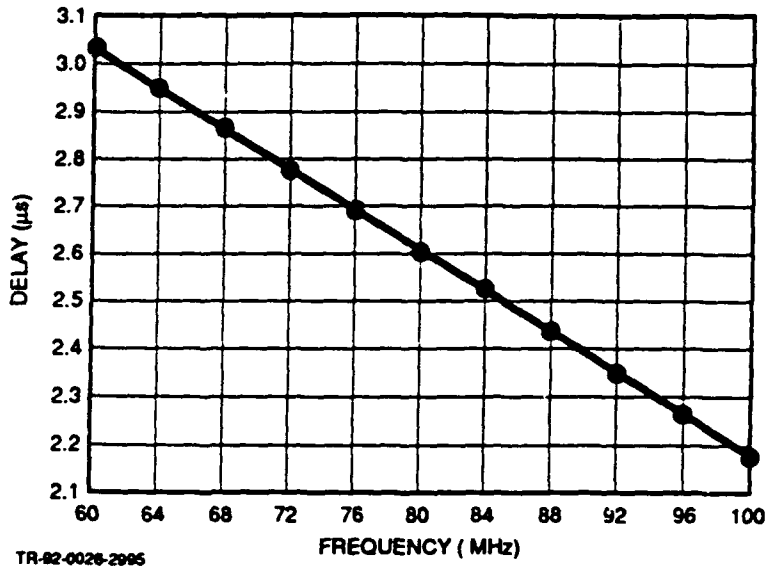

Figure 3-16. Measured AOTDL Delay Versus AOSLM Frequency

Finally, an analysis of the required focal lengths and apertures for the cylindrical and spherical lenses between the two AO cells was performed for the current longitudinal TeO_2 AOSLM and for the proposed slow-shear TeO_2 AOSLM. The focal length of the spherical and cylindrical lenses will be equal to achieve 1:1 imaging and transforming in orthogonal directions. The spherical lens focal length is found from $F_1 = T_d v_{dl} v_{slm} / \lambda B_{slm}$. With this focal length, lenses were selected from catalogs and, except for the cylindrical lenses, were purchased under this contract. Aperture sizes are determined by the focal length, diffraction angle, size of the acoustic aperture (x and y), and the focal length of the cylindrical lens preceding the AOSLM. With these considerations, figures were generated showing the shape of the diffracted beam for various focal lengths and AOSLMs. These results are shown in ***Figures 3-17 and 3-18***. In addition to the need for large apertures to contain these diffracted beams, it is desirable to employ large (4 in.) mirrors, which were also purchased. Smaller aperture optics will result in loss of system efficiency due to some of the light bypassing the optics. The slow-shear TeO_2 AOSLM offers not only smaller optics to capture the diffracted beam, but also a shorter total path length due to a smaller value of F_1.

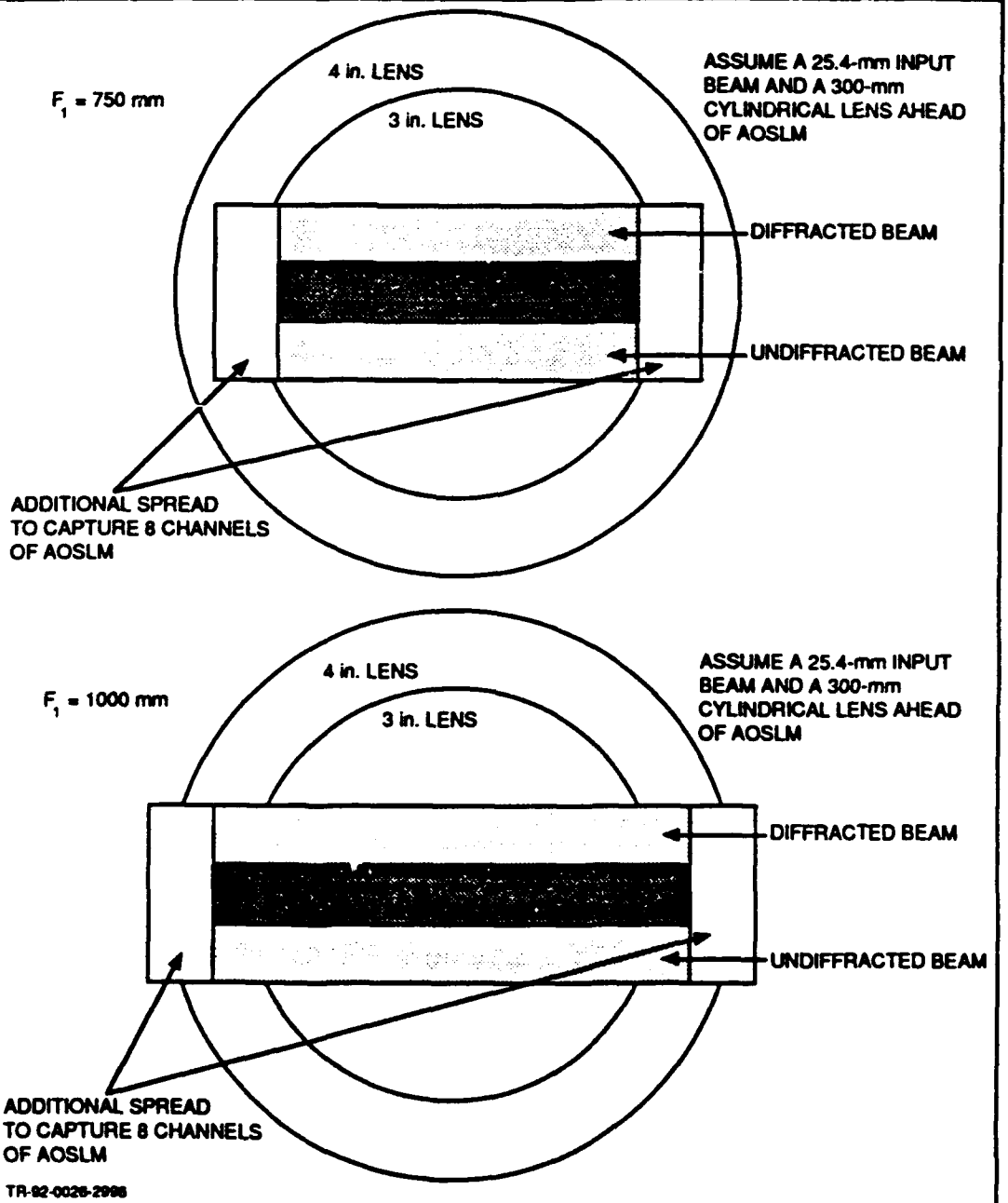

Figure 3-17. Diffracted AOSLM Beams for Longitudinal TeO_2 (Aperture = 21.1 x 22.2 mm)

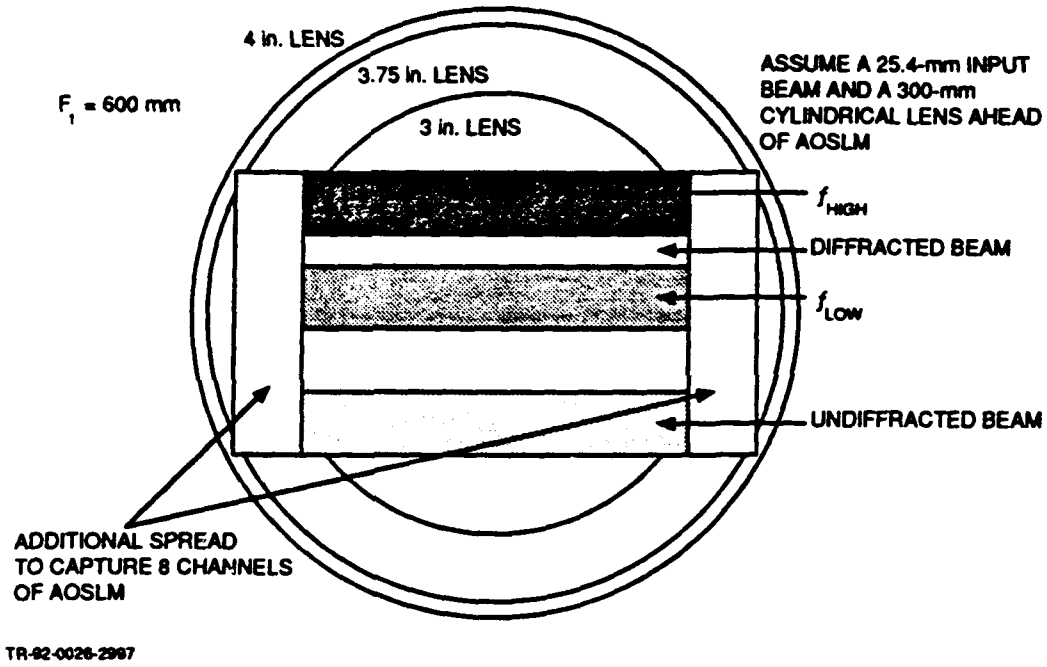

Figure 3-18. Diffracted AOSLM Beams for Slow-Shear TeO_2 (Aperture = 15.4 x 26.0 mm)

Additional theoretical development of the AOTDL, together with frequency response and crosstalk simulations and measurements, is provided in the Applied Optics draft paper in Appendix B. The simulation codes are provided in Appendix C.

4. MADOP SYSTEM TESTING

A major achievement during this effort was the initial closing of the adaptive loop between the two optical processors described in Section 3. This was achieved through 1) the RF interfacing of the two subsystems to provide common signals for processing, and 2) the development (by 1Lt. Andrews) of the software required to estimate tap weight positions and amplitudes from correlator output data and to control over GPIB a frequency generator to provide this tap signal to the AOSLM. Because of the long correlator integration times, resulting in good estimation of the interference environment, single-step cancellation in an open-loop configuration was emphasized.

4.1 MULTIPATH SIGNAL SIMULATION FOR SINGLE-STEP, OPEN-LOOP OPERATION

The electronics for simulating the multipath environment and distributing the waveforms is shown in ***Figure 4-1***. For a nominal input of 150 mW, an output of approximately 200 to 250 mW was realized in the two correlator signals and the input to the AOTDL. In addition, a low-power main channel signal (shown in the figure as the input to the canceller) is provided for cancellation with the AOTDL system output. The delay between the main channel signal and the two auxiliary channel signals (one of which is attenuated as shown in the figure) is between +0.1 and -0.4 μs. The two additional delay lines of 7.6 and 10.1 μs are used to center the delay window in the aperture of the AOTDL. All attenuators are variable except the 10-dB in-line attenuator. $ATTN_2$ is very high to effectively remove this path during this measurement.

Measurements of the frequency response of each of the paths were obtained using the network analyzer, and a representative path response is shown in ***Figure 4-2***. The response was flat in all cases to approximately 1 dB across the 75- to 85-MHz passband. Also, for the input signal shown in ***Figure 4-3***, the output shown in ***Figure 4-4*** was obtained for the AOTDL path, with the other paths being similar in appearance. This demonstrates that the intermodulation products are well down (>40 dB) from the two tones but do contribute some distortion.

4.2 CANCELLATION PERFORMANCE

For the long integration times characteristic of the current configuration, closed-loop operation implies the use of the correlation output to command the AOSLM input frequency. For many multipath scenarios, it is not necessary to feed back the error signal into the correlator for such long integration times. This was shown in Section 2. In addition, for feedback of the error, additional software modifications will be required to update the weight estimate based on the new correlation information.

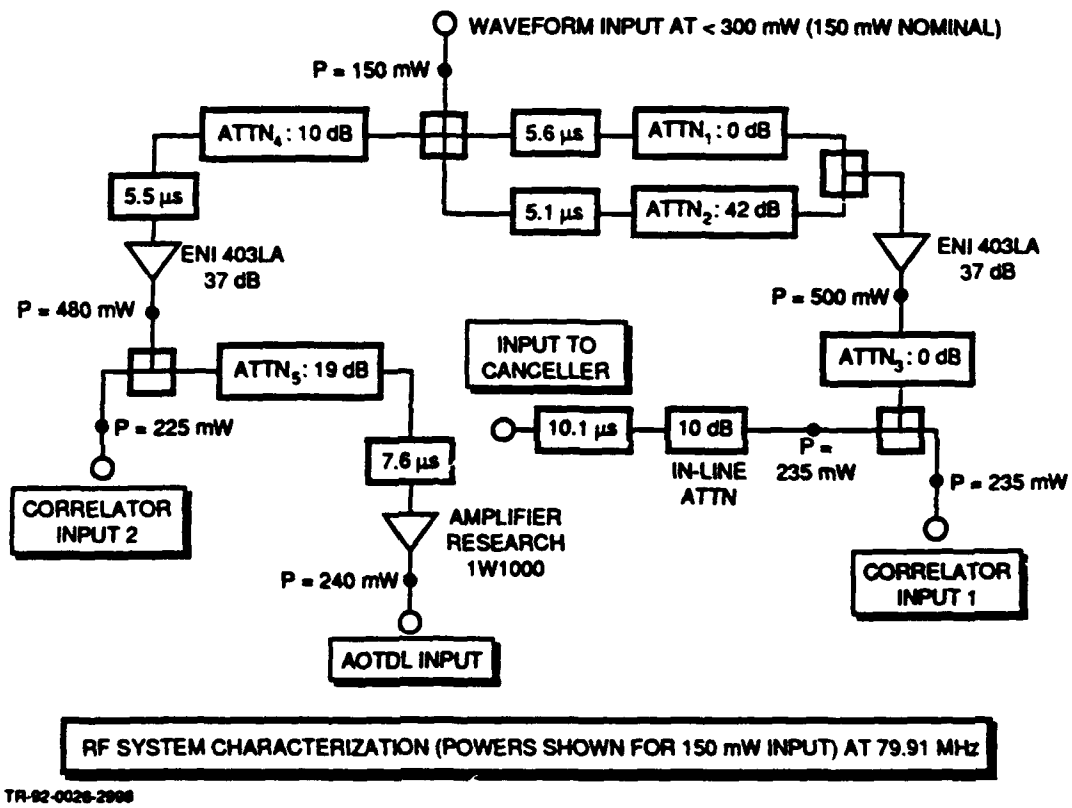

Figure 4-1. Single-Step, Open Loop Signal Generation

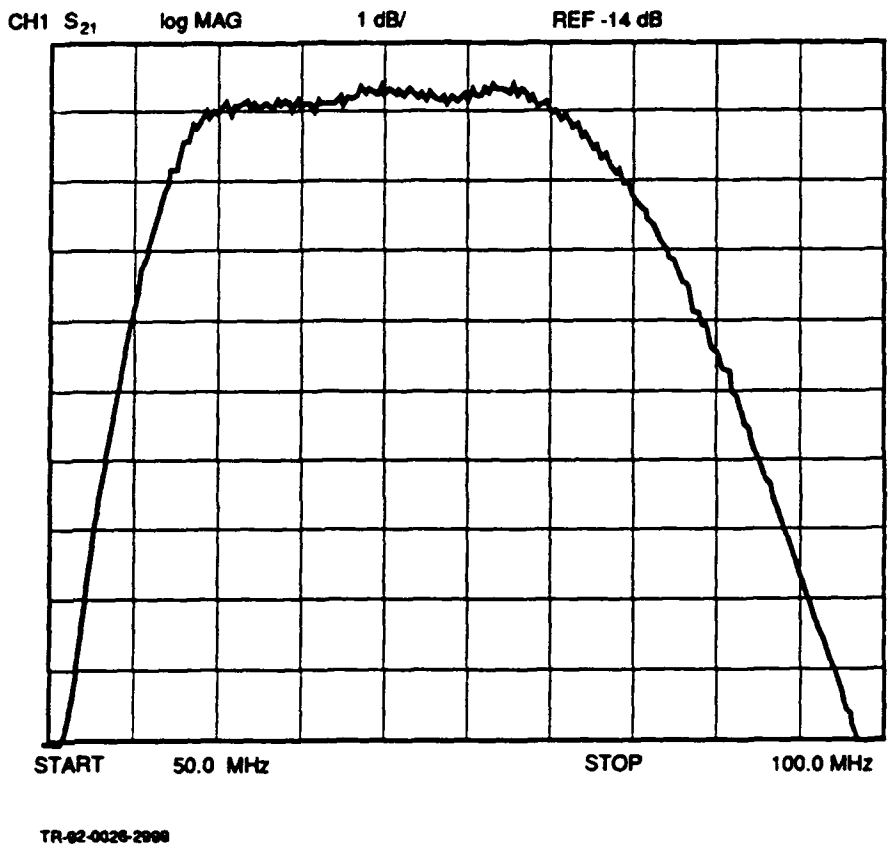

Figure 4-2. AOTDL Input Path Response

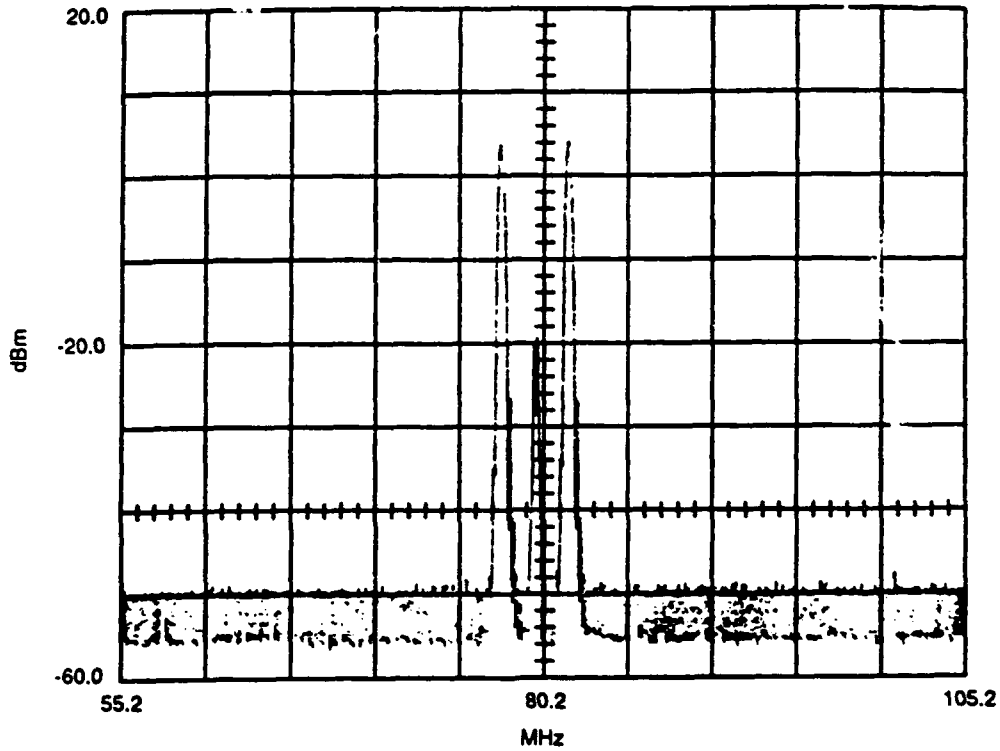

TIME: 50 ms/DIV
MAX/MIN MODE

SF 55.2 MHz	ATTN 50 dB
20 dBm	VF 3 kHz
5 MHz	10 dB
300 kHz RBW	VHF 2 V

TR-92-0026-3002

Figure 4-3. Two-Tone Signal Input

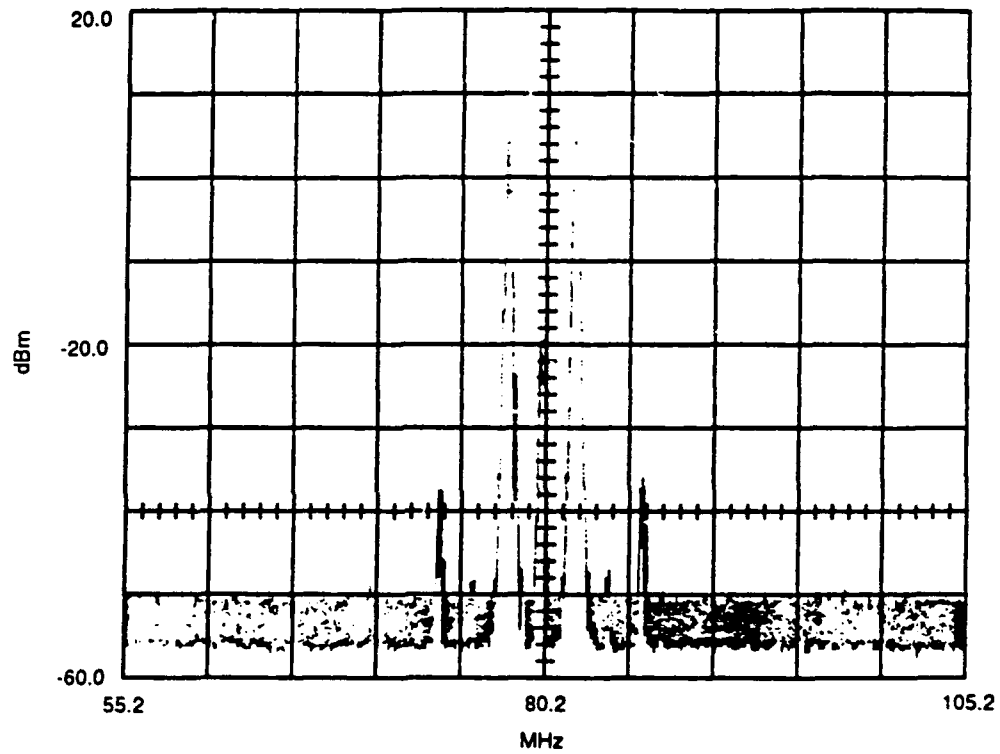

TIME: 50 ms/DIV

MAX/MIN MODE

SF 55.2 MHz	ATTN 50 dB
20 dBm	VF 3 kHz
5 MHz	10 dB
300 kHz RBW	VHF 2 V

TR-92-0026-3003

Figure 4-4. AOTDL Input Path Spectrum for Two-Tone Signal Input Shown in Figure 4-3

It is necessary to generate calibration coefficients relating delays and amplitudes in the AO correlator to those in the AOTDL. The AOTDL response was measured using the network analyzer time delay feature and was found to yield a delay-to-AOSLM frequency ratio of 0.02 μs/MHz (see ***Figure 3-16***). For the correlator, the window calibration factor was 3.0 μs/512 pixels. Therefore, the overall scaling between the two subsystems was found to be 0.28 MHz/pixel. A frequency offset and an amplitude rate and offset were also entered to achieve cancellation at a nominal system condition, but were not carefully calibrated.

During the May/June on-site support visit, the MADOP system was operated in single-step, open-loop format and was able to cancel a wideband signal (0.1-μs pulse) on an 80-MHz IF with 10 to 15 dB of cancellation. Although this occurred, it was very noisy and oscillated between cancellation and constructive interference as the tap estimate and tap power varied over several hundred kilohertz and several tenths of decibels. For manual operation, the tap frequency and power were manually set to achieve cancellation to determine the ability of the current AOTDL subsystem to cancel the 0.1-μs pulse.

Figure 4-5 shows the results of these initial measurements, taken in the manual configuration due to system instability. ***Figure 4-5 (a) and (b)*** shows the input pulse spectrum and the AOTDL output spectrum, respectively. The distortion of the pulse spectrum, especially for low frequencies, is not understood at this time since the system frequency response was fairly flat over this range (as measured on the network analyzer). Distortions exist that manifest themselves as ripple in the frequency response of the system when the 7.5-μs delay line precedes the AOTDL. These are sweep rate and start/stop frequency dependent, and imply that reflections that interfere with each other in the network analyzer are present. ***Figure 4-5 (c)*** shows the resulting cancelled signal after recombination of the two waveforms in a Mini-Circuits ZSCJ-2-1 inverting combiner. Approximately 12 dB of cancellation was achieved over this 10-MHz bandwidth. For comparison, ***Figure 4-6*** shows the input and cancelled signal for a splitter/combiner combination with equal cable lengths between the two devices and demonstrates a potential for about 32-dB cancellation of this waveform using these components.

During the August/September on-site support visit, further manual cancellation of pulses was performed. ***Figures 4-7 through 4-9*** show cancellation for pulses of 500-, 200-, and 100-ns duration, respectively. Approximately 20- to 25-dB cancellation of these pulses resulted with fairly stable cancellation over time.

As mentioned previously, due to the inaccuracy and instability of the correlator delay estimate, the stability of the single-step, open-loop performance was not good. Single-step, open-loop cancellation was achieved at intermittent times and captured on the oscilloscope, an example of which

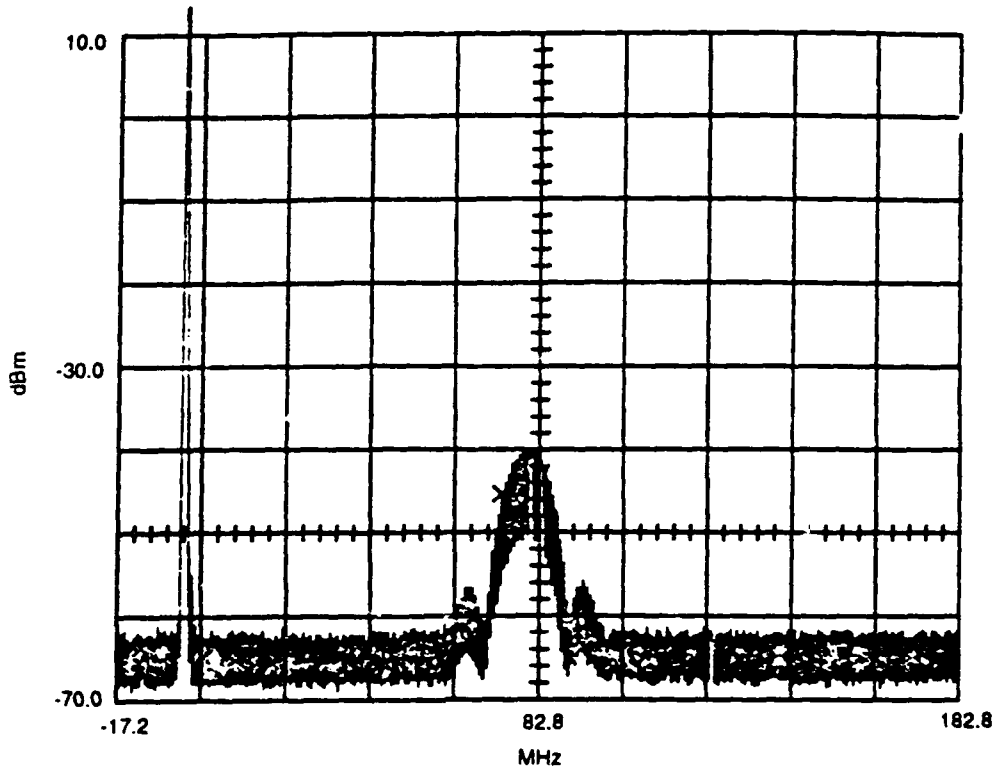

TIME: 50 ms/DIV
X - MARKER 1
MAX/MIN MODE

82.8 MHz	ATTN 40 dB
10 dBm	VF 3 kHz
20 MHz	10 dB
300 kHz RBW	M 74 MHz
	M -48.0 dBm

(a) Input 0.1-μs Pulse Spectrum

TR-92-0026-3004

Figure 4-5. Manual Cancellation Performance

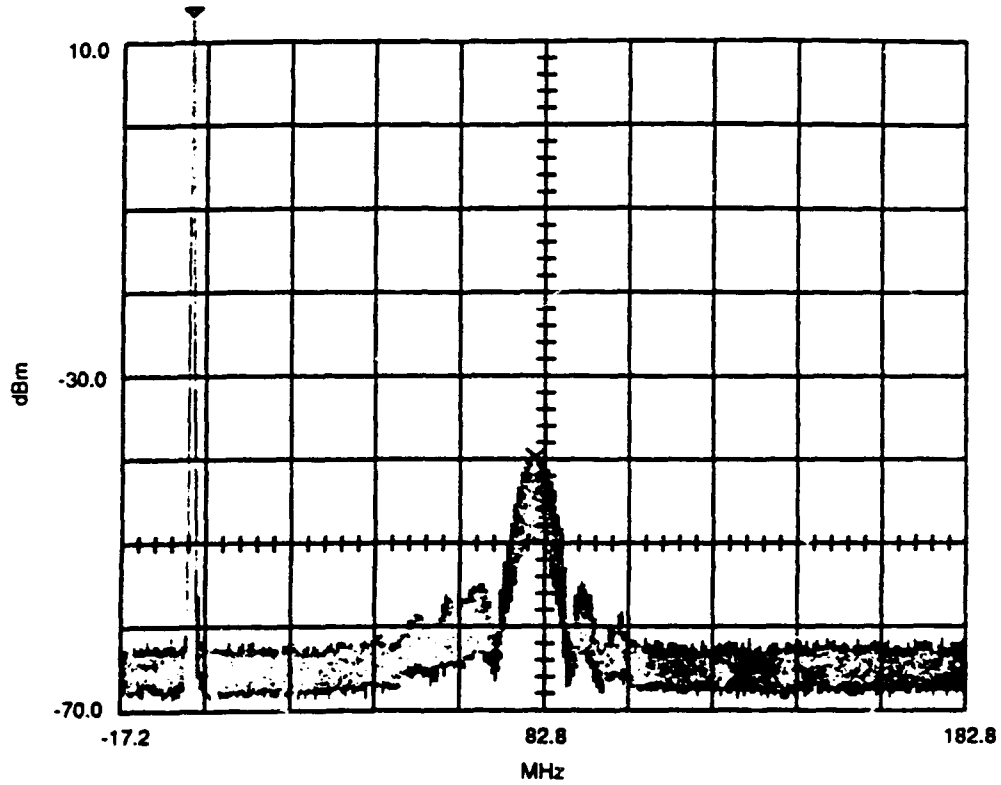

TIME: 50 ms/DIV
X - MARKER 1
Δ - MARKER 2
MAX/MIN MODE

82.8 MHz	ATTN 40 dB
10 dBm	VF 3 kHz
20 MHz	10 dB
300 kHz RBW	D 81.2 MHz
	D -58.4 dB

(b) AOTDL Output Spectrum

TR-92-0026-3005

Figure 4-5. Manual Cancellation Performance (Continued)

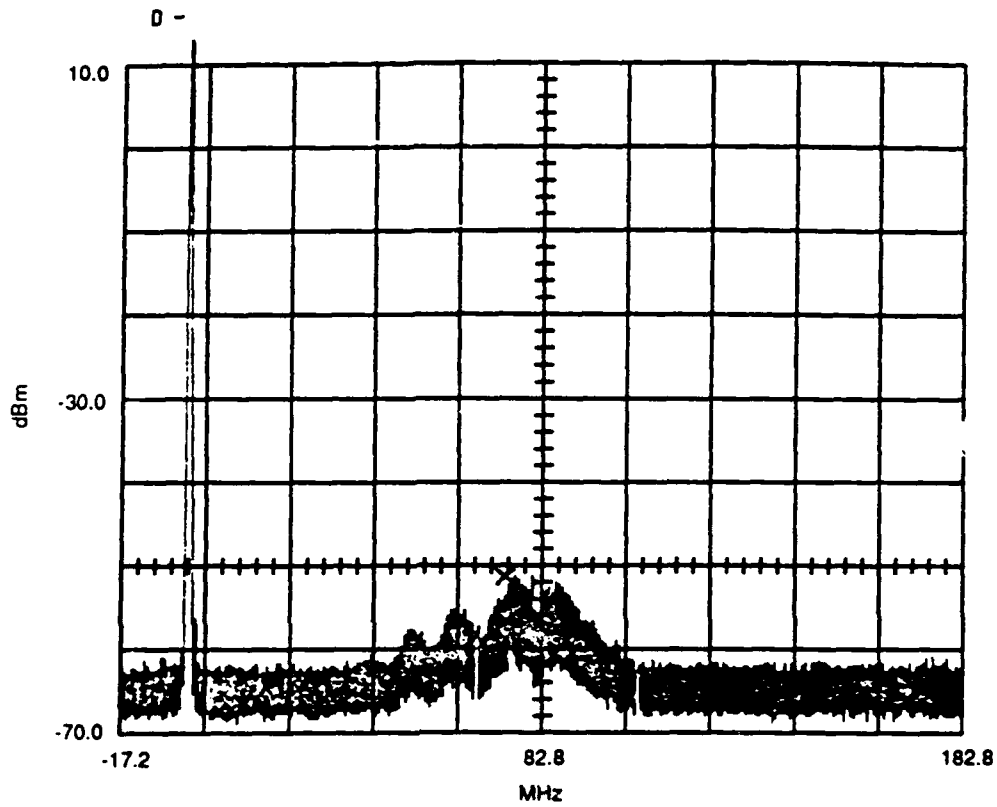

TIME: 50 ms/DIV
X - MARKER 1
MAX/MIN MODE

82.8 MHz	ATTN 40 dB
10 dBm	VF 3 kHz
20 MHz	10 dB
300 kHz RBW	M 74 MHz
	M -53.7 dBm

(c) Cancelled Signal Combined Using ZSCJ-2-1 Inverting Combiner

TR-92-0026-3006

Figure 4-5. Manual Cancellation Performance (Concluded)

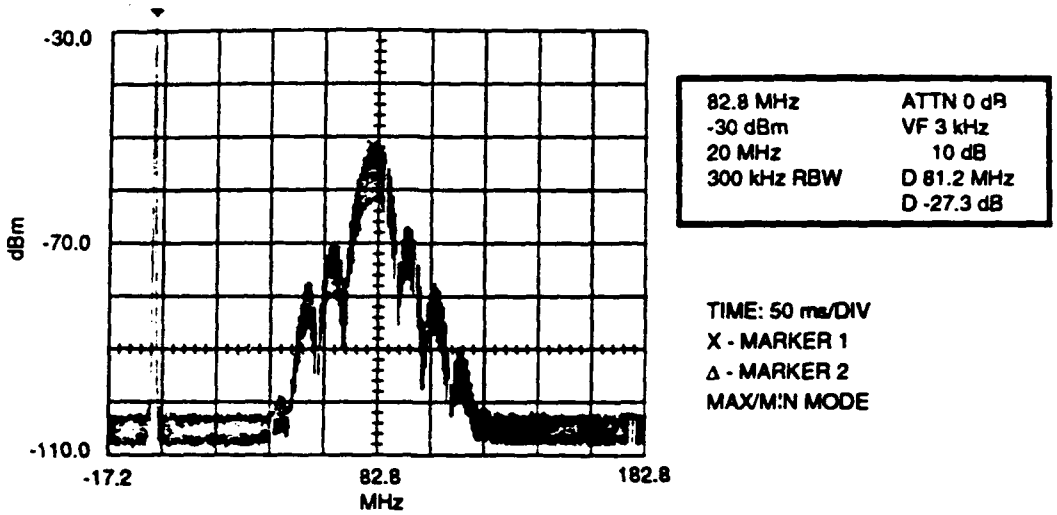

(a) Input Pulse Signal

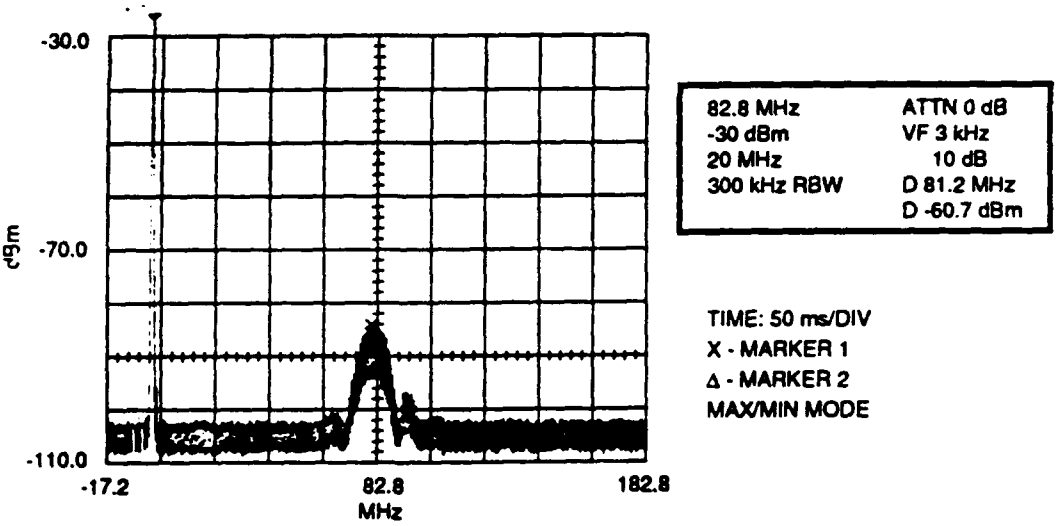

(b) Cancelled Pulse Using Splitter and Combiner

TR-92-0026-3007

Figure 4-6. Splitter/Combiner Cancellation Performance

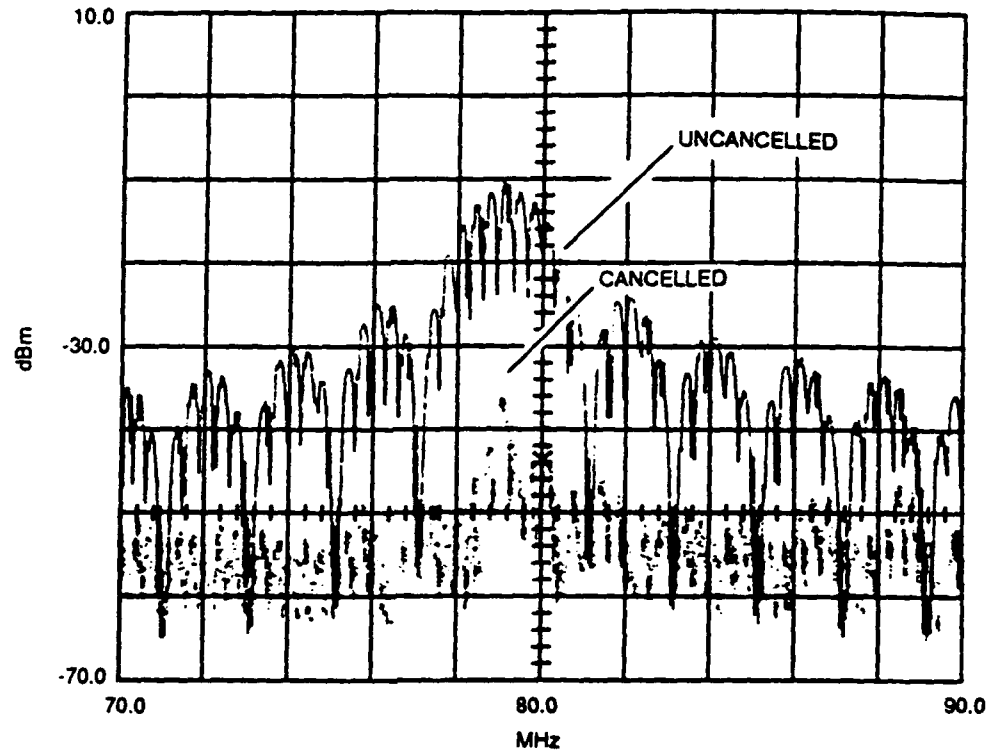

TIME: 50 ms/DIV
X - MARKER 1
MAX/MIN MODE

SF 70 MHz	ATTN 40 dB
10 dBm	VF 3 kHz
2 MHz	10 dB
300 kHz RBW	M 80 MHz
	M -48.4 dBm
	VHF 4 A

TR-92-0026-3009

Figure 4-7. Pulse Cancellation (τ = 500 ns, PRI = 3 μs, A = 200 mVp-p, 100 mV Offset)

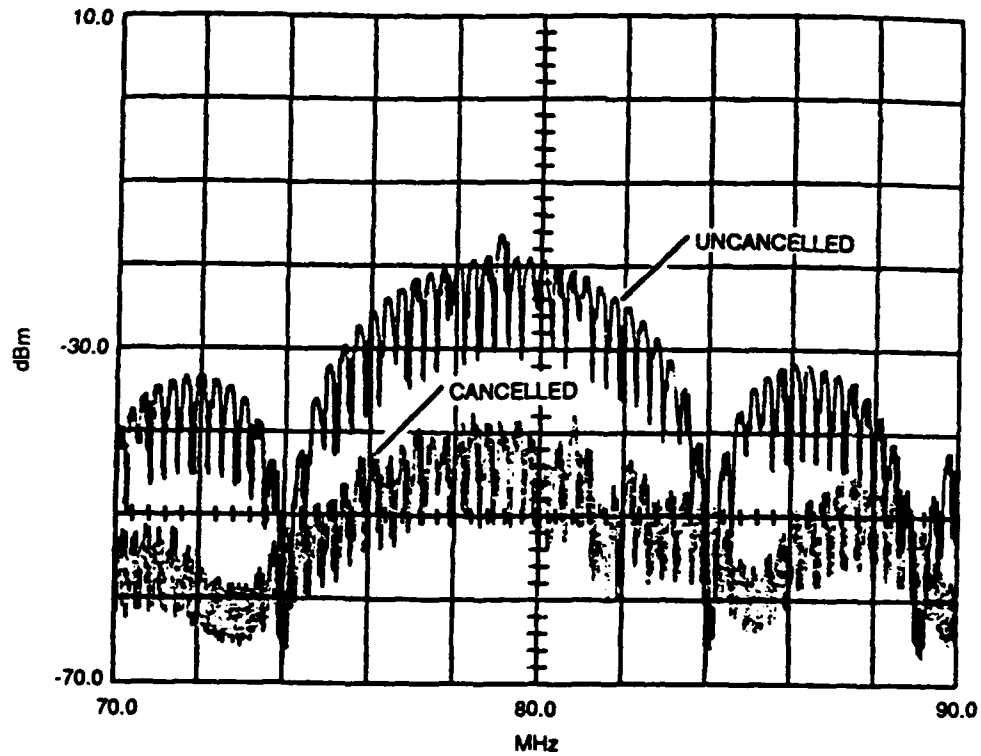

TIME: 50 ms/DIV

MAX/MIN MODE

SF 70 MHz	ATTN 40 dB
10 dBm	VF 3 kHz
2 MHz	10 dB
300 kHz RBW	
	VHF 4 A

TR-92-0026-3010

Figure 4-8. Pulse Cancellation (τ = 200 ns, PRI = 3 μs, A = 200 mVp-p, 100 mV Offset)

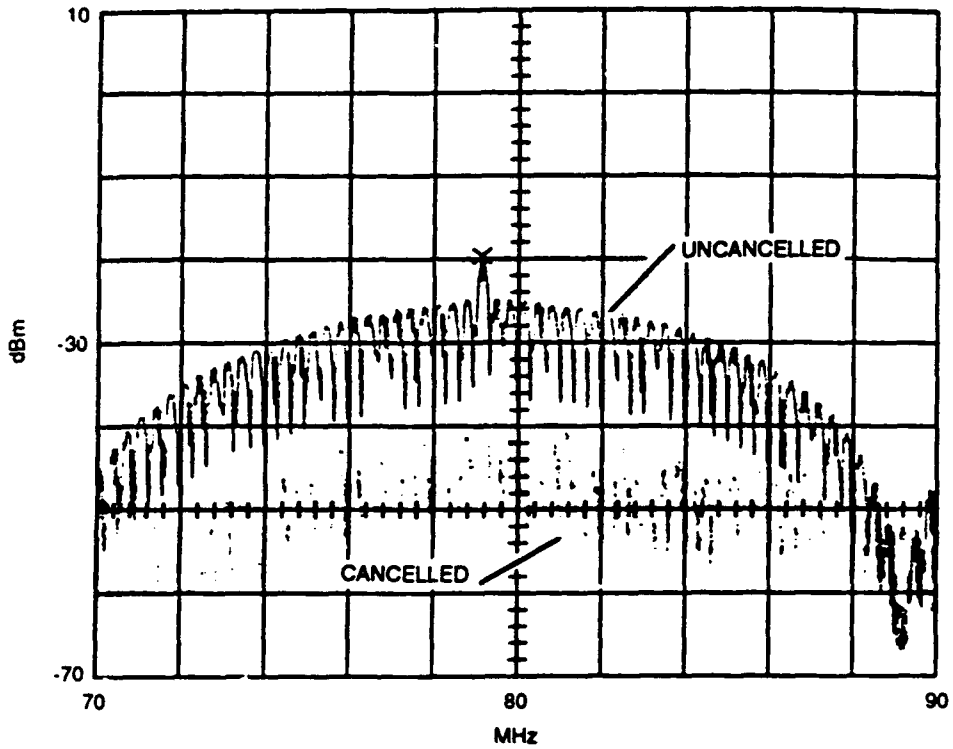

TIME: 50 ms/DIV
X - MARKER 1
MAX/MIN MODE

SF 70 MHz	ATTN 40 dB
10 dBm	VF 3 kHz
2 MHz	10 dB
300 kHz RBW	M 79.12 MHz
	M -21.7 dBm
	VHF 4 A

TR-92-0026-3011

Figure 4-9. Pulse Cancellation (τ = 100 ns, PRI = 3 μs, A = 200 mVp-p, 100 mV Offset)

is shown in ***Figure 4-10***. It is seen that for this two-tone waveform, the two sideband tones are cancelled at approximately 25 and 30 dB, whereas the carrier is not cancelled (the reason for the lack of carrier cancellation in this experiment has not been determined). This demonstrates the promising cancellation performance that should be achieved when the system is stabilized using the locking circuit described in the next subsection.

4.3 SYSTEM STABILIZATION WITH A SINGLE-LOOP ELECTRONIC CANCELLER

Analysis was undertaken to determine the required tap accuracy based on the AO correlator output. A first requirement is that the output from the photodiode in the AOTDL architecture, which is at the 80-MHz IF, must be kept very stable in order to cancel the main channel signal at the IF. ***Figure 4-11*** shows this relationship, where ***Figure 4-11 (a)*** shows the power in the cancelled signal for phase errors from 0° to 360°. This scale is expanded and put on a log scale in ***Figure 4-11 (b)*** to show the cancelled signal power for phase errors from 0° to 20°. Note that at a phase error of 1.44°, the power is down 38 dB; at 2.88°, the power is down 32 dB; and at 4.32°, the power is down 28.5 dB. This phase error puts an ultimate limit on the ability to cancel signals at the system IF, and implies a required phase accuracy of the AOTDL architecture of better than 3° to achieve 30 dB of cancellation.

To achieve the high degree of phase accuracy in the AOTDL, the tap must be accurate to within 3°, or 0.104 ns at 80 MHz. For a 1-μs delay window for an AOSLM input covering a 60- to 100-MHz frequency spread, the system must be able to resolve the tap position to within one part in 9215, or an AOSLM input accuracy of 4.16 kHz. Therefore, a very accurate estimate must be achieved from the data supplied by the AO correlator subsystem.

An alternative approach that appears to offer significant promise is to estimate the correlation peak location and amplitude as well as possibly using currently implemented techniques, and to then employ an adaptive system after the AOTDL to lock the phases of the two carriers together. This is similar in concept to a sidelobe canceller architecture, which attempts to cancel the carrier of the waveform without regard to the envelope, which is assumed to be a low bandwidth relative to the inverse delay time. The combination of the MADOP with such a sidelobe canceller architecture was suggested during the prior year's ESE effort (see Subsection 2.1.2 of Reference 1) but in a different context. Several approaches to the locking circuit were proposed and analyzed, and the best approach was found to be the classical single-loop adaptive canceller described in Reference 7. The operation of this proposed locking system is described below.

A single LMS loop utilizing a single complex weight is shown in ***Figure 4-12***. For the MADOP application, the AOTDL output is multiplied by weight (w) then subtracted from the main channel signal to create the error signal. This error signal is then mixed with the AOTDL output and

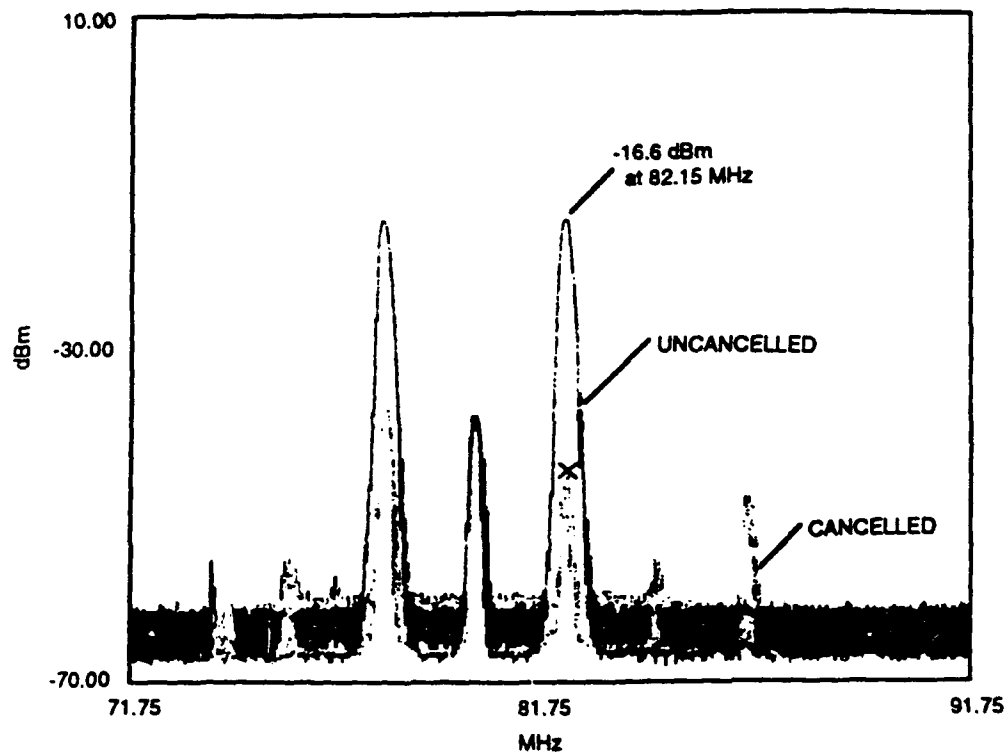

TIME: 50 ms/DIV
X - MARKER 1
MAX/MIN MODE

SF 71.75 MHz	ATTN 40 dB
10 dBm	VF 3 kHz
2 MHz	10 dB
300 kHz RBW	M 82.15 MHz
	M -47.4 dBm
	VHF 4 A

TR-92-0026-3012

Figure 4-10. Single-Step, Open-Loop Operation - Reference + AOTDL Output (~ 30 dB Cancellation at 82.15 MHz)

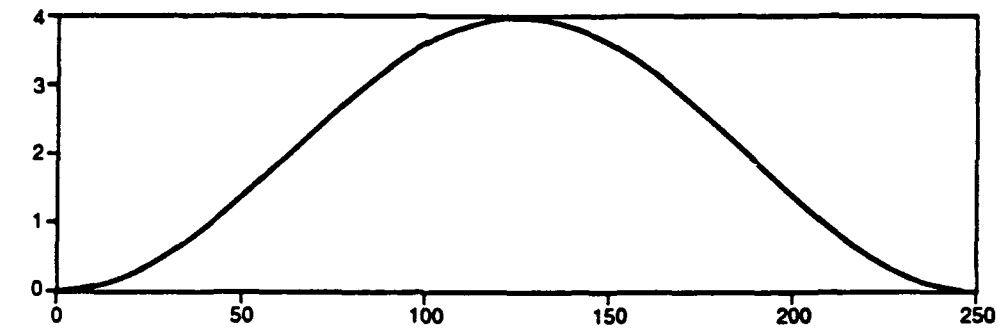

(a) Error Squared of Cancelled Signal, 1 deg = 0.69 Samples

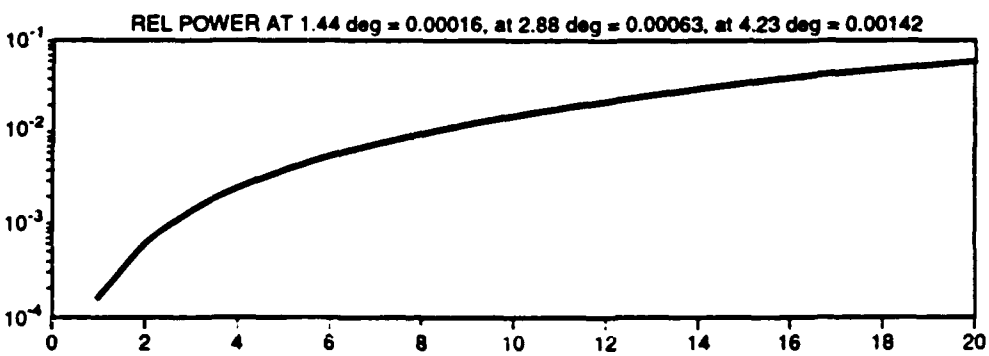

(b) Magnification Error Squared

TR-92-0026-3013

Figure 4-11. Phase Stability Effects on Signal Cancellation

integrated (with gain) to form the desired weight. The multiplication of the error signal with the AOTDL output effectively implements a phase detection process. To effect the phase of a signal on a carrier, the weight (w) must be complex. This is achieved by applying a quadrature hybrid splitter and two weights as shown in ***Figure 4-13***. The effective complex weight for the two real quadrature weights (w_I and w_Q) is given as:

$$w = \sqrt{w_I^2 + w_Q^2}\, e^{-jTan^{-1}(w_Q/w_I)} \tag{4-1}$$

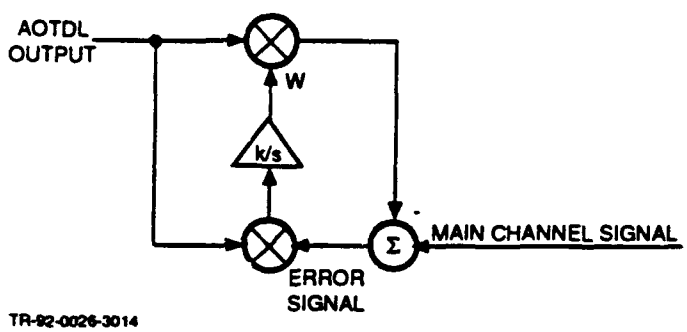

Figure 4-12. Classical Single-Weight LMS Loop

The architecture implemented in the hardware for this cancellation application is shown in ***Figure 4-14***. For this architecture, each output from the quadrature hybrid splitter feeds its own phase detection mixers to derive the respective weights at the output of the two integrators. This circuit was built during the October on-site support visit using the low-pass filter (LPF)/integrators, described in greater detail in Appendix A, and other hardware purchased for this application. This architecture performed very well during the on-site support visit, and cancellation on the order of 25 to 30 dB was achieved for both a sinusoidal input and a two-tone input. After attaining successful initial operation, the circuit quit operating properly and was not again successfully operated on-site.

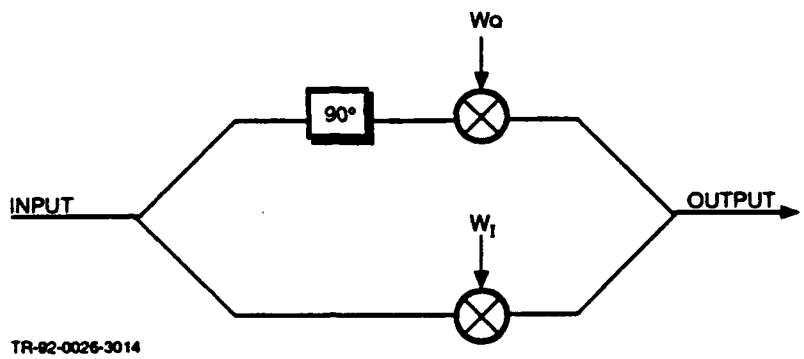

Figure 4-13. Implementation of a Complex Weight

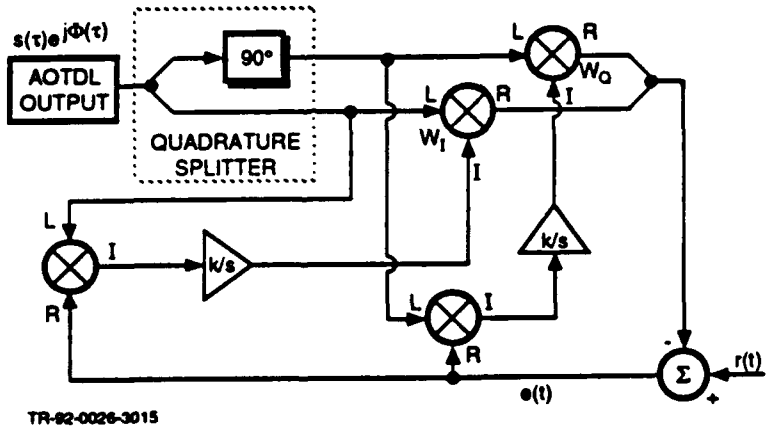

Figure 4-14. Single-Loop Electronic Canceller to Cancel Effects of Carrier Drift

Later efforts by Captains Ward and Keefer resulted in successful operation, possibly as a result of increased gain applied to the weighted AOTDL output that subsequently feeds the subtractor.

A simulation of the algorithm described above was developed using Simulink (a high-level graphical driver for MATLAB) to assess the optimum choice of LPF/integrator and the effects of variable gain on the system cancellation performance. Simulink allows the user to code the simulation at a block diagram level, as shown in ***Figure 4-15***. Representative outputs from the display devices shown on the Simulink layout are shown in ***Figure 4-16***. It was found for all test cases that the use of pure integrators in the feedback paths is preferable to the use of LPFs.

4.4 RECOMMENDED WEIGHT FUNCTION CALCULATION ALGORITHM

Even with the benefit of the single-loop electronic canceller, care must still be taken to generate an accurate estimate of the correlation peak information. The following analysis suggests improvements to the currently implemented peak-picking algorithm.

This problem is approached by first examining the AO correlator translation of the system IF down to a lower IF for spatial sampling by the linear detector array. Let the input to a conventional IF correlator be given as:

$$s_1(t-\tau_d) = a_1(t-\tau_d)\exp\left[j2\pi f_{if}(t-\tau_d)\right] \tag{4-2}$$

and

$$s_2(t) = a_2(t)\exp\{j2\pi f_{if}t\} \tag{4-3}$$

where $a_1(t)$ and $a_2(t)$ are complex modulations, f_{if} is the system IF (80 MHz), and τ_d is the relative signal delay. The correlation, as a function of correlation delay, is then given as:

$$\begin{aligned} R(\tau,\tau_d) &= \int_0^T s_1(t)\,s_2^*(t-\tau_d)\,dt = \int_0^T a_1(t-\tau_d)\,a_2^*(t-\tau)\exp\left[-j2\pi f_{if}(\tau-\tau_d)\right]dt \\ &= R_{12}(\tau-\tau_d)\exp\left[-j2\pi f_{if}(\tau-\tau_d)\right] \end{aligned} \tag{4-4}$$

where it is observed that the output is given as the cross-correlation of $a_1(t)$ and $a_2(t)$ with the correlation peak and IF carrier shifted by τ_d. Also note that at the peak of an autocorrelation for which $a_1(t)$ and $a_2(t)$ are the same signal (characteristic of multipath), the phase of the IF carrier will be zero. This implies that the carrier will always peak at the center of the correlation peak.

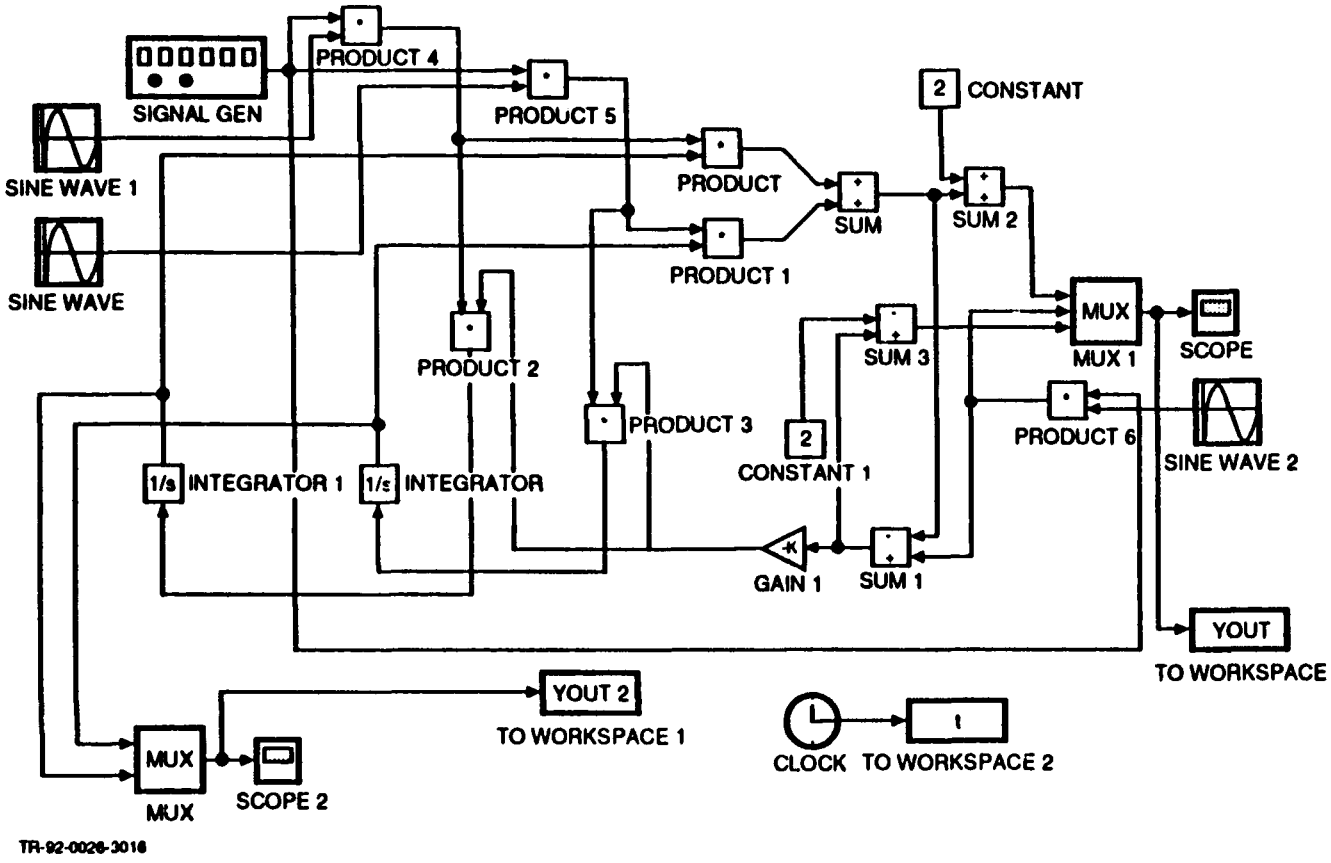

Figure 4-15. Simulink Structure for Single-Loop Electronic Canceller Simulation

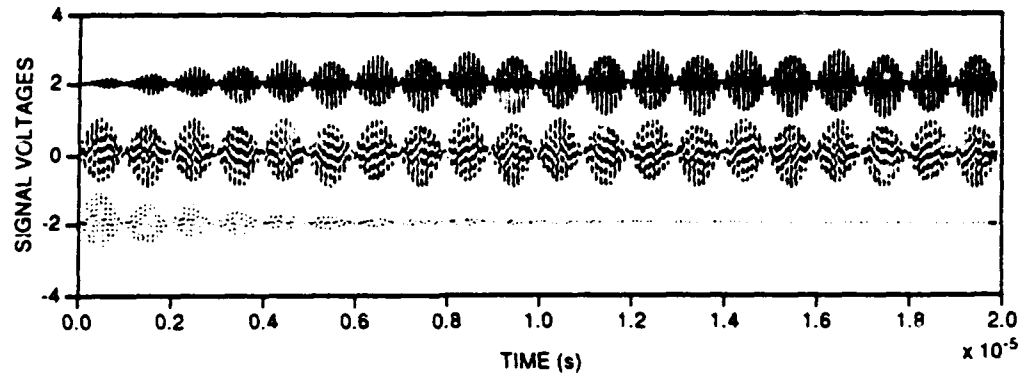

(a) Adapted Signal, Desired Signal, and Canceled Signal

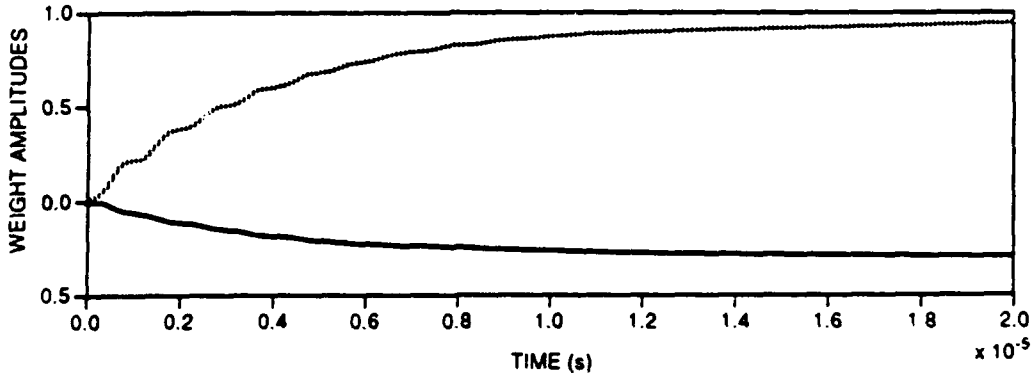

(b) I&Q Channel Weights

TR-92-0026-3017

Figure 4-16. Simulated Single-Loop Electronic Canceller Performance

For the correlator, the carrier frequency appearing spatially on the detector array is at a different IF than the system IF. Mathematically stated:

$$R(\tau,\tau_d)=\int_0^T s_1(t)\exp\left[j\pi f_\delta\tau\right]s_2^*(t-\tau)\exp\left[j\pi f_\delta\tau\right]dt = \exp\left[j2\pi f_\delta\tau\right]R_{12}(\tau-\tau_d)\exp\left[-j2\pi f_{if}(\tau-\tau_d)\right] \quad (4\text{-}5)$$

where f_δ is the difference between the system IF and the detected spatial IF. Now the phase at the correlation peak ($\tau = \tau_d$) is given by $2\pi f_\delta\tau$ in radians. It is this phase that is used to calculate the required tap position with high accuracy. At $\tau = \tau_d$, the phase is thus $\Phi_d, = 2\pi f_\delta\tau$. By measuring the phase of the carrier at the estimate of the correlation peak, the delay can then be accurately determined by:

$$\tau_d = \Phi_d/2\pi f_\delta \quad (4\text{-}6)$$

A MATLAB simulation ("peakpk") of this tap estimate technique is included in Appendix C, and a representative output is shown in ***Figure 4-17***. The system first estimates the correlation peak location by using a tri-fit to the three highest peaks of the absolute value of the correlation. The correlation is then downconverted in in-phase and quadrature (I&Q) channels to obtain both the correlation magnitude and phase. The two reference oscillators are obtained for a zero-delay autocorrelation of the 80-MHz carrier. The equivalent spatial frequency of the 80-MHz carrier and the resulting lower frequency spatial carrier are required as inputs, together with the correlation peak location (for simulating the correlation signal) and the correlation width (between zeros of the sinc(x) function). The phase of the correlation is then used in the above equation for calculating τ_d, which is periodic at the frequency of the spatial carrier. Two values of τ_d are calculated that straddle the tri-fit peak estimate, and the closer of the two values is selected for the tap. For the case shown in ***Figure 4-17***, the absolute value of the correlation is plotted, together with a magnified version centered on the true delay. The tri-fit estimated the peak position to be at 298.03 for an actual offset of 297.40. The magnitude and phase are then calculated and plotted, the phase is measured at the tri-fit correlation peak location, and the precise delay is calculated, in this case, correctly. For this method, about 1 in 20 tap positions results in erroneous tap estimates. In all cases, the tap estimate is off by $1/f_\delta$, because the phase measurement is exact.

A version of the simulation ("peakpknsy") was also developed that adds zero-mean Gaussian noise to the correlation value before processing. ***Figure 4-18 (a) through (c)*** shows the effects of this Gaussian noise. As the noise variance increases, the tri-fit estimate becomes worse, and the final delay estimate hops to a new value. This new value is off by approximately a multiple of $1/f_\delta$, but is not at

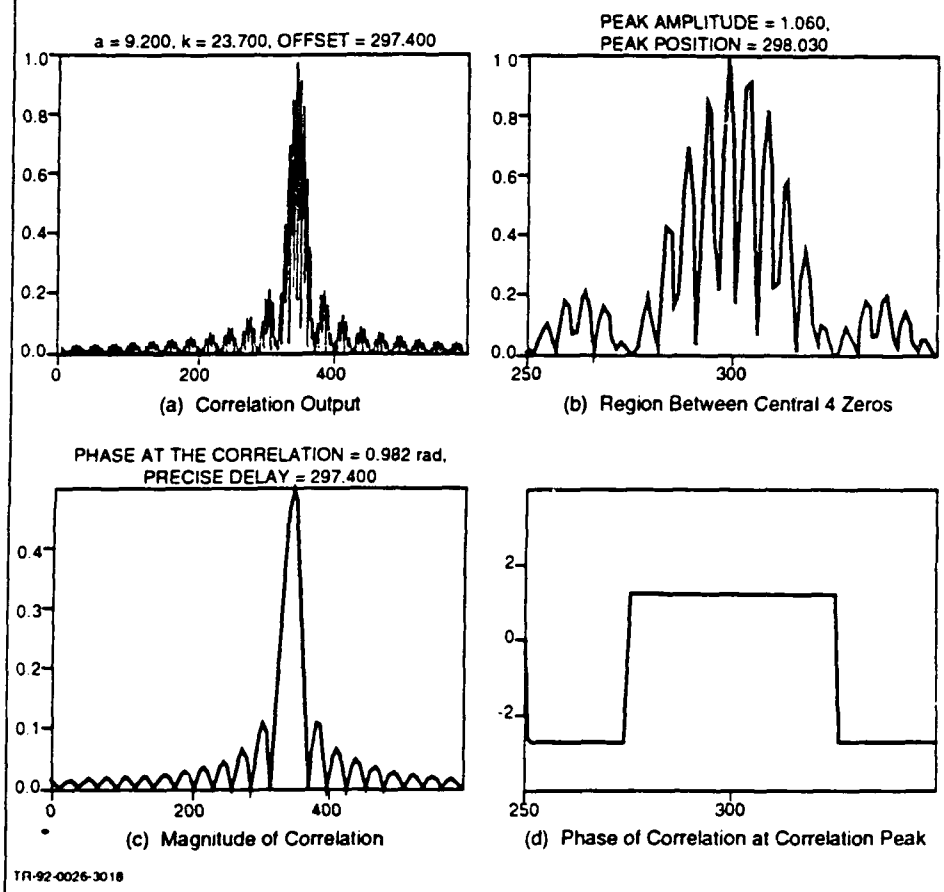

Figure 4-17. Enhanced Peak Picking Results

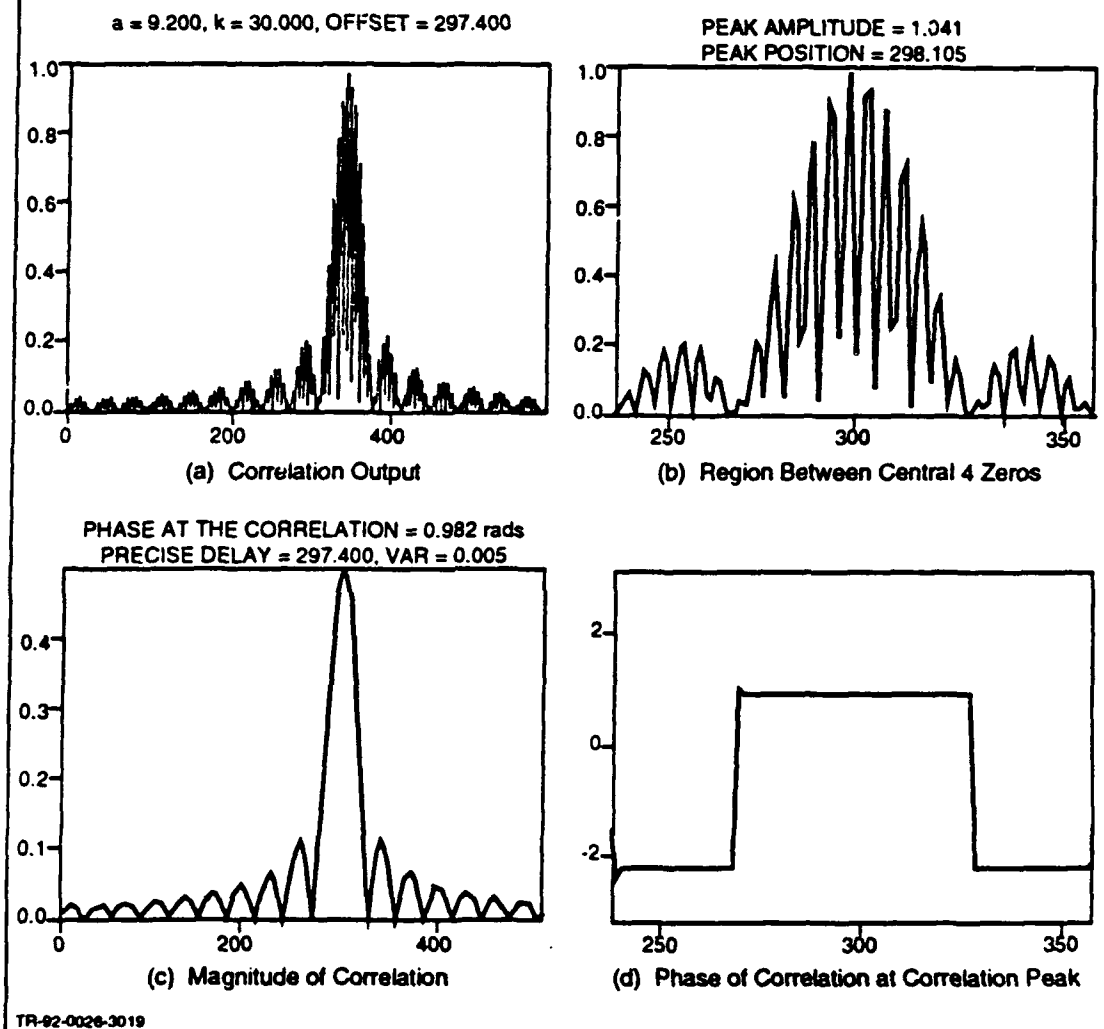

Figure 4-18. Noisy Peak Picking Results

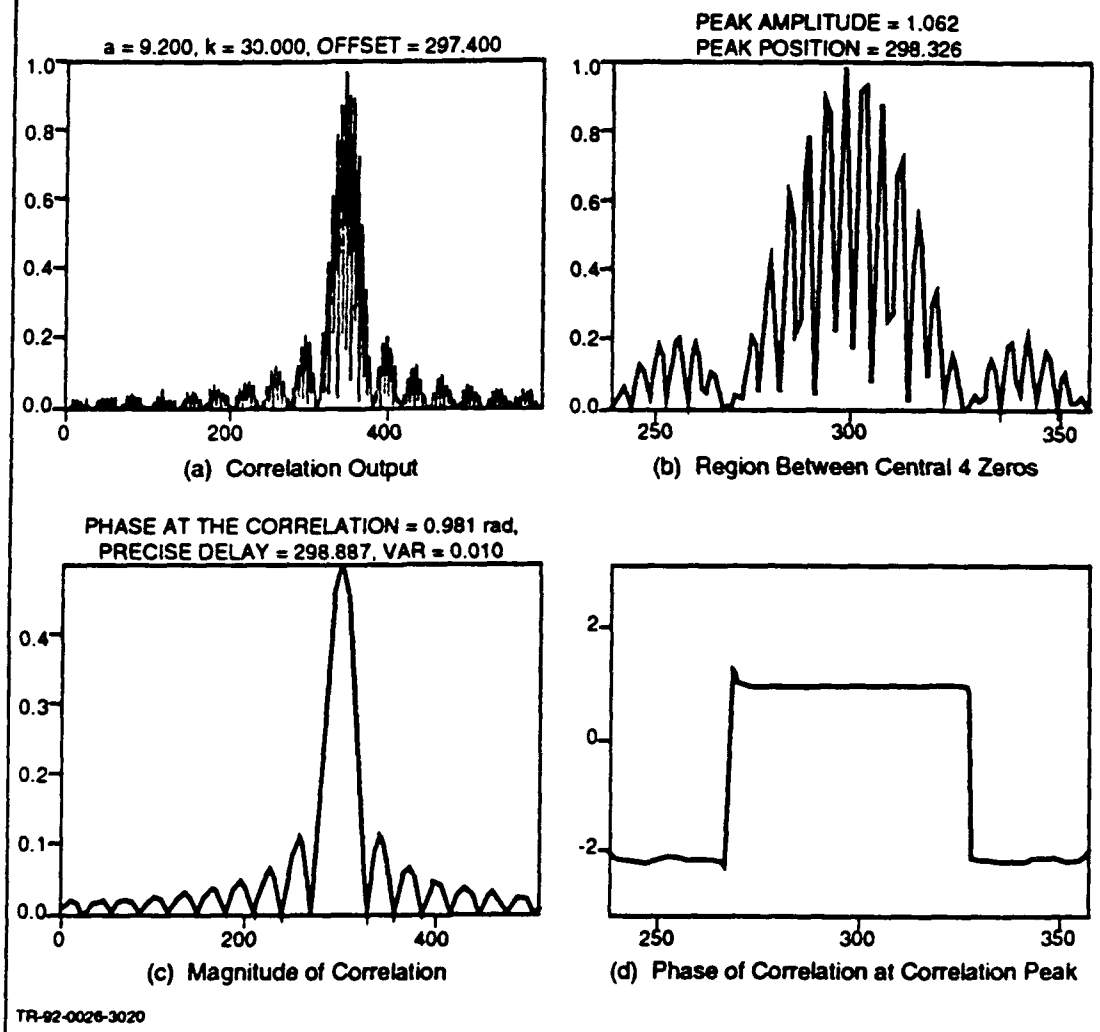

Figure 4-18. Noisy Peak Picking Results (Continued)

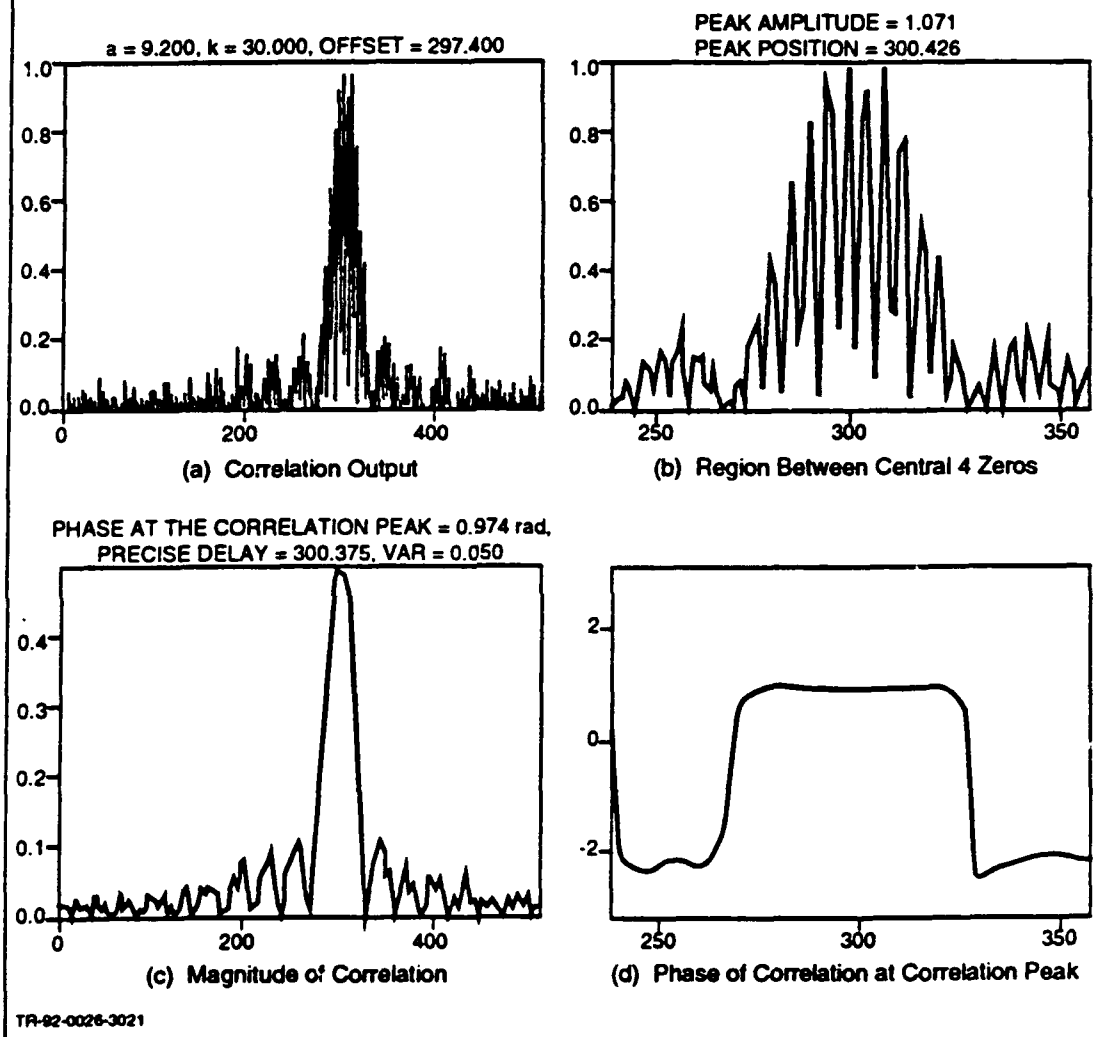

Figure 4-18. Noisy Peak Picking Results (Concluded)

exactly such a multiple since the phase measurement is now noisy. These calculations show the effects of correlation noise, and should provide requirements for AO correlator stability.

Based on this analysis, it is recommended that the following procedure be followed:

1. When the correlator system is ready to collect and process data with the zero-delay position of the correlation at pixel 256 (this may be difficult to know exactly), and the window span is known accurately (in order to determine the 80-MHz equivalent spatial carrier using the equation $1/f_{if}$ = (80MHz)(time window)/(512 pixels)), insert a zero-delay 80-MHz carrier. Collect this output and perform the correction processing (background subtraction, bias removal, gain nonuniformity removal, etc.) but not the absolute value. This acts as the in-phase reference oscillator.

2. Measure as accurately as possible the spatial carrier frequency in units of cycles/pixel.

3. In memory, shift the in-phase reference oscillator by 90° to obtain the quadrature reference oscillator. As a test of the accuracy of the phase shift, multiplication of these two functions followed by low-pass filtering (fast-Fourier transform (FFT), window, and inverted FFT) and taking the absolute value should yield a very small-valued vector.

4. Collect the test signal correlation and, after performing the correction processing, perform a tri-fit (or other fit) to the absolute value of the correlation to obtain the first delay estimate.

5. Using the bipolar correlation, downconvert in I&Q channels to obtain a phase measurement at the tri-fit delay position.

6. Using the algorithm described above, calculate the new estimate of the delay position and convert to a frequency to drive the AOTDL system.

The penalty for using this algorithm is the increased computations required to calculate the new estimate of the delay position, including down conversion in I&Q channels, and the additional requirement for *a priori* measurement of spatial carrier parameters. It is recommended that before this algorithm is implemented, the MADOP system be evaluated using the single-loop electronic canceller to assess performance without the above enhanced accuracy tap position estimation.

(Reverse Blank)

5. CONCLUSIONS AND RECOMMENDATIONS

Progress over the current and prior ESE efforts has been steady and on track for demonstration of the MADOP in FY93. A number of the challenges to making the system compatible with insertion into the C-band radar test-bed in the OC Surveillance Directorate at Rome Lab have been successfully met. Several activities remain to be completed as described below. Some of these activities are near term (bold type), while others are fairly long term.

OPTICAL SUBSYSTEMS

1. Implement the large aperture AOTDL subsystem using a slow-shear TeO_2 cell for the AOSLM and the new lenses.

2. **Generate the calibration coefficients for the two subsystems.**

3. **Generate a look-up table of amplitudes versus tap frequency to equalize any nonuniform frequency response of the AOSLM.**

RF SUBSYSTEMS

1. **Further develop the single-loop electronic canceller circuit described in Section 4 and Appendix A.**

2. Provide computer-controlled switches at the two correlator inputs to perform automatic background subtraction.

3. Provide AGC control of the RF inputs to the correlator.

4. Feed the error signal back to the correlator for high-speed operation when short integration times are practical.

DIGITAL/COMPUTER INTERFACE

1. Develop automatic algorithm for background subtraction with switches at the RF inputs to the correlator to turn one signal off at a time.

2. **Keep tri-fit algorithm constrained to a region around the peak to avoid using points from separate correlation peaks that appear in the window.**

3. **Select only those peaks that are within the window of the MADOP, as set by the window of the AOTDL subsystem (central 1/3 of correlation window).**

4. Configure the system to handle multiple taps.

5. Configure the system to handle feedback of the error signal to update the tap weight information.

6. Develop algorithms to utilize the AGC information in the tap amplitude calculation.

The primary advantage of the MADOP is cancellation of multipath delays much greater than the inverse signal bandwidth, which negates the effectiveness of classical sidelobe canceller systems. Because of our studies using the Block-LMS and OJC simulations, we feel that there is significant potential for the MADOP system in realistic scenarios. This is especially true when the environment is predominantly stationary over millisecond timeframes. In these cases, the single-step open-loop approach (residual error is not fed back to the correlator) should offer satisfactory cancellation performance due to the accurate estimates of the multipath delays and resulting tap positions. For severe multipath environments consisting of significantly greater multipath in the auxiliary channels than in the main channel, cancellation will be difficult for any adaptive system.

APPENDIX A. ANALOG DESIGNS FOR SINGLE-LOOP ELECTRONIC CANCELLER

A.1 ANALOG SINGLE-LOOP ELECTRONIC CANCELLER

Figures A-1 and A-2 contain, respectively, block and circuit diagrams of the electronic canceller discussed in Section 4. The two figures are similarly drawn so that it is possible to see where the various splitter/combiners and mixers were used to represent the various functional parts of the block diagram. All of the splitter/combiners and mixers are manufactured by Mini-Circuits. These were chosen on the basis of their availability in the Photonics Center. The error signal circuits shown in the figures will be discussed below.

The canceller operates at the OJC IF of 80 MHz, except for the error signal circuits, which operate at baseband. The 80-MHz IF is the reason that the junctions of ***Figure A-1*** were implemented with splitters, the summers were implemented by combiners, and the multiplication operation was implemented by mixers. The interconnects between the components were effected through the use of coaxial cables because of the prototype nature of the system. This led to a cumbersome implementation that was very difficult to troubleshoot. It is suggested that future implementations use some type of breadboard configuration to reduce the size of the canceller and increase its reliability.

When the canceller was implemented, its operation was very sensitive to the signal levels at various points in the circuit. This was caused by limitations on the various mixers and splitter/combiners that were used. For example, situations were encountered where the error signal circuits saturated the mixers and where signal levels at other places were too low to support proper operation of the components. After getting the circuit to work on the second day of a recent visit, the time was spent trying to determine the source of the difficulties so that Photonics Center personnel could make the circuit work.

Captains Keefer and Ward modified the circuit depicted in ***Figure A-2*** to produce the circuit depicted in ***Figure A-3***. As can be seen, the major modifications were the inclusion of some attenuators, some filters, and an amplifier. For purposes of monitoring system operation, splitters were added. One of the two-way splitters was replaced with a three-way splitter. It is assumed that the unused terminals of the monitoring splitters were terminated in 50-Ω loads. Captains Keefer and Ward indicated that the canceller worked well when implemented as shown in ***Figure A-3***.

Figure A-4 contains a functional schematic diagram of the error signal circuits of the electronic canceller. Two such circuits were constructed, one for each of the I&Q channels of the canceller. The circuits were constructed using the LM308 operational amplifier. This amplifier was chosen because it was available in the Rome Laboratories Stores Facility. Since the error signal circuit

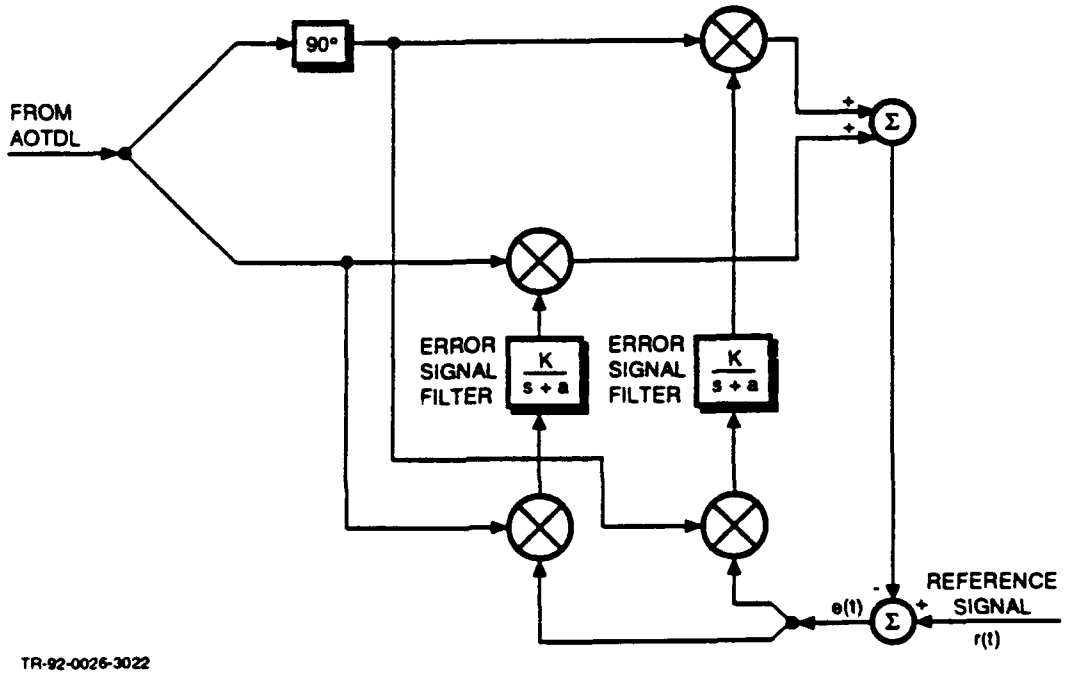

Figure A-1. (U) Canceller Block Diagram

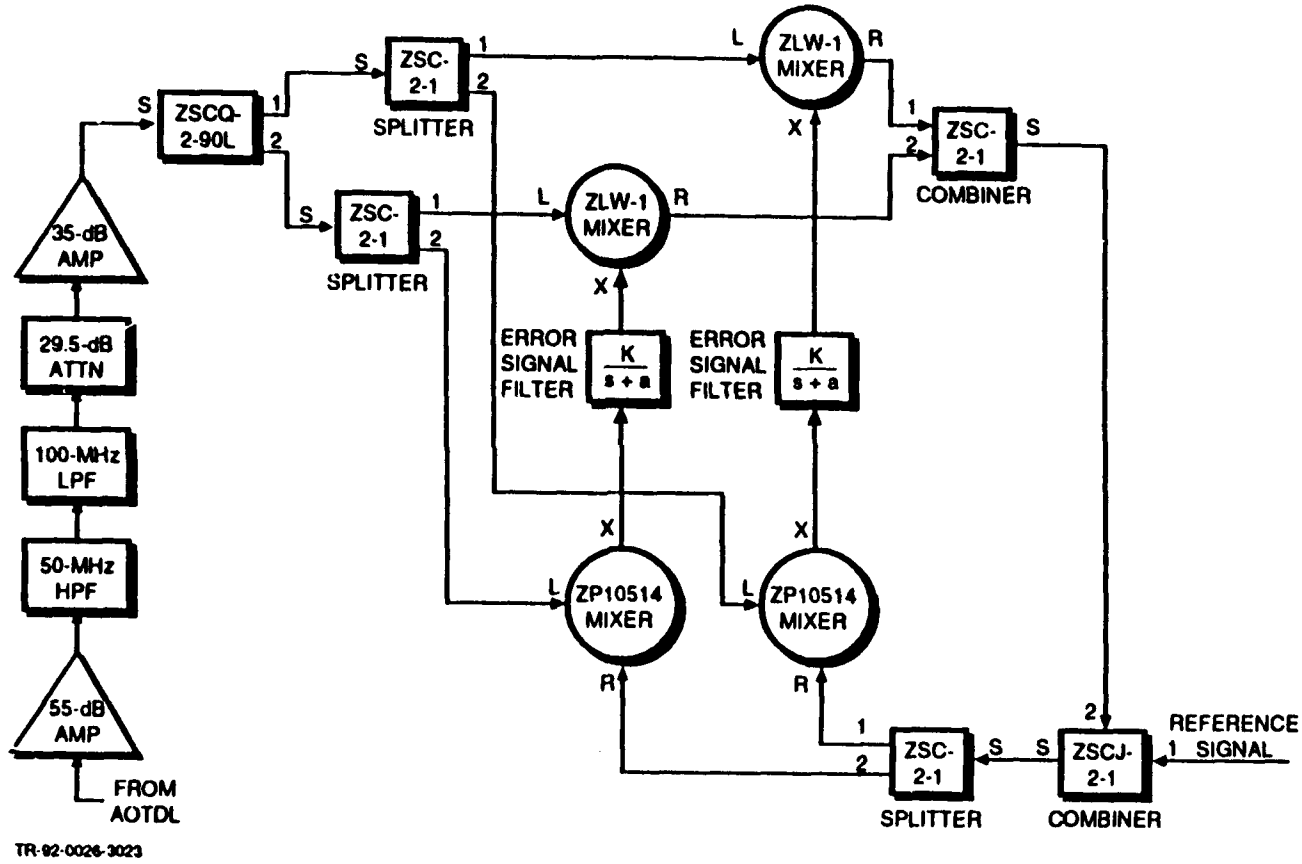

Figure A-2. Circuit Diagram of Canceller

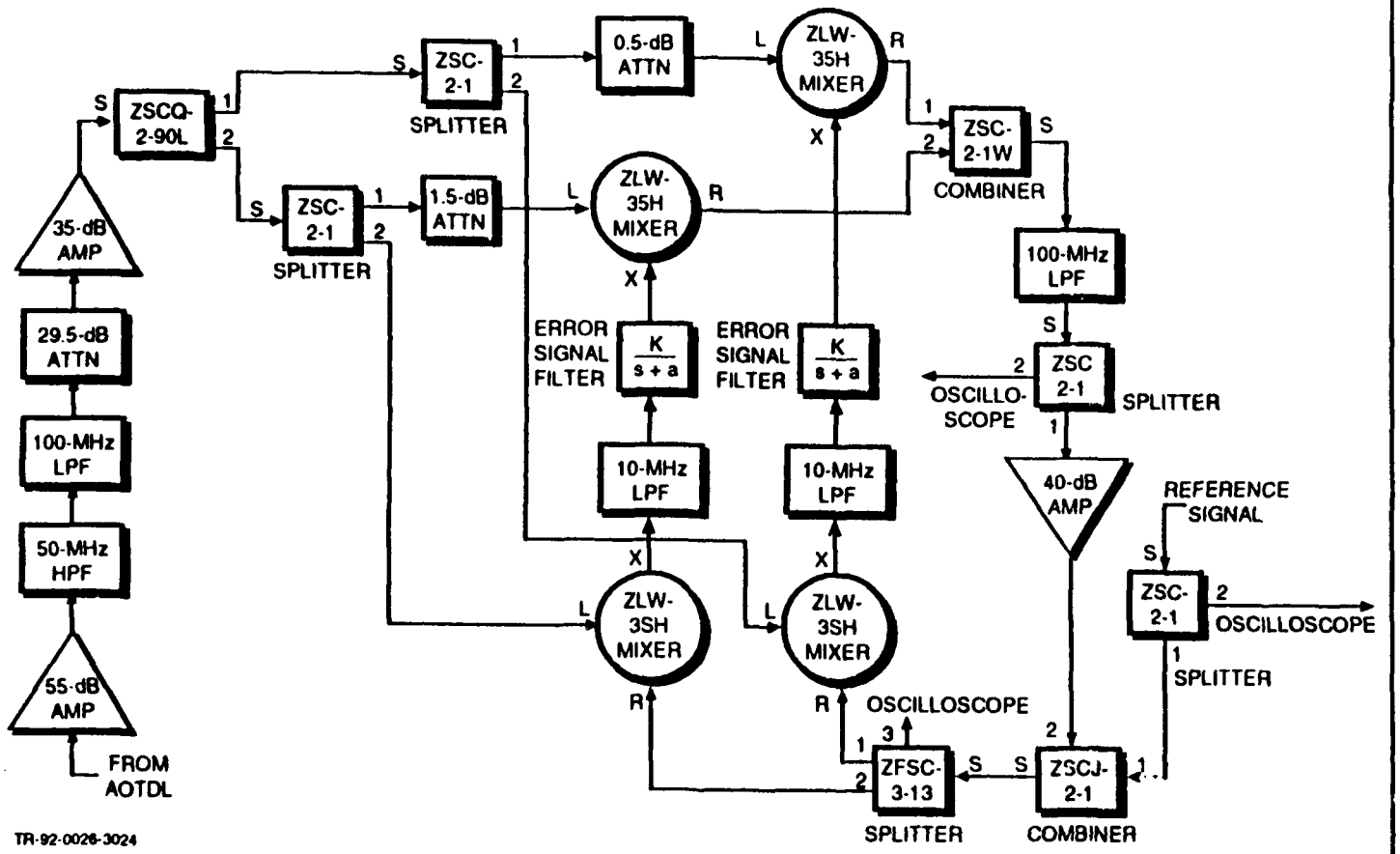

Figure A-3. Circuit Diagram of Canceller as Implemented by Photonics Center Personnel

operates at baseband and does not need to support large bandwidth signals, almost any other operational amplifier would have been suitable.

The first portion of the error signal circuit, the left operational amplifier of ***Figure A-4***, is an LPF with a cutoff frequency of 10 rad/s or 1.6 Hz. Its main components are the 10-kΩ input resistor and a parallel combination of a 1-μF capacitor and a 100-kΩ resistor. The choice of cutoff frequency and selection of components was driven more by availability of components than system requirements.

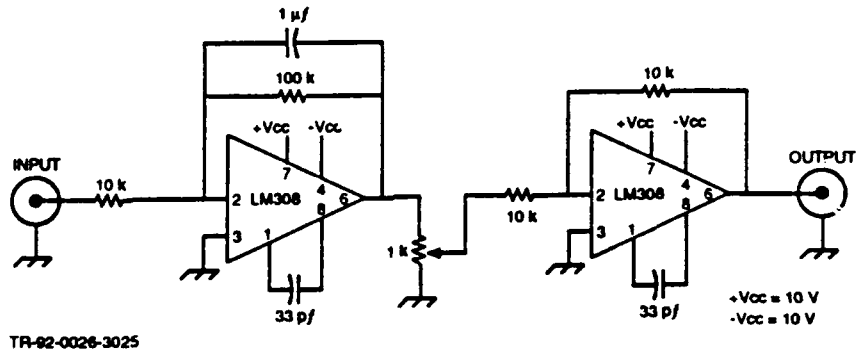

Figure A-4. Error Signal Circuit

Originally, it was intended that the LPF would be an integrator. However, for the prototype, this implementation caused problems because operational amplifier offsets were integrated and caused the integrator to saturate when not connected to the circuit. For the prototype, it was intended that the LPF would be used while the electronic canceller was stabilizing. After the canceller was stabilized, the LPF would then be converted to an integrator by removing the 100-kΩ resistor from the feedback path of the first operational amplifier. This was done the one time that the canceller was made to work. When the LPF was converted to an integrator, the circuit remained stable and the cancellation seemed to improve, as expected.

From a theoretical perspective, the error signal circuit should be an integrator. This configuration forces the error signal (e(t) in ***Figure A-1***) to have a steady state value of zero, which, in turn, will cause the AOTDL phase to exactly match that of the reference, in a steady state. This, in turn, should maximize the jammer cancellation ratio. In practice, the tradeoff between using the LPF and integrator should be performed through laboratory experiments and verified by theoretical analyses. This was not possible under the current ESE effort because of time and funding constraints.

The potentiometer following the LPF is used to adjust the gain of the error signal circuit that will affect the response time of the electronic canceller. The value of 1 kΩ was chosen to minimize the loading on the LPF output and to be less than the input impedance of the buffer amplifier.

The second operational amplifier of ***Figure A-4*** is configured as a sign inverter and buffer. The resistor values were chosen to provide unity gain and not load the 1-kΩ potentiometer.

The 33-pf capacitors on the two operational amplifiers provide frequency compensation. The values used were based on recommendations in the linear circuits handbook containing the specifications on the LM308 operational amplifier.

Each error signal circuit was constructed on a 2-in. by 3-in. protoboard. The protoboards were installed in a chassis, and connections to the other parts of the circuit were effected through the use of BNC connectors. Two ±10-V power supplies were used to supply the 10 V needed by the error signal circuit.

A.2 TUNABLE LPF DESIGN

A critical component of the LMS canceller is the LPF/integrator. This subsection describes the design of a tunable LPF which, although not implemented, may provide useful results. To provide a flat passband with a sharp cutoff, sixth-order Butterworth filter was selected. A passive filter design was excluded from consideration due to the large size of the components needed to produce a low cutoff frequency (f_c). For example, to attain an f_c on the order of 1 kHz, a passive Butterworth filter would require capacitors and inductors on the order of a few microfarads and tens of millihenrys, respectively. For this reason, an active filter was specifically designed as a sixth-order switched capacitor Butterworth LPF. The switched capacitor technique allows a clock tunable f_c that enables fine-tuning of the filter while operating in the LMS canceller. ***Figure A-5*** shows block and pin diagrams of the NSC sixth-order switched capacitor Butterworth LPF chip (part number MF6CN-50) that was used in this design. The f_c of the chip, which can be controlled internally or by an external transistor-transistor logic (TTL) or complementary metal oxide semiconductor (CMOS) logic clock, can range from 0.1 Hz to 20 kHz and is equal to one-fiftieth of the clock frequency. The chip also offers two independent CMOS operational amplifiers (op amps), which were not used in the LPF design.

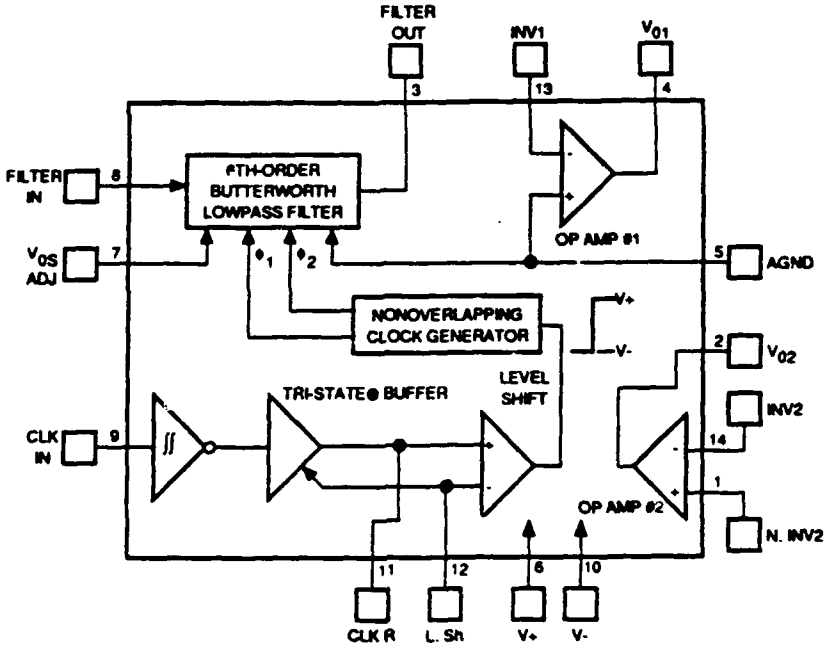

(a) Block Diagram

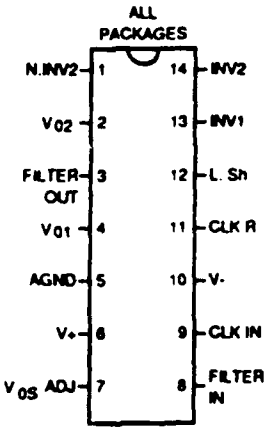

SOURCE: Reference 1

(b) Pin Diagram

TR-92-0026-3016

Figure A-5. MF6CN-50 Diagrams

The filter was designed to accept a TTL clock to control f_c. The voltage range of this clock was ±2.5 to ±7 V and, as stated previously, the clock frequency was 50 times f_c. This clock was input to pin 11 via a BNC cable. A BNC cable was also connected to pin 8 for the LPF input. Pins 6 and 10 were connected to +5- and -5-V power supplies, respectively. These pins were decoupled by connecting a 0.1-μF capacitor between each pin and ground. A common ground (pin 5) was used throughout the design. In addition, pins 7 and 12 were tied to ground to select zero dc offset of the filter output and a TTL clock input, respectively. Pin 3 provided the output of the LPF. Complete descriptions of all 14 pins are given in ***Table A-1***

The LPF output could not drive a 50-Ω load (i.e., a BNC cable), so the signal was buffered by an NSC Fast Buffer Amplifier (part number LH0033G). ***Figure A-6*** shows a connection diagram for this chip. The input to this chip (pin 5) was connected to the output of the LPF. Pins 12 and 10 were connected to +15- and -15-V power supplies, respectively. Also, pin 12 was tied to pin 1 and pin 10 was tied to pin 9 (each through a 100-Ω resistor), and pins 1 and 9 were decoupled by connecting a 0.1-μF capacitor between each pin and ground. In addition, pins 6 and 7 were tied together to disable the offset voltage adjust. A BNC cable provided the output of the buffer amplifier via pin 11. A complete schematic of this LPF design is shown in ***Figure A-7***

Table A-1. Pin Descriptions

Pin	Description
FILTER OUT (3)	The output of the LPF. It will typically sink 0.9 mA and source 3 mA and swing to within 1 V of each supply rail.
FILTER IN (8)	The input to the LPF. To minimize gain errors the source impedance that drives this input should be less than 2k. For single supply operation, the input signal must be biased to mid-supply or ac coupled.
V_{os}ADJ (7)	This pin is used to adjust the dc offset of the filter output; if not used it must be tied to the AGND potential.
AGND (5)	The analog ground pint. This pin sets the dc bias level for the filter section and the noninverting input of opamp #1 and must be tied to the system ground for split supply operation or to mid-supply for single supply operation. When tied to mid-supply, this pin should be well bypassed.
V_{o1} (4), INV1 (13)	V_{o1} is the output and INV1 is the inverting input of opamp #1. The noninverting input of this opamp is internally connected to the AGND pin.
V_{o2} (20), INV2(14), NINV2(1)	V_{o2} is the output, INV2 is the inverting input, and NINV2 is the noninverting input of opamp #2.
V⁺(6), V⁻(10)	The positive and negative supply pins. The total power supply range is 5 to 14 V. Decoupling these pins with 0.1-μF capacitors is highly recommended.
CLK IN (9)	A CMOS Schmitt-trigger input to be used with an external CMOS logic level clock. Also used for self-clocking Schmitt-trigger oscillator.
CLKR (11)	A TTL level clock input when in split supply operation (±2.5 to ±7 V) and L. Sh tied to system ground. This pin becomes a low impedance output when L. Sh is tied to V⁻. Also used in conjunction with the CLK IN pin for a self-clocking Schmitt-trigger oscillator.
L.Sh (12)	Level shift pin, selects the logic threshold levels for the desired clock. When tied to V⁻ it enables an internal tri-state buffer stage between the Schmitt trigger and the internal clock level shift stage thus enabling the CLK IN Schmitt-trigger input and making the CLK R pin a low impedance output. When the voltage level at this input exceeds [25%(V⁺ - V⁻) + V⁻] the internal tri-state buffer is disabled allowing the CLK R pin to become the clock input for the internal clock level shift stage. The CLK R threshold level is now 2 V above the voltage applied to the L Sh pin. Driving the CLK R pin with TTL levels can be accomplished through the use of split supplies and by tying the L Sh pin to system ground.

SOURCE: Reference 1

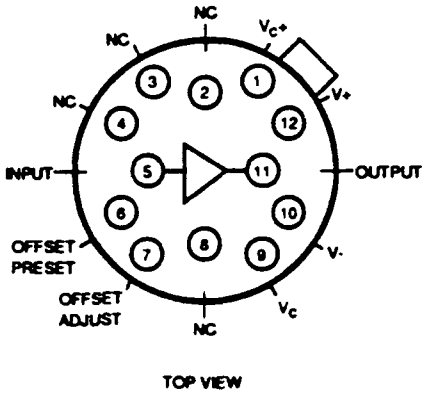

SOURCE: Reference 2

TR-92-0026-3026a

Figure A-6. LH0033G Connection Diagram

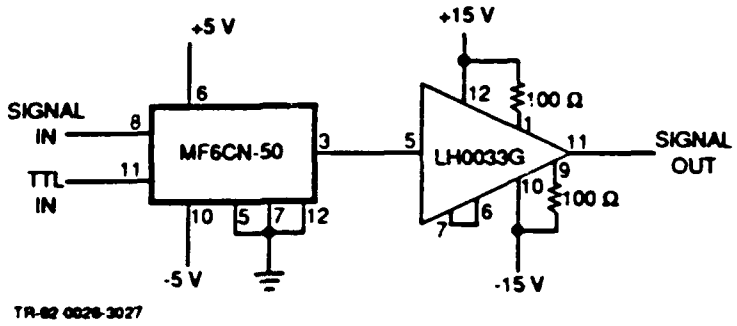

Figure A-7. LPF Design

APPENDIX B. APPLIED OPTICS DRAFT PAPER

Acousto-optic tapped delay line filter

Robert J. Berinato

Dynetics, Inc.

1000 Explorer Blvd.

Huntsville, AL 35806

ABSTRACT

An acousto-optic tapped delay line finite impulse response filter that operates at a system intermediate frequency without requiring a reference optical beam is introduced. Principles of operation are theoretically derived and used to model the system frequency response and multiple tap crosstalk performance. As an element of this derivation, a focused optical illumination of a diverging acoustic wave is analyzed. Experimental results are also provided for a multichannel acousto-optic tapped delay line operational over a 10-MHz bandwidth at an 80-MHz intermediate frequency.

Key Words:

tapped delay line filters, acousto-optics, Bragg cells, delay lines, heterodyne detection, optical processing, signal processing

I. Introduction

Tapped delay line structures are an integral part of many analog and digital signal processing architectures. Convolution with arbitrary filter functions is possible with tapped delay lines by weighting the tapped signals and summing the resultant weighted and delayed signals. Current analog delay lines are either characterized by fixed delay lengths or discrete fixed tap positions. Acousto-optic (AO) analog delay lines can be externally tapped through the use of laser illumination that is spatially modulated by the desired filter weight function, and both continuous and arbitrarily spaced tap positions can be accommodated. AO delay lines are available having bandwidths from 10 MHz to greater than 1 GHz with time-bandwidth products on the order of 500 to 2000.

In this paper, an AO tapped delay line filter is presented together with performance analysis and experimental results. The motivation for this filter development is as a component of an adaptive signal processing system for canceling multipath interfering sources from a desired main-channel signal[1]. The AO tapped delay line filter can be viewed as an AO point modulator that is tapped by a second AO cell that acts as a spatial light modulator (SLM). The resulting diffracted beams from the tapped delay line are heterodyne detected and result in the desired filtered signal and other out-of-band biases. An electronic reference input into the tapped delay line is also considered, and may offer enhanced signal reconstruction efficiency for some applications. An approach to implementing infinite impulse response (IIR) filter functions using two AO tapped delay lines filters is also introduced. Analytical and experimental results are presented that address the filter frequency response for a single tap and two taps, and the more general multiple tap condition is analytically derived.

In Section II we describe the AO tapped delay line filter architecture. As part of this description, an AO SLM concept is presented that allows for tuning of the tap positions and adjustment of the complex weight amplitudes. Section III introduces three architectural variants of

the system, namely an electronic reference implementation, a multichannel AO tapped delay line filter for accommodating multiple input signals, and a conceptual IIR filter approach. Section IV provides an analysis of the tradeoff between AO SLM tap resolution and number of taps, an analysis of the impact of intermodulation products, a summary of the effects of focused tap beams, and a derivation of the theoretical frequency response of the processor. Section V summarizes the experimental work in terms of single-tap frequency response and two-tap frequency response, and conclusions are provided in Section VI.

II. System Layout

Fig. 1 shows a general tapped delay line filter. In this layout, the signal to be filtered is tapped at multiple delays and weighted at each tap to generate a filtered output. Given a signal, $s(t)$, and a weight function, $w(\tau)$, the output from the tapped delay line filter for N taps will be given by

$$y(t) = \sum_{i=1}^{N} w(\tau_i) s(t-\tau_i) \quad . \tag{1}$$

Thus for a single tap at delay τ_k the output is a delayed version of $s(t)$ and is given by

$$y(t) = w(\tau_k) s(t-\tau_k) \tag{2}$$

or equivalently in the frequency domain as

$$Y(f) = w(\tau_k) \int_{-\infty}^{\infty} s(t-\tau_k) exp(-j2\pi ft) dt = w(\tau_k) S(f) exp(-j2\pi f \tau_k) \tag{3}$$

which has a linear phase shift as a function of frequency, f, and delay, τ_k.

The non-recursive structure shown in Fig. 1 implements a finite impulse response (FIR) filter that has a frequency responses composed of only zeros and no poles. The AO implementations presented in this paper utilize an AO cell driven by the signal to be filtered as the delay line element, and a second AO cell to produce the taps. The resultant tapped and weighted

outputs are then collected onto a photodetector. The input to the tapped delay line filter is at an intermediate frequency (IF), and the filtered output is maintained at the system IF. A single tap placed at a given position in the delay line therefore produces a given time-delayed version of the input signal.

A conceptual layout of the AO tapped delay line filter is shown in Fig. 2 for the general case of a multichannel system. An AO SLM is driven with the filter tap information and illuminated with collimated light at the Bragg angle. In the development below, the tap weight is the square of the amplitude of the frequency input to the AO SLM, and is always positive and real. For most filtering applications for which the signal to be filtered is at an IF, this positive and real weight is sufficient. For example, a phase shift of ϕ degrees can be approximated by shifting the tap position by an amount equal to ϕ degrees of the IF carrier. The diffracted light from the AO SLM is transformed to provide the spectrum of the AO SLM across the aperture of the AO tapped delay line device. In order to fully illuminate the AO tapped delay line and thereby achieve the maximum delay line length, the effective focal length of the Fourier transforming optics must be sufficiently large. This illumination of the AO tapped delay line represents the filter weighting function. The diffracted and undiffracted beams from the AO tapped delay line are heterodyne detected resulting in the filtered signal on the output of the processor given by Equation 1.

The AO SLM operation will first be described followed by the development of the AO tapped delay line operation. Several key design considerations will then be presented.

A. AO SLM Description

In our architecture, a tap is generated by injecting a tone into the AO SLM and forming a spot in the frequency plane of the AO tapped delay line. The comparison of the AO SLM approach to other SLM technologies for generating a weight vector for tapped delay line filters has been recently reported on[2]. We write the input to the AO SLM as

$$f(t) = \sum_{i=1}^{N} a_i \cos 2\pi f_{si} t \tag{4}$$

where a_i and f_{si} are the tap amplitude and frequency (subscript s denotes SLM input to distinguish it from the AO tapped delay line input to be described later). We exclude the diffraction efficiency, input optical beam amplitude, and other amplitude factors arising from Fourier transform operations in the following development since they are not critical to an understanding of the system. The signal $f(t)$ drives the AO SLM to form a diffracted +1 order beam given by

$$f(t,x) = w(x) \sum_{i=1}^{N} a_i \exp\left[j2\pi f_{si}\left(t - \frac{T_{slm}}{2} - \frac{x}{v_{slm}}\right)\right] \tag{5}$$

where v_{slm} is the acoustic velocity, T_{slm} is the acoustic time aperture, and $w(x)$ is the apodization function characterizing the AO cell window. The nonuniform frequency response of the AO SLM is included in the coefficients a_i, and can be electronically equalized prior to entering the AO cell. As shown in Fig. 2, lens L1, having an effective focal length F_1, forms the magnified Fourier transform of Equation 5 for illumination of the AO tapped delay line. This Fourier transform illumination can be written as

$$F(t,\tau) = \sum_{i=1}^{N} a_i W\left(\frac{\tau}{\lambda F_1} + \frac{f_{si}}{v_{slm}}\right) \exp\left[j2\pi f_{si}\left(t - \frac{T_{slm}}{2}\right)\right] \tag{6}$$

where τ is the spatial coordinate in the plane of the AO tapped delay line and $W(\tau)$ represents the unscaled transform of the apodization function. For a single tap, this function $W(\tau)$ will be a sharply focused tap beam containing a large spread of input angles.

B. AO Tapped Delay Line Filter Description

The signal to be filtered is input to the AO tapped delay line and can be expressed in terms of a Fourier expansion given by

$$s(t) = \sum_{j=1}^{M} b_j \cos(2\pi f_{tj} t + \phi_j) \tag{7}$$

where b_j and ϕ_j are the amplitudes and phases of each input tapped delay line frequency component f_{tj}. This signal expansion is useful in order to derive the frequency response of the system and to visualize the design factors involved in modifying this frequency response. In analogy to Equation 3, for a single tap the output should be given as

$$y(t) = \sum_{j=1}^{M} b_j \exp(j\phi_j) \exp(-j2\pi f_{tj} \tau_k) \exp(j2\pi f_{tj} t) \tag{8}$$

where τ_k is the tap delay.

Employing the illumination function given in Equation 6, and again selecting the +1 order diffraction, we obtain the diffracted amplitude field

$$s(t,\tau) = \sum_{i=1}^{N} \sum_{j=1}^{M} a_i W_s\left(\frac{\tau}{\lambda F_1} + \frac{f_{si}}{v_{slm}}\right) \exp\left[j2\pi f_{si}\left(t - \frac{T_{slm}}{2}\right)\right]$$

$$\times \quad b_j \exp(j\phi_j) \exp\left[j2\pi f_{tj}\left(t - \frac{T_{dl}}{2} + \frac{\tau}{v_{dl}}\right)\right] \tag{9}$$

where v_{dl} and T_{dl} are the tapped delay line velocity and time aperture. The term $W_s(\tau)$ represents the weighted angular spectrum of the tap energy that is Bragg matched to the acoustic wave for a focused tap input[3]. The constant phase terms dependent on T_{slm} and T_{dl} can be neglected below. Lens L2, having focal length F_2, proceeds to generate the Fourier transform of this amplitude field,

$$s(t,x) = \sum_{i=1}^{N} \sum_{j=1}^{M} a_i b_j \exp(j\phi_j) \exp\left[j2\pi\,(F_j + f_{si})t\right]$$

$$\times \quad \int_{-\infty}^{\infty} W_s\left(\frac{\tau}{\lambda F_1} + \frac{f_{si}}{v_{slm}}\right) \exp\left(j2\pi f_{tj}\tau/v_{dl}\right) \exp\left(j2\pi\,\tau x/\lambda F_2\right) d\tau \tag{10}$$

(the sign of the Fourier exponential is now positive to correspond to the definition of the coordinate

system) to realize the detector illumination

$$s(t,x) = \sum_{i=1}^{N} \sum_{j=1}^{M} a_i b_j \exp(j\phi_j) \exp\left(-j2\pi \frac{\lambda f_{si} f_{tj} F_1}{v_{slm} v_{dl}}\right) \exp\left(-j2\pi \frac{F_1 f_{si} x}{F_2 v_{slm}}\right)$$

$$\times \quad w_s\left(\frac{xF_1}{F_2} + \frac{\lambda f_{tj} F_1}{v_{dl}}\right) \exp\left[j2\pi (f_{tj} + f_{si})t\right] \tag{11}$$

To simplify this notation, we define a position independent phase shift

$$\Delta\Phi_{ij} = -2\pi \frac{\lambda f_{si} f_{tj} F_1}{v_{slm} v_{dl}} \tag{12}$$

which is dependent on both tap frequency and signal frequency. This phase term, which is linear in signal frequency, generates the desired time delay of the reconstructed signal for each tap position (see Equation 3). The signal beam at the detector is thus represented as

$$s(t,x) = \sum_{i=1}^{N} \sum_{j=1}^{M} a_i b_j \exp\left[j\left(\phi_j + \Delta\Phi_{ij}\right)\right] \exp\left(-j2\pi \frac{F_1 f_{si} x}{F_2 v_{slm}}\right)$$

$$\times \quad w_s\left(\frac{xF_1}{F_2} + \frac{\lambda f_{tj} F_1}{v_{dl}}\right) \exp\left[j2\pi (f_{tj} + f_{si})t\right] \quad . \tag{13}$$

The undiffracted beam is also made to illuminate the photodetector, and acts as the reference beam to generate the heterodyned filter output. This undiffracted beam is given by the Fourier transform of the AO tapped delay line illumination, accounting for the amplitude depletion due to the diffracted signal beam[3]. This undiffracted beam is thus represented at the photodetector as

$$u(t,x) = w_u\left(\frac{xF_1}{F_2}\right) \sum_{i=1}^{N} a_i \exp\left(-j2\pi \frac{F_1 f_{si} x}{F_2 v_{slm}}\right) \exp(j2\pi f_{si} t) \tag{14}$$

where $w_u(x)$ denotes the image of the AO SLM aperture with a weighting due to diffraction depletion. We note that this beam is similar to the diffracted signal beam except that they:

1. Differ in position by an amount $\lambda f_{tj} F_2 / v_{dl}$;

2. Differ spatially due to the diffracted beam shape and undiffracted beam depletion region;
3. Differ in temporal modulation by the AO SLM input signal; and
4. Have a tap frequency and signal frequency dependent phase shift of the temporal modulation resulting in time delay.

C. The Detected Output Signal

The heterodyned filter output is the magnitude squared sum of the diffracted and undiffracted beams given by

$$d(t) = \int_{-L/2}^{L/2} \left[|s(t,x)|^2 + |u(t,x)|^2 + 2\mathrm{Re}\{s(t,x)u^*(t,x)\} \right] dx \tag{15}$$

where L is the detector size. The third component of this detected signal is the desired output and is separated in frequency from the first two baseband components. Using the results of Equations 13 and 14, and ignoring the baseband components, this desired output is expressed as

$$d(t) = \int_{-L/2}^{L/2} \mathrm{Re}\{ \sum_{i=1}^{N} \sum_{j=1}^{M} a_i b_j \exp\left[j(\phi_j + \Delta\Phi_{ij})\right] \exp\left(-j2\pi \frac{F_1 f_{si} x}{F_2 v_{slm}}\right) w_s\left(\frac{xF_1}{F_2} + \frac{\lambda f_{ij} F_1}{v_{dl}}\right)$$

$$\times \quad \exp\left[j2\pi (f_{ij} + f_{si})t\right] w_u\left(\frac{xF_1}{F_2}\right) \sum_{k=1}^{N} a_k \exp\left(j2\pi \frac{F_1 f_{sk} x}{F_2 v_{slm}}\right) \exp(-j2\pi f_{sk} t) \}dx \quad . \tag{16}$$

There are two cases arising in Equation 16 depending on whether $i=k$ or $i \neq k$. For $i=k$, we have our desired result

$$d(t,i=k) = \mathrm{Re}\{ \sum_{i=1}^{N} a_i^2 \sum_{j=1}^{M} b_j \exp\left[j(\phi_j + \Delta\Phi_{ij})\right] \exp(j2\pi f_{ij} t)$$

$$\times \quad \int_{-L/2}^{L/2} w_s\left(\frac{xF_1}{F_2} + \frac{\lambda f_{ij} F_1}{v_{dl}}\right) w_u\left(\frac{xF_1}{F_2}\right) dx \} \quad . \tag{17}$$

For the case of $i \neq k$, we find that cross terms result given by

$$d(t, i \neq k) = \mathrm{Re}\Big(\sum_{i=1}^{N} \sum_{j=i}^{N} \sum_{k=1}^{N} a_i a_k b_j \exp\big[j(\phi_j + \Delta\Phi_{ij})\big] \exp\big[j2\pi\,(f_{ij} + f_{si} - f_{sk})t\big]$$

$$\times \int_{-L/2}^{L/2} w_s\Big(\frac{xF_1}{F_2} + \frac{\lambda f_{ij} F_1}{v_{dl}}\Big) w_u\Big(\frac{xF_1}{F_2}\Big) \exp\Big(-j2\pi \frac{F_1(f_{si} - f_{sk})x}{F_2 v_{slm}}\Big) dx \Big) \qquad (18)$$

which appear within the band of the desired output at the output of the photodetector.

It is helpful at this point to examine Equations 17 and 18 in terms of the AO tapped delay line properties. First, the ith tap in Equation 17, having the weight a_i^2, creates a delayed signal at the IF given by Equation 8 and weighted by the overlap integral. For multiple taps, the output is composed of multiple delayed and weighted replicas of the input signal, each weighted by the overlap integral. We also observe that the overlap integral is a function of AO tapped delay line input frequency, f_{ij}, and as a result contributes to the frequency response of the system. Finally, Equation 18 represents the cross terms that result from closely spaced taps, each of which is offset from the IF by the tap difference frequency input to the AO SLM. The overlap integral is now seen to be a Fourier transform of the product of the two weighted apodization functions, and provides a measure of the degree of crosstalk for a given tap separation, $f_{si} - f_{sk}$, and AO tapped delay line input frequency, f_{ij}.

D. Design Considerations

The selection of AO devices and lenses is critical to the performance of the AO tapped delay line filter. In this subsection, criteria for selection of key components will be provided and representative examples will be given. The performance of the system as a function of the design parameters will be described in more detail and simulated in Section IV.

The selection of the lens L1 will first be considered. This lens must form the Fourier

transform of the AO SLM at the plane of the AO tapped delay line. This selection is primarily driven by the total tapped delay line filter length, T_{dl}. As given in Equation 6, the position of the spots in the plane of the AO tapped delay line are (recall that τ is a distance coordinate in the tapped delay line plane)

$$\tau = \frac{\lambda f_{si} F_1}{v_{slm}} \quad . \tag{19}$$

In order to span the total tapped delay line filter length for a bandwidth of inputs to the AO SLM, B_{slm}, the effective focal length must satisfy

$$F_1 = \frac{T_{dl} v_{dl} v_{slm}}{\lambda B_{slm}} \quad . \tag{20}$$

In addition, the heterodyne output efficiency is dependent on the overlap integral given in Equation 18. We thus desire to have the center of the diffracted spot, $w_s(x)$, lying within the undiffracted spot, $w_u(x)$. This sets a minimum requirement that one-half the width of $w(x)$, i.e., $v_{slm}T_{slm}/2$ at the AO SLM, be equal to the offset of the diffracted spot. Thus

$$\frac{\lambda f_{ij} F_2}{v_{dl}} = \frac{v_{slm} T_{slm} F_2}{2F_1} \quad . \tag{21}$$

Combining Equations 20 and 21 we find that a fundamental requirement on the AO SLM is that the time-bandwidth product satisfy

$$B_{slm} T_{slm} = 2 f_{ij} T_{dl} \quad . \tag{22}$$

It is also possible to impose an angular offset of the input tap beams so that the Bragg angle occurs on the edge of the angular input spectrum. This results in an undiffracted beam that is depleted from one side of the beam (rather than the center of the beam as assumed in the above equations), and therefore allows the diffracted beam to be offset from the undiffracted beam depleted area by an amount approaching the full width of $w_u(x)$. This approach can offer a wider frequency response and is described in more detail in Section IV.

An additional design consideration arises from the desire to minimize the effect of the cross-terms given in Equation 18. The overlap integral is seen to be a Fourier transform in this case. We assume for now (more exact derivations will be provided in Section IV) that the illumination due to the beam overlap is uniform and overfills the photodetector, and write the overlap integral as[4]

$$P(f_{si} - f_{sk}) = \int_{-\infty}^{\infty} \mathrm{rect}(x/L)\exp\left[-j2\pi \frac{F_1(f_{si} - f_{sk})x}{F_2 v_{slm}}\right]dx \quad . \tag{23}$$

We therefore find that the overlap integral defining the heterodyne efficiency of the undesired cross-terms reduces to

$$P(f_{si} - f_{sk}) = L\,\mathrm{sinc}\left[L\,\frac{F_1(f_{si} - f_{sk})}{F_2 v_{slm}}\right] \tag{24}$$

where $\mathrm{sinc}(\beta) = \sin\pi\beta/\pi\beta$. Thus the minimum AO SLM input frequency separation can be set such that we achieve the first null of the sinc function (β=1). We therefore find that the minimum AO SLM input frequency separation is given by

$$f_{si} - f_{sk} = \frac{\pi F_2 v_{slm}}{L F_1} \quad . \tag{25}$$

It is observed that to maximize the tap resolution the detector size must be as large as possible, preferably matching the overlap region dimensions. For sharply focused tap beams the detector size should be on the order of the diffracted beam size for a wideband signal input, which will be smaller than the undiffracted beam size as detailed in Section IV.

III. AO Tapped Delay Line Design Variants

Several variants are possible based on the design presented in Section II. These include the addition of an electronic reference tone at the input to the AO tapped delay line to potentially improve heterodyne efficiency, the extension of the architecture to multichannel operation, and the

use of two AO tapped delay lines and feedback to generate arbitrary IIR filter responses. Each of these design variants will now be described.

A. Electronic Reference Option

One technique available for potentially improving the efficiency of the filtering process is to employ an out-of-band electronic reference. This electronic reference plays the role of the undiffracted beam in the above development, but generates a beam at the photodetector that may have greater overlap with the diffracted signal beam. The output generated by the heterodyne detection of the electronic reference and signal beams will now appear, not at the system IF, but rather at the difference between the system IF and the frequency of the electronic reference. This result is mixed with the electronic reference tone to bring the desired filtered signal back up to the system IF.

We let the electronic reference input to the AO tapped delay line be given as

$$r(t) = \alpha\cos(2\pi f_{er}t) \tag{26}$$

which results in the diffracted electronic reference beam at the detector

$$r(t,x) = \alpha w_{er}\left(\frac{xF_1}{F_2} + \frac{\lambda f_{er}F_1}{v_{dl}}\right)\sum_{i=1}^{N} a_i\exp(j\Delta\Phi_{ier})\exp\left(-j2\pi\frac{F_1 f_{si}x}{F_2 v_{slm}}\right)\exp\left[j2\pi\,(f_{er} + f_{si})t\right] \tag{27}$$

where $\Delta\Phi_{ier}$ is given by Equation 12 with f_{ij} replaced by f_{er}. Adding this illumination to the previous detector illumination, we have the resulting output detected signal given by

$$d'(t) = d(t) + \int_{-L/2}^{L/2}\left[\,|r(t,x)|^2 + 2\mathrm{Re}\{r(t,x)u^*(t,x)\} + 2\mathrm{Re}\{s(t,x)r^*(t,x)\}\right]dx \tag{28}$$

where $d(t)$ is given in Equation 15. The final term is the term of interest with all other terms being out-of-band with this term. We write this desired term, $d_{er}(t)$, as

$$d_{er}(t,i=k) = \mathrm{Re}\{\sum_{i=1}^{N} a_i^2 \sum_{j=1}^{M} b_j \exp\left[j\left(\phi_j + \Delta\Phi_{ij} - \Delta\Phi_{ier}\right)\right]\exp\left[j2\pi(f_{ij} - f_{er})t\right]$$

$$\times \int_{-L/2}^{L/2} w_s\left(\frac{xF_1}{F_2} + \frac{\lambda f_{ij} F_1}{v_{dl}}\right) w_{er}\left(\frac{xF_1}{F_2} + \frac{\lambda f_{er} F_1}{v_{dl}}\right) dx \} \quad . \tag{29}$$

Cross-terms similar to Equation 18 will also result for this architecture.

The impact of employing the electronic reference approach is a greater spatial overlap of the two heterodyned beams, as given by the integral in Equation 29. The key drawback of this approach is the loss of the true time delay properties of the delay line. This is a result of the phase term, $\Delta\Phi_{ij} - \Delta\Phi_{ier}$, which is proportional to tap position and the difference frequency, $f_{ij} - f_{er}$. Thus, the phase term is not proportional to the signal frequency but rather to the difference frequency, resulting in a proportional phase shift of the signal carrier frequency within the signal envelope. This limits the electronic reference approach to incoherent applications not requiring true time delay of the signal, but rather just true time delay of the envelope magnitude.

This non-true time delay property of the electronic reference approach also occurs for time delay architectures that employ a reference beam (not coincident with the undiffracted beam) to interfere with the diffracted beam. This is not an obvious result but follows rather from the mathematics provided above, and has not been recognized in earlier writings[5]. If the reference beam is given a phase delay through addition of path length (for example with a piston-action mirror), true time delay can be achieved as has been demonstrated for a beamforming application[6].

B. Multichannel System Architecture

For a number of signal processing applications, multidimensional filtering is desired. For these cases, multiple signals are simultaneously filtered and the resultant system output is the sum of the individually filtered input signals. Each input signal passes through its filter with a given impulse response.

This multidimensional filtering can be achieved in a compact architecture by capitalizing on the three-dimensional nature of optics. Multichannel AO cells replace the single-channel AO SLM and the AO tapped delay line to allow simultaneous input of multiple filter functions and multiple signals to be filtered. All of the resultant diffracted and undiffracted light from the multichannel AO tapped delay line is transformed (focused) onto the photodetector resulting in the desired multidimensional filter output. Such a filter is shown in Fig. 2.

The required optical system for the multichannel architecture has several demanding aspects. The input to the AO SLM is now composed of plane wave illuminations for each of the N channels. In order to optimize the amount of light being diffracted, it is desirable to employ a beamforming system that forms N collimated sheet beams that match the AO aperture function. This can be achieved through a beamsplitting configuration, or through the use of holographic gratings. At the output of the AO SLM, anamorphic optics must be used to 1) image the AO SLM acoustic columns onto the AO tapped delay line acoustic columns in the direction orthogonal to the acoustic propagation direction, and 2) form a magnified Fourier transform of each AO SLM diffracted beam to generate each of the N tap weight functions. An anamorphic system of lenses takes a magnified Fourier transform of the AO SLM along the acoustic propagation direction, and images along the orthogonal direction. The resultant output from the AO tapped delay line is transformed onto the photodetector with a final spherical lens, thereby capturing all delays and all channels on a single photodetector.

C. IIR Filter Architecture

A general IIR filter function will be composed of both zeros and poles, and must be implemented with both feedforward and feedback tap weights. The AO tapped delay line filters described above have implemented only the feedforward portion of an arbitrary IIR filter, and can be characterized as FIR filters. It is possible to approximate a stable IIR filter with a very long FIR filter because the impulse responses can be matched for a length of time after which the IIR filter response is negligible. For a number of applications this requires prohibitively long FIR filters that in turn

require a high degree of computational and hardware complexity to implement. A better solution is often to implement a lower complexity IIR filter, although this must be done carefully to avoid instability due to the feedback structure. One application which has realized great utility from the IIR filtering is adaptive equalization[7].

An approach to implementing the IIR filter with two tapped delay line filters is shown in Fig. 3. For an input, $u(t)$, this general IIR filter has an output, $y(t)$, given by

$$y(t) = \sum_{i=0}^{M} a_i u(t - i\tau) - \sum_{j=1}^{N} b_j y(t - j\tau) \tag{30}$$

where τ is a unit time delay. The corresponding transfer function is then

$$H(z) = \frac{Y(z)}{U(z)} = \frac{\sum_{i=0}^{M} a_i z^{-i}}{1 + \sum_{j=1}^{N} b_j z^{-j}} \quad . \tag{31}$$

The IIR AO tapped delay line filter is composed of two replicas of the AO tapped delay line filter, as shown in Fig. 4. Here the feedforward path is identical to the standard FIR filter described earlier in Section II, with input $u(t)$ and weighting function described by the vector a in Equation 30. The output of the feedforward path then drives a second AO delay line, which is in turn tapped by the weighting function denoted by the vector b in Equation 30.

IV. Analysis of Filter Performance

The frequency response of the AO tapped delay line filter is dependent on a number of design considerations. Each of these is described below, and techniques for optimizing the design to meet specific requirements are presented. In addition, the crosstalk of the system is considered as a function of the apodization of the AO SLM and properties of the tap beam.

A. Analysis of AO Tapped Delay Line Focused Input and Frequency Response

The focused spot that illuminates the AO tapped delay line, given in Equation 6, approximates the beam waist of a Gaussian beam. This focused beam has a large spread in angle and will vary in degree of Bragg matching with the acoustic wave. Therefore, the diffracted beam will be generated by a central cone of angles that significantly match the Bragg conditions, resulting in a nonuniform depletion of the undiffracted beam. The combination of these two effects create the functions w_s and w_u given in Equations 11 and 14, respectively. For successful operation of the system, the diffracted and undiffracted beams must also overlap. The degree of focus of the input optical beam will thus affect the heterodyne efficiency and resultant frequency response of the AO tapped delay line system.

AO diffraction from Gaussian illumination beams has been investigated by others[3]. Following Korpel, we define an input optical plane wave spectrum and acoustic plane wave spectrum as $E_i(\theta)$ and $S(\gamma)$, respectively, where the angles θ and γ are defined using the sign convention of Fig. 5. The resulting diffracted beam for +1 diffraction, $E_1(\theta)$, is then given as

$$E_1(\theta) = -0.25jkCS(\theta_B - \theta)E_i(\theta - 2\theta_B) \tag{32}$$

where k is the optical wavevector in the crystal, C is a proportionality constant relating $S(\gamma)$ to the change in index of refraction of the material, and θ_B is the Bragg angle. The interaction of the focused optical beam with the spreading acoustic wave is shown schematically in the wavevector diagram of Fig. 6a and the physical model of the crystal in Fig. 6b.

It can be observed that when the angular spread of the focused optical beam is greater than the acoustic angular spread, then the diffracted beam has an angular plane wave spectrum that approximates that of the acoustic beam. The undiffracted beam will be depleted accordingly. For multiple input frequencies, multiple images of the acoustic angular spread will be formed. Therefore, we observe that W_s appearing in Equation 10 can be replaced by S. This will be then be converted to a spatial pattern $w_s(x)$ after the final lens L2, as given in Equations 13 and 17. Likewise, $w_u(x)$ in Equations 14 and 17 can be written as the difference between $w(x)$ and $w_s(x)$.

We now assume that $S(\gamma)$ can be modeled as a sinc function[3],

$$S(\gamma) \propto \mathrm{sinc}(\gamma L_a / \Lambda) \tag{33}$$

where L_a is the acoustic column width and Λ is the acoustic wavelength. We also assume that $E_i(\theta)$ is uniform over all angles contained in $S(\gamma)$ (i.e., $E_i(\theta)$ has a large cone angle of equal angular plane wave amplitude). The frequency response for a given frequency input to the AO tapped delay line can then be calculated. This model is shown in Figure 7. We now observe that the conditions for overlap in Figs. 7c and 7e relate back to Equation 21. The performance of the system can also be improved if we note that the input of $E_i(\theta)$ need not be centered at θ_B but could be centered at $-\Delta\theta + \Lambda/L_a$ so that greater AO tapped delay line frequencies can be handled with more uniform frequency response, as in Fig. 7d.

For the hardware implementation and experimental results described below in Section V, the focused input optical beam leads to a condition as shown in Fig. 7e. For this case, the acoustic angular spread is approximately equal to the optical angular spread, and both of the angular spreads are great enough to obtain significant overlap of the diffracted and undiffracted beams in the plane of the photodetector. We now observe that as an input tone to the AO tapped delay line, f_{ij}, is tuned, the system frequency response given by the overlap integral in Equation 17 will vary and thereby produce a non-uniform frequency response. We can express the heterodyne efficiency, η_{het}, as the overlap integral

$$\eta_{het} = \int_{-D+\lambda f_{ij} F2/v_{dl}}^{D} w_s\left(\frac{xF_1}{F_2} + \frac{\lambda f_{ij} F_1}{v_{dl}}\right)\left(1 - w_s\left(\frac{xF_1}{F_2}\right)\right) dx \tag{34}$$

where $2D$ is the size of the undiffracted beam at the photodetector (a magnified image of the AO SLM) and D is given as

$$D = \frac{T_{slm} v_{slm} F_2}{2F_1} \quad . \tag{35}$$

Using the sinc(x) model described above, we have the processor heterodyne efficiency frequency response

$$\eta_{het}(f_{ij}) = \int_{-D+\lambda f_{ij}F_2/v_{dl}}^{D} w_s\left(\frac{xF_1}{F_2} + \frac{\lambda f_{ij}F_1}{v_{dl}}\right)\left(1 - \mathrm{sinc}\left(\frac{xF_1}{F_2}\right)\right)dx \quad . \tag{36}$$

This function can be interpreted as the correlation of the diffracted beam with the undiffracted beam in the variable f_{ij}. Fig. 8 displays the results of a computer simulation of this frequency response for a given system configuration. Fig. 8a displays the apodization of the AO SLM, which is assumed to be Gaussian with standard deviation, *std*, and symmetric with respect to the AO SLM acoustic aperture. The diffracted beam (shown for $f_{ij} = 0$) is displayed in Fig. 8b for three different tap beam focusing conditions. The width of the diffracted beam zeros is constant, but is shown with respect to the width of the undiffracted beam (assumed to be changing due to greater focus of the tap), and therefore appears to be changing in width. The diffracted beam is also shifted with respect to the center of the undiffracted beam to show the effects of different portions of the angular spread of the input tap being Bragg matched. Fig. 8c shows the resulting depleted undiffracted beam, and Fig. 8d provides the system frequency response as given by Equation 36. Figure 9 shows another condition consisting of a sharper Gaussian apodization of the AO SLM and a more symmetric focused tap beam with respect to the Bragg matching condition. In this case, due to the greater symmetry of the focused tap beam with respect to the Bragg matching condition, the normalized frequency response cuts off at a lower frequency for each focusing condition.

B. System Resolution and Crosstalk

As in any AO Fourier transform system, the ability to generate resolvable spots in the frequency plane is limited by the size and apodization of the input aperture. A traditional estimate of the total number of resolvable spots in an AO spectrum analyzer is the AO time-bandwidth product, which can be derived assuming a uniform apodization at the input aperture. With this criteria, the

crosstalk between adjacent frequency components is quite severe. The use of non-uniform apodization can reduce the crosstalk of adjacent frequency components at the expense of reduced number of resolvable spots. In order to completely eliminate crosstalk, the Fourier transform of the input apodization function must be finite width (compact). One example of such apodization is a sinc function whose Fourier transform is a rect. Unfortunately, in order to achieve this total elimination of crosstalk, the input aperture must be infinite in extent. Therefore, a balance between number of resolvable spots and the crosstalk generated between closely spaced taps must be designed. An attractive apodization function that has been well analyzed[4,8] is a Gaussian weighting, which naturally results due to the Gaussian beam properties of the laser illumination.

In order to model the resolution and crosstalk, we refer back to Equation 18 and calculate the overlap integral. We choose to model the crosstalk in a consistent manner to the modeling of the frequency response above, and therefore apply a Gaussian apodization with a sinc(x) acoustic beam shape. We note that the resulting crosstalk will be a function of tap frequency separation and the input frequency to the AO tapped delay line. Fig. 10 shows the resulting crosstalk for the conditions of Fig. 8. We note that the crosstalk follows approximately a sinc(x) as a function of tap frequency separation, as described in Equation 24.

C. AO Spatial Light Modulator Intermodulation Products

AO SLM crosstalk will also result due to the generation of intermodulation products that appear as spurious taps at the AO tapped delay line. The magnitude of these intermodulation products can be kept below a specified level to set the spur-free dynamic range of the system. For two equal amplitude taps, resulting in tap intensities $I_1 = I_2 = I$, the intensity of the intermodulation product spur, I_s, relative to the desired intensity, I, is given as[4]

$$I_s / I = \eta_f^2 / 36 \tag{37}$$

where η_f is the diffraction efficiency. Solving this for η_f, we have

$$\eta_f = 6\sqrt{I_s / I} \quad . \tag{38}$$

Therefore, to achieve 40-dB suppression of the intermodulation products ($I_s/I = 0.0001$), η_f must be set to 0.06, or 6% diffraction efficiency. This will limit the total amount of light available in each of the taps. For three or more taps, third-order intermodulation products will appear in band and will result in a more severe diffraction efficiency requirement by a factor of 2.

V. Experimental Results

A multichannel AO tapped delay line filter was fabricated and tested to verify the theory presented above. Both the baseline architecture and the electronic reference approach were implemented and shown to agree with theory. All experimental results presented below are for single-channel operation. Requirements for the fabricated system included an 80-MHz IF with a 10-MHz bandwidth and a delay line length of 1-μsec. The laser for the system was a 20-mW diode-pumped Nd:YAG laser operating at a wavelength of 532 nm. The system employed a Brimrose 8-channel AO cell as the AO SLM and a second Brimrose 8-channel AO cell as the AO tapped delay line. Both of the AO cells had passbands from 60 MHz to 100 MHz. A ThorLabs photodetector having a frequency response beyond 100 MHz was used.

A. Single-Tap Frequency Response

When single taps are applied to the AO tapped delay line filter, the input signal should be accurately reconstructed with a given time delay depending on tap position. In order to accurately reconstruct the signal, a very flat magnitude frequency response and linear phase response are required. A number of measurements were taken to assess the effects of varying the tap position on the single-tap frequency response. The best such frequency response plot obtained experimentally is shown in Fig. 11. For this measurement, the frequency input to the AO SLM was 76.0 MHz, and averaging over 16 network analyzer sweeps was employed to reduce the effects of amplitude variation due to system vibrations. We see in Fig. 11(a) that across the passband the magnitude

response is within a 0.2-dB range. Also shown in Fig. 11(b) is the phase response (with the time delay removed in the network analyzer) which is flat to within 3 deg across the passband. The insertion loss for this example was 8 dB with a 55-dB low-noise amplifier after the photodetector, yielding a total insertion loss of 63 dB.

The frequency response remained within a 3-dB range across the passband for varying tap positions, although the insertion loss varied over approximately 10 dB when tuning the AO SLM input over its 40 MHz bandwidth. This behavior is shown in Fig. 12 for five values of the tap position spanning the desired 40-MHz frequency spread. The variation in the insertion loss of the system as a function of tap position can be equalized by controlling the power input to the AO SLM as a function of frequency. This is equivalent to imposing an additional tap-dependent weighting on the weight function applied to the system.

B. Two-Tap Frequency Response

For two equal-amplitude taps, the frequency response consists of notches located at frequencies given by $(2k+1)/2\tau$ for $k=0,1,2,...$ Two equal amplitude taps were generated in the AO tapped delay line filter by applying to the AO SLM a waveform consisting of a tone modulated onto an 81.6-MHz carrier using a double-sideband, suppressed-carrier (DSB-SC) mixer. The carrier suppression was approximately 27 dB relative to the sidebands, and the tap spacing was set by tuning the frequency of the tone input to the DSB-SC mixer.

Fig. 13 depicts the theoretical frequency response for delays of (a) 22 nsec, 88 nsec, and 176 nsec, and (b) 352 nsec and 572 nsec. Fig. 14 shows the experimental results for two taps with tap frequency separations of (a) 1 MHz, 4 MHz, and 8 MHz, and (b) 16 MHz and 26 MHz. The experimental results demonstrate good agreement with the theory. Using the simulated results, we can refer back to Equation 19 to verify the quantity F_l (note that τ is a distance). For a 26 MHz frequency spread resulting in a delay of 572 nsec, and with an acoustic velocity of 4200 m/sec, we have F_l = 0.73 m. The actual focal length of the lens employed was 0.75 m, and the

variance from the calculated value of 0.73 m is most likely due to a positioning of the lens L1 slightly closer than one focal length from the AO SLM.

VI. Conclusions

An AO implementation of a tapped delay line filter has been described. The operating principles have been mathematically derived, design considerations have been reviewed, and performance has been modeled and experimentally verified. Architectural variants have also been proposed, including an electronic reference option, a multichannel implementation, and the combination of two AO tapped delay lines with feedback to perform general IIR filtering.

A number of practical issues remain to be resolved, primarily in the realization of a uniform frequency response not only for a single tap but for multiple tap positions over the multiple channels of the multichannel system. This requires careful component design and selection, critical system alignment, and the development of repeatable alignment procedures.

The driving application for this AO tapped delay line is to multichannel adaptive cancellation of wideband interference sources for an active radar scenario[1]. In this overall system, a multichannel time-integrating correlator provides the adaptive weight vector information and the AO tapped delay lines perform the filtering to generate the desired signal estimate. At the Rome Laboratory Photonics Center, a multichannel acousto-optic time-integrating correlator in a Mach-Zehnder configuration has been fabricated and tested in a two-channel configuration. The AO tapped delay line filter described in this paper has also been fabricated at the Rome Laboratory Photonics Center with support from Rome Laboratory in-house project funds. Prior Rome Laboratory work on this AO tapped delay line architecture is summarized in Reference 2.

The author would like to acknowledge the contributions of Captain Michael Ward of the Rome Laboratory Photonics Center and Dr. Chris Anderson and Michael Zari of Dynetics, Inc., for their technical suggestions and their review of the manuscript. This research has been supported in part by the US Air Force Rome Laboratory Photonics Center under contracts F30602-91-D-0001

(Subcontract C-140545) and F30602-92-C-0026.

References

1. M. C. Zari, R. J. Berinato, M. J. Ward, and H. G. Andrews, "Multichannel Optical Time-Integrating Correlator for Adaptive Jamming Cancellation," SPIE Vol. 1704, paper 1704-11 (1992)
2. M. J. Ward, C. W. Keefer, S. T. Welstead, "Spatial Light Modulation Techniques for System Application to Multipath Delay Estimation," Applied Optics, 31, 4010-4015 (1992).
3. A. Korpel, *Acousto-Optics* (Marcel Dekker, New York, 1988).
4. A. VanderLugt, *Optical Signal Processing* (John Wiley and Sons, New York, 1992).
5. F. W. Freyre, "Continuously Variable Delay Line," U.S. Patent 4,390,247, (1983).
6. H. Zmuda, E. N. Toughlian, "Adaptive Microwave Signal Processing: A Photonic Solution," Microwave Journal, 35, pp. 58-71 (1992).
7. S. Qureshi, "Adaptive Equalization," Proc. IEEE, 73, 1349-1387 (1985).
8. D. A. Satorius, T. E. Dimmick, "Impact of Beam Weighting on Dynamic Range and Resolution of Optical Spectrum Analyzers," SPIE Vol. 1704, paper 1704-09 (1992).

FIGURE CAPTIONS

Fig. 1. Finite impulse response tapped delay line filter.

Fig. 2. Two-channel AO tapped delay line architecture: (a) top view; (b) side view showing multichannel operation.

Fig. 3. Infinite impulse response tapped delay line filter.

Fig. 4. AO implementation of IIR filter.

Fig. 5. Wavevector sign convention.

Fig. 6. Wavevectors for a focused optical input: (a) wavevector diagram for a focused optical tap; (b) physical model of the AO cell.

Fig. 7. Diffracted and undiffracted beam phenomenology: (a) acoustic beam shape; (b) focused optical tap beam shape; (c) diffraction for a tap beam centered at the Bragg angle; (d) diffraction for a tap beam not centered at the Bragg angle; (e) diffraction for a weakly focused beam.

Fig. 8. Simulated diffracted and undiffracted beams and resulting system frequency response, ———— zeros of sinc(x) at $-3D/5\pm(2i-1)2D$, • • • • • zeros of sinc(x) at $-3D/5\pm(2i-1)2D/5$, - - - - - - zeros of sinc(x) at $-3D/5\pm(2i-1)2D/25$: (a) Gaussian beam apodization, $std=2D$; (b) diffracted beam for three focus conditions; (c) depleted undiffracted beam; (d) normalized system frequency response, $f_{ij}(2D)=v_{slm}T_{slm}v_{dl}/\lambda F_1$.

Fig. 9. Simulated diffracted and undiffracted beams and resulting system frequency response, ———— zeros of sinc(x) at $-3D/5\pm(2i-1)2D$, • • • • • zeros of sinc(x) at $-3D/5\pm(2i-1)2D/5$, - - - - - - zeros of sinc(x) at $-3D/5\pm(2i-1)2D/25$: (a) Gaussian beam apodization, $std=6D/5$; (b) diffracted beam for three focus conditions; (c) depleted

undiffracted beam; (d) normalized system frequency response, $f_{ij}(2D)=v_{slm}T_{slm}v_{dl}/\lambda F_1$.

Fig. 10. Normalized crosstalk performance under conditions of Fig. 8 with $f_{ij}=0.3v_{slm}T_{slm}v_{dl}/\lambda F_1$.

Fig. 11. Best measured system frequency response: (a) magnitude; (b) phase.

Fig. 12. System frequency response for various AO SLM input frequencies, • • • • • AO SLM freq.=60.0 MHz, x x x x AO SLM freq.=68.0 MHz, ———— AO SLM freq.=80.0 MHz, - • - • - AO SLM freq.=92.0 MHz, - - - - - AO SLM freq.=100.0 MHz.

Fig. 13. Simulated two-tap system frequency response: (a) narrow tap separation, ———— tap delay separation = 22 nsec, - - - - - - tap delay separation = 176 nsec, • • • • • tap delay separation = 88 ns; (b) wide tap separation, ———— tap delay separation = 352 nsec, - - - - - - tap delay separation = 572 nsec.

Fig. 14. Measured two-tap system frequency response: (a) narrow tap separation, ———— tap frequency separation = 1 MHz, - - - - - - tap frequency separation = 4 MHz, • • • • • tap frequency separation = 8 MHz; (b) wide tap separation, ———— tap frequency separation = 16 MHz, - - - - - - tap frequency separation = 26 MHz.

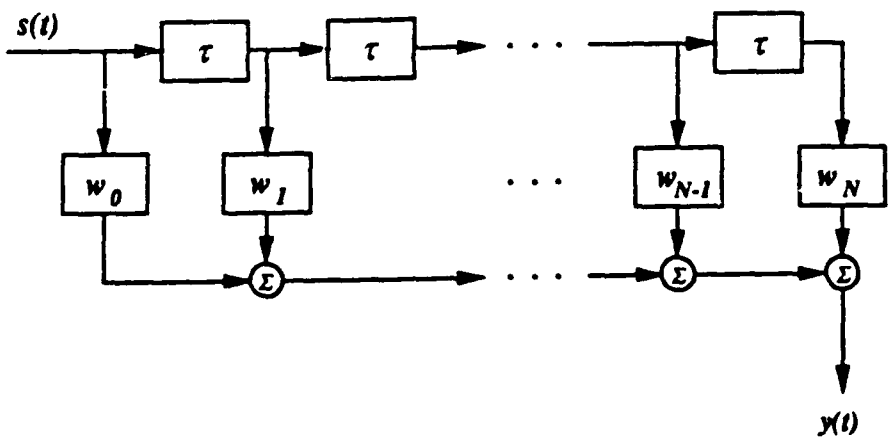

Fig. 1. Finite impulse response tapped delay line filter

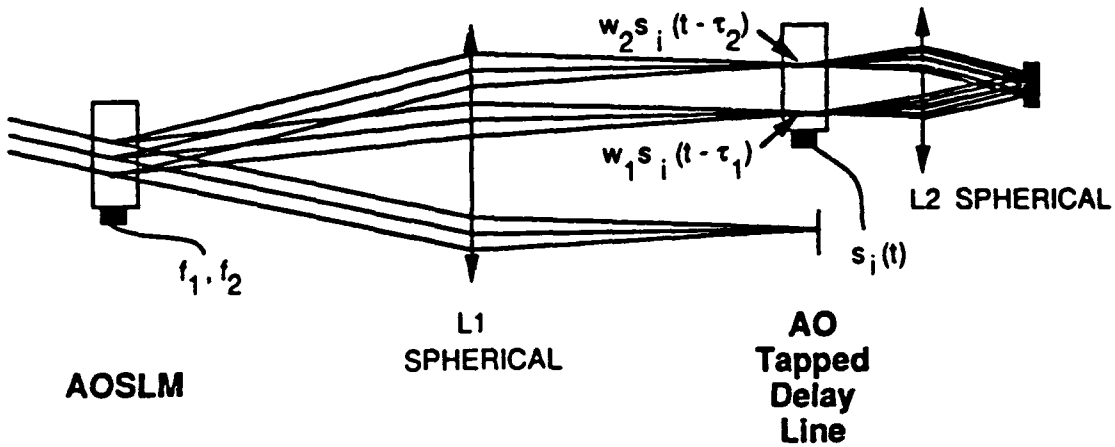

(a) Top view

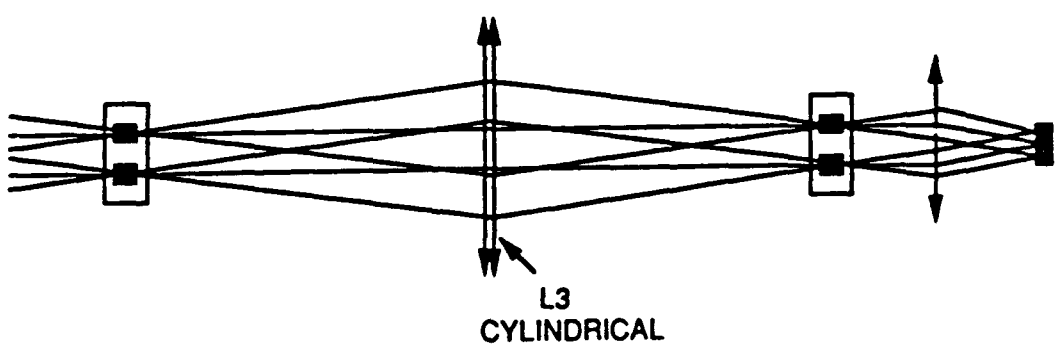

(b) Side view showing multichannel operation

Fig. 2. Two-Channel AO Tapped Delay Line Architecture

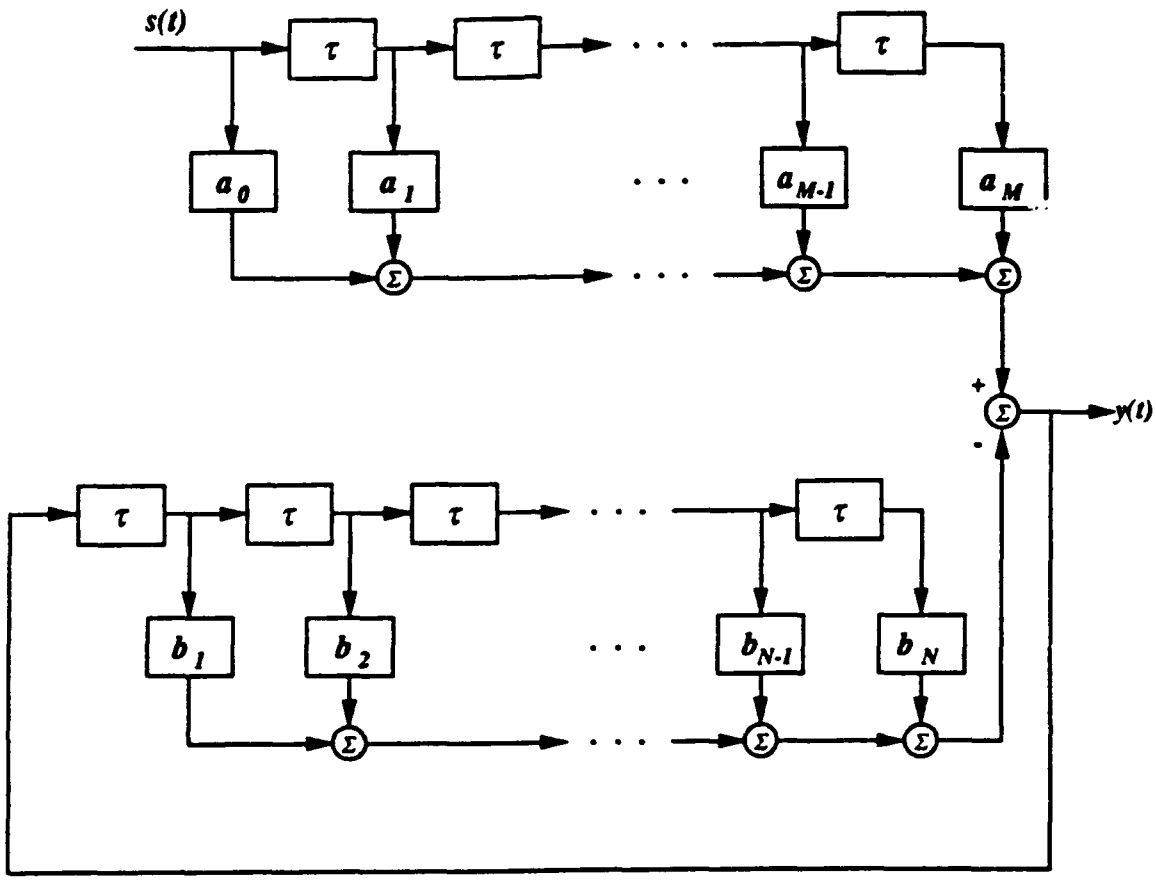

Fig. 3. Infinite impulse response tapped delay line filter

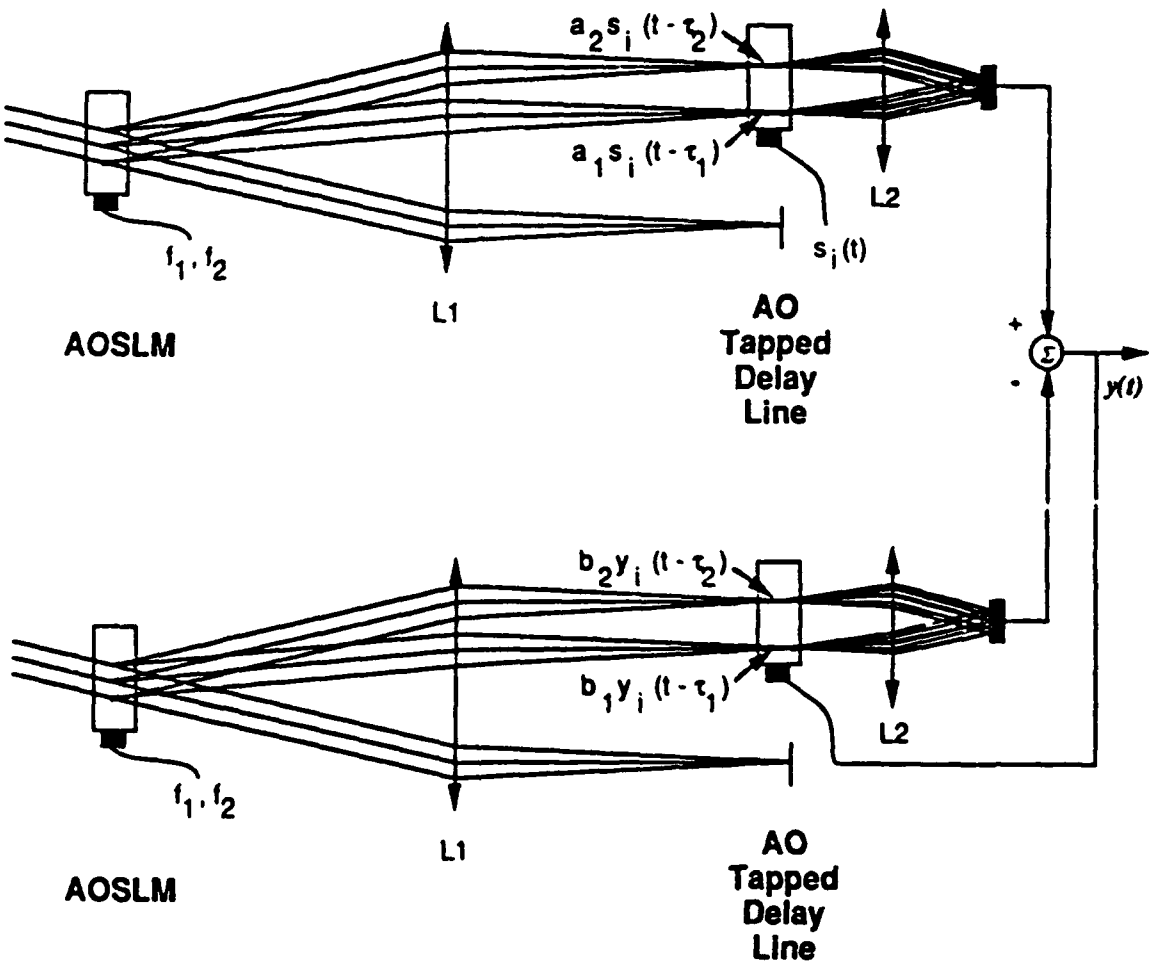

Fig. 4. AO implementation of IIR filter

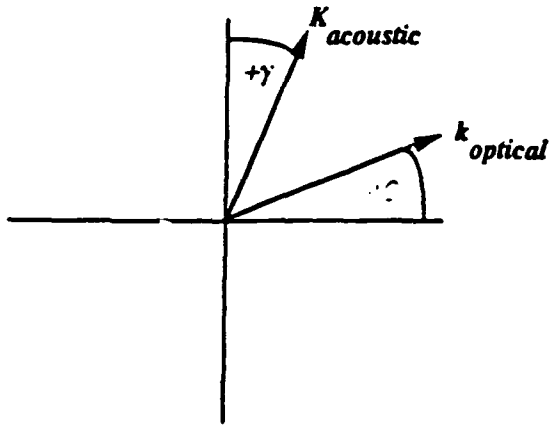

Fig. 5. Wavevector sign convention

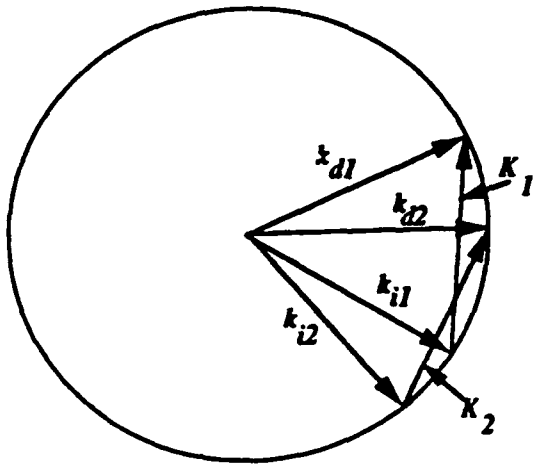

(a) Wavevector Diagram for a focused optical tap

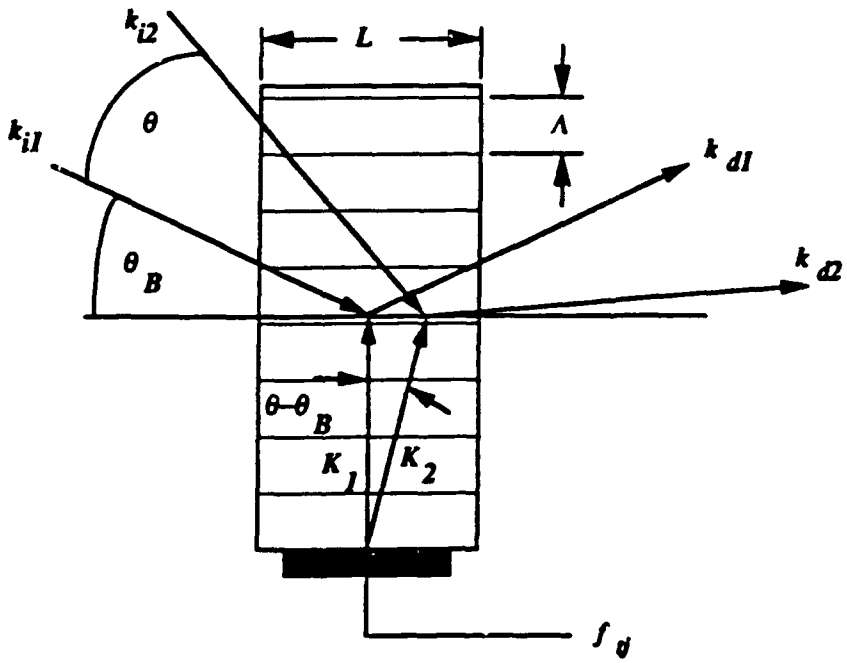

(b) Physical model of the AO cell

Fig. 6. Wavevectors for a focused optical input

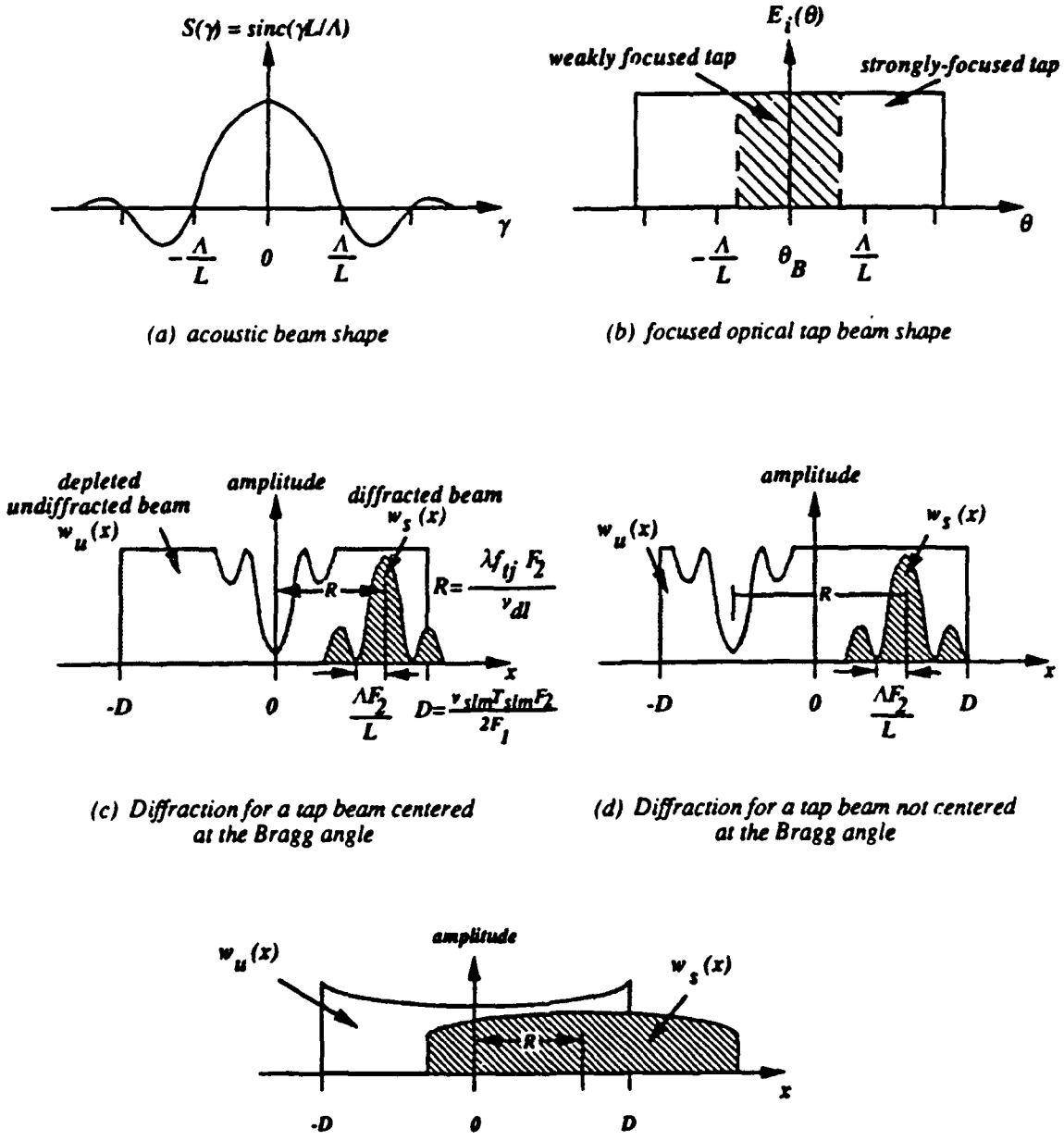

Fig. 7. Diffracted and undiffracted beam phenomenology

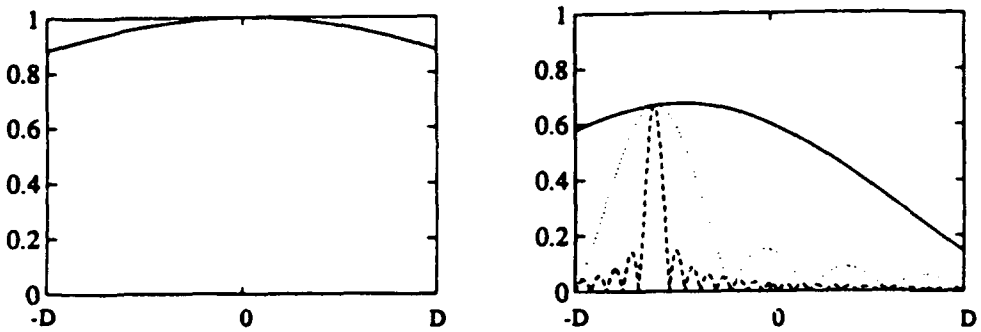

(a) Gaussian beam apodization, std=2D

(b) Diffracted beam for three focus conditions

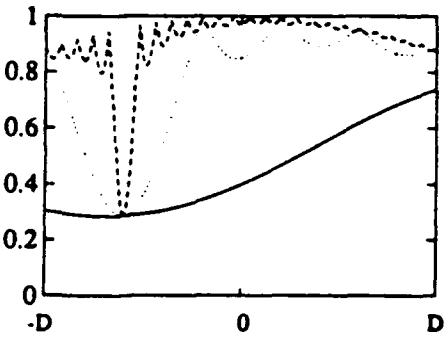

(c) Depleted undiffracted beam

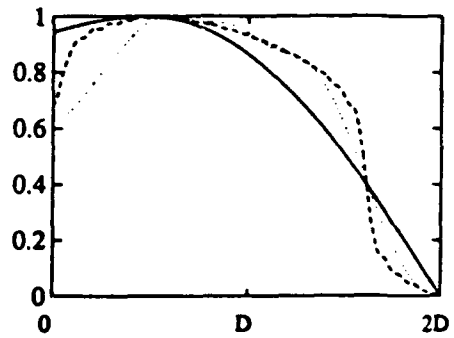

(d) Normalized system frequency response,

$$f_{tj}(2D)=v_{slm}T_{slm}v_{dl}/\lambda F_{l}$$

Fig. 8. Simulated diffracted and undiffracted beams and resulting system frequency response

——— *zeros of sinc(x) at -3D/5 ±(2i-1)2D*
..... *zeros of sinc(x) at -3D/5 ±(2i-1)2D/5*
- - - - - - - *zeros of sinc(x) at -3D/5 ±(2i-1)2D/25*

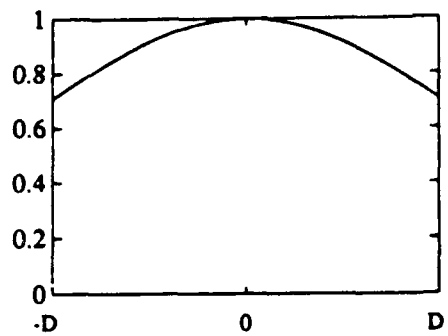

(a) Gaussian beam apodization, std=6D/5

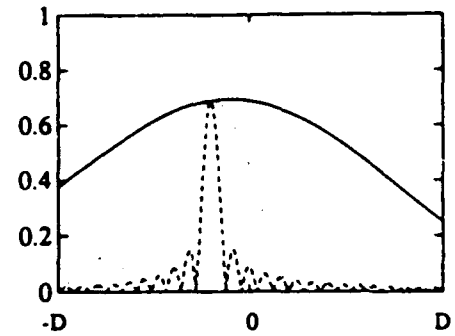

(b) Diffracted beam for three focus conditions

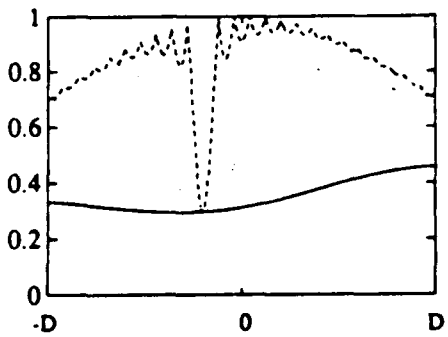

(c) Depleted undiffracted beam

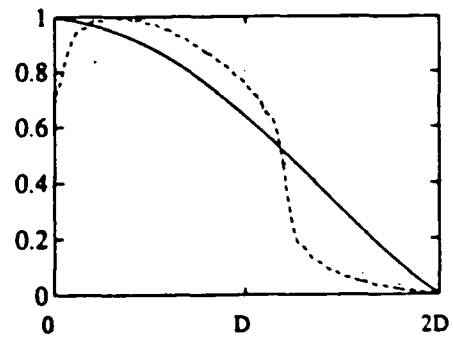

(d) Normalized system frequency response,

$f_{ij}(2D)=v_{slm}T_{slm}v_{dl}/\lambda F_1$

Fig. 9. Simulated diffracted and undiffracted beams and resulting system frequency response

——— *zeros of sinc(x) at -D/5 ±(2i-1)2D*
..... *zeros of sinc(x) at -D/5 ±(2i-1)2D/5*
- - - - - - - *zeros of sinc(x) at -D/5 ±(2i-1)2D/25*

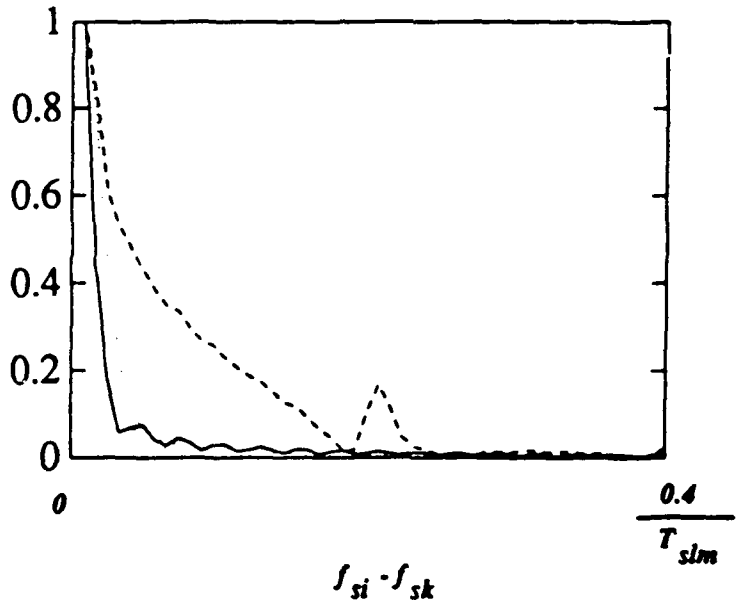

Fig. 10. Normalized crosstalk performance under conditions of Fig. 8 with $f_{ij} = 0.3 v_{slm} T_{slm} v_{dl} / \lambda F_l$

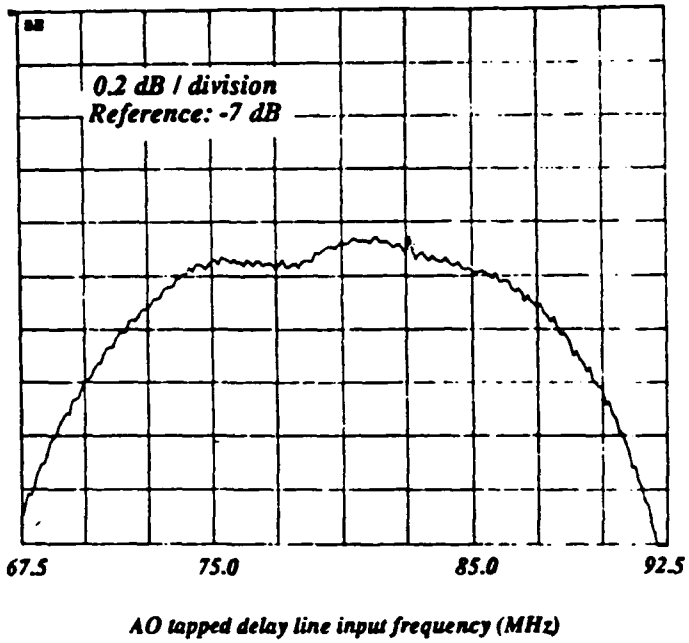

(a) Magnitude

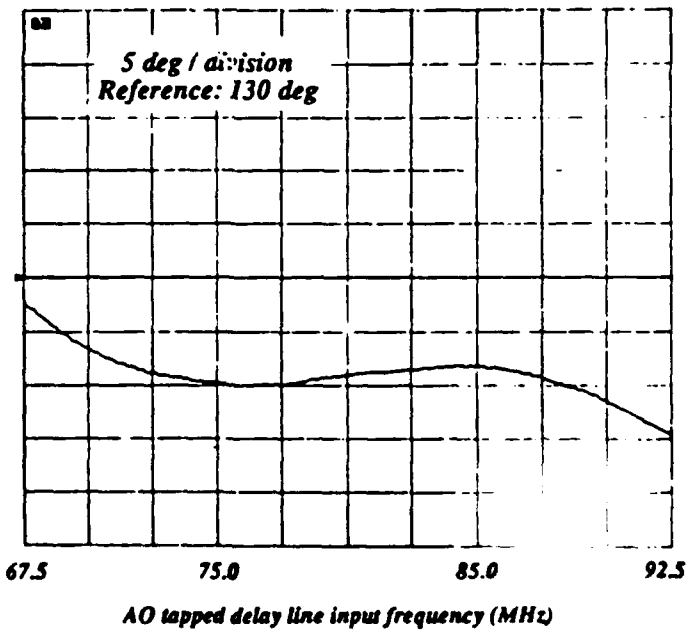

(b) Phase

Fig. 11. Best measured system frequency response

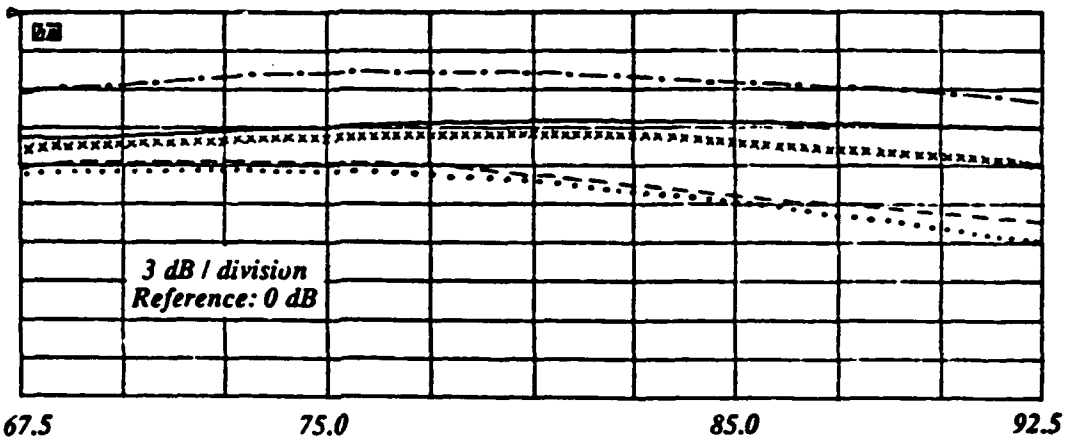

AO tapped delay line input frequency (MHz)

Fig. 12. System frequency response for various AO SLM input frequencies

• • • • • •	*AO SLM freq. = 60.0 MHz*
x x x x x	*AO SLM freq. = 68.0 MHz*
———	*AO SLM freq. = 80.0 MHz*
— · — · — ·	*AO SLM freq. = 92.0 MHz*
— — — — —	*AO SLM freq. = 100.0 MHz*

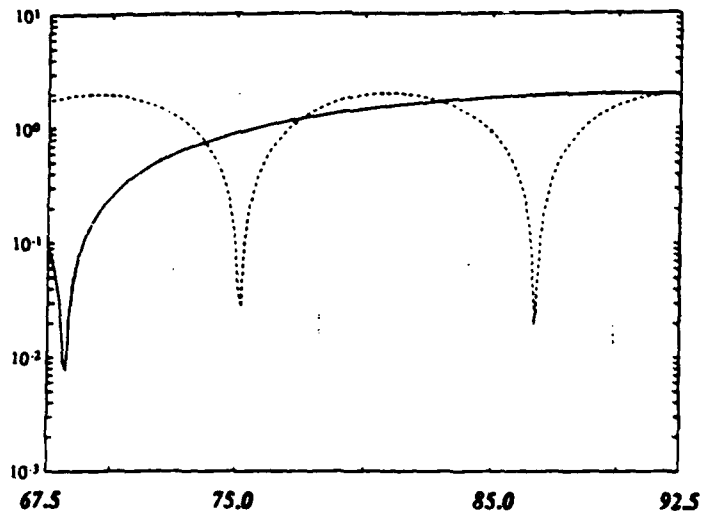

(a) Narrow tap separation: ——— *tap delay separation = 22 ns*
- - - - - - - *tap delay separation = 88 ns*
..... *tap delay separation = 176 ns*

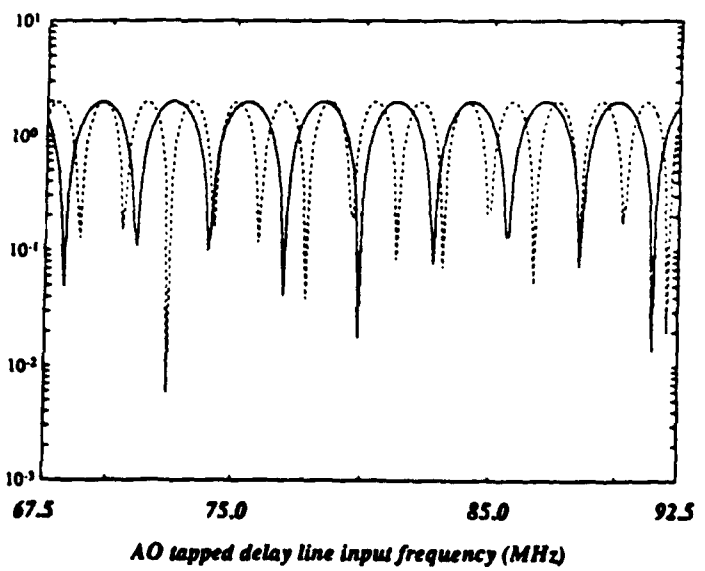

(b) Wide tap separation: ——— *tap delay separation = 352 ns*
- - - - - - - *tap delay separation = 572 ns*

Fig. 13. Simulated two-tap system frequency response

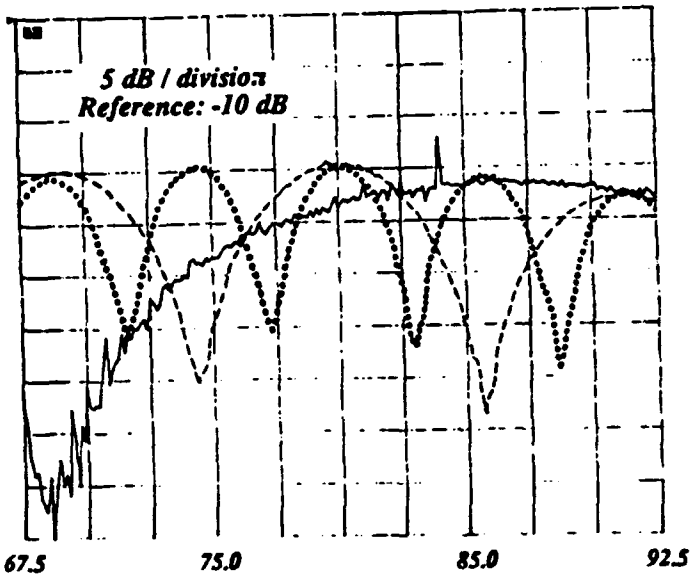

(a) Narrow tap separation: ——— *tap frequency separation = 1 MHz*
- - - - - - - *tap frequency separation = 4 MHz*
..... *tap frequency separation = 8 MHz*

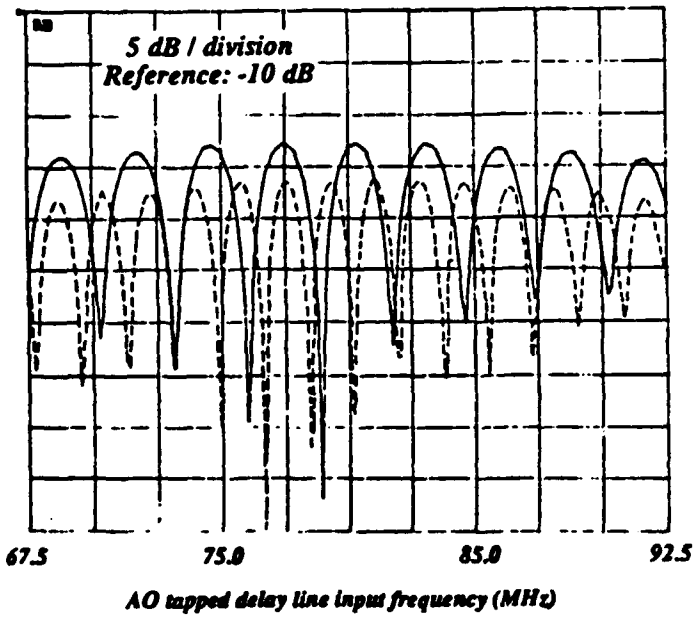

(b) Wide tap separation: ——— *tap frequency separation = 16 MHz*
- - - - - - - *tap frequency separation = 26 MHz*

Fig. 14. Measured two-tap system frequency response

APPENDIX C. MATLAB SOFTWARE

```
% Program lmsRLcorr
%
% This program adaptively filters a signal, r, to generate an estimate, dest,
% of the desired output, d.  The BLOCK-LMS filtering algorithm is employed,
% where integration of the correlation result is performed before the weight
% vector is updated.
%
% For this system identification problem, d is the output from a zero-only
% filter.  Therefore, when the output error is minimized, the adaptive filter
% best estimates the unknown zero-only filter.
%
% Variables required external are
%  mue, the step size
%  M, the number of iterations through the filter
%  R, the filter size (number of taps) is set to 100
%  x, the signal input (can be created using noisegen)
%    Constraint: M + R <= length of x
%
% Create a zero-only system representing multipath to the main channel
% We choose to use a 5-microsec window with each sample being 50 ns.
% Thus the total number of samples in the window is 100.
num=zeros(1:100);
delays=[60];
num(delays)=[.631];
%
% Create a zero-only system representing multipath to the auxiliary
num2=zeros(1:100);
delays2=[1,5,20];
num2(delays2)=[.251,.69,.8];

% Create the desired output, d
d=filter(num,1,x);
% Create the received auxiliary input, r
r=filter(num2,1,x);
%
% Initialize vectors
err=[];
w=[];
wcorr=[];
R=100;
%
% Initialize the filter weights to zero. Note that the
% first element of w is on the far right of the filter
w(1,R)=(0:0);
wcorr(1,R)=(0:0);
%
% Perform lms filtering beginning with a full filter
%
k=0;
for n=1:M
%
% Form the estimate and error signals
  dest(n)=w*r(n:n+R-1)';
  e=dest(n)-d(n+R-1);
%
%  w=w-mue*r(n:n+R-1)*e;
% Update the adaptive weight vector - BLOCK LMS
  wcorr=wcorr-mue*r(n:n+R-1)*e;
  if (n-1)/100==k
    w=wcorr;
    k=k+1;
  end
%
% Store the error squared
  err(n)=e*e;
%
end
%
% Plot the error squared versus iteration number
semilogy(err)
```

```
%program peakpk
%This program simulates the peak picking algorithm for the MADOP
%correlator weight calculation, and includes a measurment of the
%phase of the detected spatial carrier. The carrier frequency is
%'a' pixels per cycle, or equivalently 512/'a' cycles per 512-pixel
%window. The carrier phase at pixel 256 is 'phi', which is set by noting
%that the phase of carrier is linear in delay and IF frequency difference, %1/fif-1/a. fif
will be given as 512/400=1.28 (400 cycles per 5-microsecond, 512 %pixel window. The carrier
is multiplied by a correlation function with a %sinc(x) shape having unity magnitude
centered at 'offset' with zeros at %offset±ik, i=1,2,... The absolute value of this
function is then taken, and is %representative of the detected signal. With the IF
conversion from 80 MHz to %the new spatial carrier (around 15 MHz) the phase of the carrier
at the
%peak of the correlation will reveal the delay more accurately, as
%follows. Using a zero delay reference carrier, 'ref', which has a zero
%phase at zero delay (pixel 256), we can determine the phase of the
%non-zero delay carrier at the correlation peak. This is done through
%I&Q processing to yield correlation magnitude and phase.
%The phase is then used to determine the exact position using the equations
%delta=phase/2*pi*(1/1.28-1/a), and xnew=256+(p cycles of the 1/(1/fif-1/a)
%carrier)-delta. xnew is calculated for the two closest values of p, and the
%closest delay estimate to the tri-fit estimate is selected.

%%%%%variables requiring external definition are
%%%%% k: the width in pixels of the sinc(x) correlation function between zeros
%%%%% offset: the position of the correlation peak, in pixels
%%%%% a: the inverse of the spatial carrier frequency, in units of pixels/cycle

 clg
 axis([0 512 0 1]);
%create the two reference oscillators for I&Q processing
 ref=cos(2*pi*((1:512)-256)/a);
 ref2=sin(2*pi*((1:512)-256)/a);
%create the correlation function, assumed to be a sinc(x)
 corr=(k/pi)*sin(pi*((1:512)-offset)/k)./((1:512)-offset);
 corr(offset)=1;
%define the IF frequency [512pixels/(5 microseconds*80 MHz)]
 fif=1.28;
%calculate the expected phase offset due to conversion to a different IF
 phi=-2*pi*(offset-256)*(1/fif-1/a);
%create the carrier at the new IF @ 'a' pixels/cycle
 c=cos((2*pi*((1:512)-256)/a)+phi);
%create the carrier modulated correlation
 cbipolar=corr.*c;
%create the absolute value of the correlation and plot the whole window and a
%central region containing 3 central lobes of the sinc(x)
 c2=abs(cbipolar);
 subplot(221),plot(c2);title('correlation output')
 axis([offset-2*k offset+2*k 0 1]);
 subplot(222),plot(c2);title('region between central 4 zeros')
 axis;
%find the three peak positions and amplitudes
 [cmax1,indx1]=max(c2);
 if (indx1-k/4>0),
  c2(indx1-k/4:indx1+k/4)=zeros(1:k/2+1);
 else
  c2(1:indx1+k/4)=zeros(1:indx1+k/4);
 end
 [cmax2,indx2]=max(c2);
 if (indx2-k/4>0),
```

```
  c2(indx2-k/4:indx2+k/4)=zeros(1:k/2+1);
 else
  c2(1:indx2+k/4)=zeros(1:indx2+k/4);
 end
 [cmax3,indx3]=max(c2);
%calculate the slopes for the two lines going through the highest peak and the
%other peaks, and select the one having the largest slope magnitude
 slope1=abs((cmax1-cmax2)/(indx1-indx2));
 slope2=abs((cmax1-cmax3)/(indx1-indx3));
 if(slope2>slope1),
  y1=cmax1;
  x1=indx1;
  y2=cmax3;
  x2=indx3;
  y3=cmax2;
  x3=indx2;
 else
  y1=cmax1;
  x1=indx1;
  y2=cmax2;
  x2=indx2;
  y3=cmax3;
  x3=indx3;
 end
%calculate the position, x, and amplitude, y, for the equilateral triangle fit
%to the three points, and display the position and amplitude
 x=(x2*y1-x1*y2+y1*x3-y2*x3+y3*x1-y3*x2)/(2*y1-2*y2);
 y=(y1-y2)*x/(x1-x2)+(x1*y2-x2*y1)/(x1-x2);
 label= sprintf('peak amplitude =%6.3f, peak position =%6.3f',y,x);
 text(0.5,0.5,label,'sc')
%form the I and Q channels by (1) multiplying the bipolar correlation by the
%two reference oscillators, and (2) filtering out the sum terms by windowing in %the
frequency domain
 I=cbipolar.*ref;
 Q=cbipolar.*ref2;
 II=fft(I);
 QQ=fft(Q);
 II(512/a:512-512/a)=zeros(1:512-1024/a+1);
 QQ(512/a:512-512/a)=zeros(1:512-1024/a+1);
 I=ifft(II);
 Q=ifft(QQ);
%calculate the correlation magnitude and plot
 MAG=sqrt(abs(I).^2+abs(Q).^2);
 axis([0 512 0 max(MAG)]);
 subplot(223),plot(MAG);title('magnitude of correlation')
%calculate the correlation phase and plot the central three-lobe region
 phase=-atan2(Q,I);
 axis([offset-2*k offset+2*k -pi pi]);
 subplot(224),plot(phase);title('phase of correlation at correlation peak')
%calculate the delay from the center pixel (256), modulo 1/(1/fif-1/a), as a %function of
phase shift
 delta=phase(x)/(2*pi*(1/fif-1/a));
%calculate the nearer and further distance from the center pixel (256), in %cycles of
1/(1/fif-1/a), of the original delay estimate obtained through the %tri fit
 p1=ceil((x-256)*(1/fif-1/a));
 p2=floor((x-256)*(1/fif-1/a));
%calculate the new, more precise, value of the delay for the nearer and farther %estimates
p1 and p2, choose the result closest to the original tri-fit %estimate, and display the
result
 xnew1=256+p1/(1/fif-1/a)-delta;
```

```
xnew2=256+p2/(1/fif-1/a)-delta;
delx1=abs(xnew1-x);
delx2=abs(xnew2-x);
if (delx1>delx2),
 xnew=xnew2;
else
 xnew=xnew1;
end
label1= sprintf('phase at the correlation peak =%6.3f radians, precise delay =
%6.3f',phase(x),xnew);
text(0.0,0.0,label1,'sc')
label2= sprintf('a =%6.3f, k =%6.3f, offset =%6.3f',a,k,offset);
text(0.0,0.5,label2,'sc')
```

```
%program peakpk\154
%This program simulates the peak picking algorithm for the MADOP
%correlator weight calculation, and includes a measurment of the
%phase of the detected spatial carrier. The carrier frequency is
%'a' pixels per cycle, or equivalently 512/'a' cycles per 512-pixel
%window. The carrier phase at pixel 256 is 'phi', which is set by noting
%that the phase of carrier is linear in delay and IF frequency difference, %1/fif-1/a. fif
will be given as 512/400=1.28 (400 cycles per 5-microsecond, 512 %pixel window. The carrier
is multiplied by a correlation function with a %sinc(x) shape having unity magnitude
centered at 'offset' with zeros at %offset±ik, i=1,2,... The absolute value of this
function is then taken, and is %representative of the detected signal. With the IF
conversion from 80 MHz to %the new spatial carrier (around 15 MHz) the phase of the carrier
at the
%peak of the correlation will reveal the delay more accurately, as
%follows. Using a zero delay reference carrier, 'ref', which has a zero
%phase at zero delay (pixel 256), we can determine the phase of the
%non-zero delay carrier at the correlation peak. This is done through
%I&Q processing to yield correlation magnitude and phase.
%The phase is then used to determine the exact position using the equations
%delta=phase/2*pi*(1/1.28-1/a), and xnew=256+(p cycles of the 1/(1/fif-1/a)
%carrier)-delta. xnew is calculated for the two closest values of p, and the
%closest delay estimate to the tri-fit estimate is selected.

%%%%%variables requiring external definition are
%%%%% k: the width in pixels of the sinc(x) correlation function between zeros
%%%%% offset: the position of the correlation peak, in pixels
%%%%% a: the inverse of the spatial carrier frequency, in units of pixels/cycle

 clg
 axis([0 512 0 1]);
 rand('normal')
%create the two reference oscillators for I&Q processing
 ref=cos(2*pi*((1:512)-256)/a);
 ref2=sin(2*pi*((1:512)-256)/a);
%create the correlation function, assumed to be a sinc(x)
 corr=(k/pi)*sin(pi*((1:512)-offset)/k)./((1:512)-offset);
 corr(offset)=1;
 corr=corr+var*rand(1,512);
%define the IF frequency [512pixels/(5 microseconds*80 MHz)]
 fif=1.28;
%calculate the expected phase offset due to conversion to a different IF
 phi=-2*pi*(offset-256)*(1/fif-1/a);
%create the carrier at the new IF @ 'a' pixels/cycle
 c=cos((2*pi*((1:512)-256)/a)+phi);
%create the carrier modulated correlation
 cbipolar=corr.*c;
%create the absolute value of the correlation and plot the whole window and a
%central region containing 3 central lobes of the sinc(x)
 c2=abs(cbipolar);
 subplot(221),plot(c2);title('correlation output')
 axis([offset-2*k offset+2*k 0 1]);
 subplot(222),plot(c2);title('region between central 4 zeros')
 axis;
%find the three peak positions and amplitudes
 [cmax1,indx1]=max(c2);
 if (indx1-k/4>0),
  c2(indx1-k/4:indx1+k/4)=zeros(1:k/2+1);
 else
  c2(1:indx1+k/4)=zeros(1:indx1+k/4);
 end
```

```
 [cmax2,indx2]=max(c2);
 if (indx2-k/4>0),
  c2(indx2-k/4:indx2+k/4)=zeros(1:k/2+1);
 else
  c2(1:indx2+k/4)=zeros(1:indx2+k/4);
 end
 [cmax3,indx3]=max(c2);
%calculate the slopes for the two lines going through the highest peak and the
%other peaks, and select the one having the largest slope mag nitude
 slope1=abs((cmax1-cmax2)/(indx1-indx2));
 slope2=abs((cmax1-cmax3)/(indx1-indx3));
 if(slope2>slope1),
  y1=cmax1;
  x1=indx1;
  y2=cmax3;
  x2=indx3;
  y3=cmax2;
  x3=indx2;
 else
  y1=cmax1;
  x1=indx1;
  y2=cmax2;
  x2=indx2;
  y3=cmax3;
  x3=indx3;
 end
%calculate the position, x, and amplitude, y, for the equilateral triangle fit
%to the three points, and display the position and amplitude
 x=(x2*y1-x1*y2+y1*x3-y2*x3+y3*x1-y3*x2)/(2*y1-2*y2);
 y=(y1-y2)*x/(x1-x2)+(x1*y2-x2*y1)/(x1-x2);
 label= sprintf('peak amplitude =%6.3f, peak position =%6.3f',y,x);
 text(0.5,0.5,label,'sc')
%form the I and Q channels by (1) multiplying the bipolar correlation by the
%two reference oscillators, and (2) filtering out the sum terms by windowing in %the
frequency domain
 I=cbipolar.*ref;
 Q=cbipolar.*ref2;
 II=fft(I);
 QQ=fft(Q);
 II(512/a:512-512/a)=zeros(1:512-1024/a+1);
 QQ(512/a:512-512/a)=zeros(1:512-1024/a+1);
 I=ifft(II);
 Q=ifft(QQ);
%calculate the correlation magnitude and plot
 MAG=sqrt(abs(I).^2+abs(Q).^2);
 axis([0 512 0 max(MAG)]);
 subplot(223),plot(MAG);title('magnitude of correlation')
%calculate the correlation phase and plot the central three-lobe region
 phase=-atan2(Q,I);
 axis([offset-2*k offset+2*k -pi pi]);
 subplot(224),plot(phase);title('phase of correlation at correlation peak')
%calculate the delay from the center pixel (256), modulo 1/(1/fif-1/a), as a %function of
phase shift
 delta=phase(x)/(2*pi*(1/fif-1/a));
%calculate the nearer and further distance from the center pixel (256), in %cycles of
1/(1/fif-1/a), of the original delay estimate obtained through the %tri fit
 p1=ceil((x-256)*(1/fif-1/a));
 p2=floor((x-256)*(1/fif-1/a));
%calculate the new, more precise, value of the delay for the nearer and farther %estimates
p1 and p2, choose the result closest to the original tri-fit %estimate, and display the
```

```
result
 xnew1=256+p1/(1/fif-1/a)-delta;
 xnew2=256+p2/(1/fif-1/a)-delta;
 delx1=abs(xnew1-x);
 delx2=abs(xnew2-x);
 if (delx1>delx2),
  xnew=xnew2;
 else
  xnew=xnew1;
 end
 label1= sprintf('phase at the correlation peak =%6.3f radians, precise delay = %6.3f, var
=%6.3f ,phase(x),xnew,var);
 text(0.0,0.0,label1,'sc')
 label2= sprintf('a=%6.3f,k=%6.3f,offset=%6.3f',a,k,offset);
 text(0.0,0.5,label2,'sc')
```

```
% program overlap
% Creates an apodized abs(sinc) of magnitude b and length L
% centered at L-K with zeros at L-K±ia, i=1,2,...
% The apodization function is a gaussian with standard deviation std.
% The results are plotted for the externally supplied a, a/5, and a/25.
% The undiffracted beam is then created by subtracting the
% apodized abs(sinc) function from the apodization function.
% Correspondence to the Applied Optics paper is as follows:
% The width of the undiffracted beam, L, is given as the magnified
% image of the AO SLM aperture, L=v(slm)T(slm)(f4)/(f1)
% The position in the output plot is from 1 to L, and corresponds to
% the heterodyne efficiency as a function of diffraction angle, and
% therefore provides a measure of frequency response. The distance
% diffracted is given as lambdaF(j)(f4)/v(dl). At L, the frequency
% input to the AO tapped delay line is F(j)=v(dl)v(slm)T(slm)/(f1)lambda.
% This frequency response should be multiplied by the AO tapped delay
% line frequency response and the photodetector frequency response to
% obtain the overall frequency response.
% In addition, a tap position response will result due to the frequency
% response of the AO SLM, and the shape of the acoustic beam as a function
% of delay position (assumed to be a sinc as a function of angle and
% therefore independent of tap position).
%
 axis([0 L 0 1]);
 k=0;
 sinc=0;
 invsinc=0;
 output=0;
% Create AO SLM apodization, which is always centered on the undiffracted beam
 B=(1:L/2).*(1:L/2);
 var=std*std;
 apod=exp(-B/(2*var))/sqrt(2*pi*var);
 apod=apod/max(apod);
 apod(L/2+1:L)=apod;
 for i=1:L/2-1
   j(i)=apod(L/2-i);
 end
 apod(1:L/2-1)=j;
 apod(L/2)=1;
% Create abs(sinc) - diffracted beam
 sinc=abs((a/pi)*sin(pi*(1:K)/a)./(1:K));
 sinc(L-K+1:L)=sinc;
 for i=1:L-K-1
   k(i)=sinc(L-K-i);
 end
 sinc(1:L-K-1)=k;
 sinc(L-K)=1;
 sinc=b*sinc.*apod;
% Create undiffracted beam
 invsinc=apod-sinc;
 clg
%subplot(221),plot(apod)%;title(['AO SLM apodization, std=',num2str(std)])
% subplot(222),plot(sinc)%;title(['diffracted beam,
a=',num2str(a),',b=',num2str(b),',K=',num2str(K)])
% subplot(223),plot(invsinc)%;title(['depleted undiffracted beam',',std=',num2str(std)])
% Create the frequency response
% output=xcorr(invsinc,sinc);
 %output=output/max(output(L:2*L-1));
% subplot(224),plot(output(L:2*L-1))%;title('normalized frequency response')
% Calculate the impact of crosstalk
```

```
 sincd=0;
 sincd(F:L)=sinc(1:L-F+1);
 sincd=sincd.*invsinc;
 ct=fft(sincd);
 ct=ct/max(ct);
 ct=sqrt(real(ct).*real(ct)+imag(ct).*imag(ct));
 ct=ct/max(ct);
 axis([0 L/20 0 1]);
 subplot(221),plot(ct)%;title(['crosstalk vs. tap separation',',F=',num2str(F)])
 axis([0 L 0 1]);
% Run program for new value of a
 a=a/5;
 k=0;
 sinc=0;
 invsinc=0;
 output=0;
 sinc=abs((a/pi)*sin(pi*(1:K)/a)./(1:K))
 sinc(L-K+1:L)=sinc;
 for i=1:L-K-1
   k(i)=sinc(L-K-i);
 end
 sinc(1:L-K-1)=k;
 sinc(L-K)=1;
 sinc=b*sinc.*apod;
 invsinc=apod-sinc;
% subplot(222),plot(sinc,':');
 %subplot(223),plot(invsinc,':');
 %output=xcorr(invsinc,sinc);
 %output=output/max(output(L:2*L-1));
 %subplot(224),plot(output(L:2*L-1),':')
% Calculate the impact of crosstalk
 sincd=0;
 sincd(F:L)=sinc(1:L-F+1);
 sincd=sincd.*invsinc;
 ct=fft(sincd);
 ct=ct/max(ct);
 ct=sqrt(real(ct).*real(ct)+imag(ct).*imag(ct));
 ct=ct/max(ct);
 axis([0 L/20 0 1]);
 subplot(221),plot(ct,':')
 axis([0 L 0 1]);
% Run program for new value of a
 a=a/5;
 k=0;
 sinc=0;
 invsinc=0;
 output=0;
 sinc=abs((a/pi)*sin(pi*(1:K)/a)./(1:K));
 sinc(L-K+1:L)=sinc;
 for i=1:L-K-1
   k(i)=sinc(L-K-i);
 end
 sinc(1:L-K-1)=k;
 sinc(L-K)=1;
 sinc=b*sinc.*apod;
 invsinc=apod-sinc;
% subplot(222),plot(sinc,'—');
 %subplot(223),plot(invsinc,'—');
 %output=xcorr(invsinc,sinc);
 %output=output/max(output(L:2*L-1));
```

```
%subplot(224),plot(output(L:2*L-1),'--')
a=25*a;
% Calculate the impact of crosstalk
sincd=0;
sincd(F:L)=sinc(1:L-F+1);
sincd=sincd.*invsinc;
ct=fft(sincd);
ct=sqrt(real(ct).*real(ct)+imag(ct).*imag(ct));
ct=ct/max(ct);
axis([0 L/20 0 1]);
subplot(221),plot(ct,'--')
axis([0 L 0 1]);
end
```

```
%phase error program
%create 80 MHz sinusoid over 25 ns (2 cycles) at a 0.05 ns sample rate
sinusoid=0;
errorsq=0;
error=0;
sinusoid=sin(0.008*pi*(1:500));
%calculate square of magnitude of sinusoid for varying phase error
%where the phase is varied 250 steps over 360 deg (250 steps equals
%1/80MHz at the 0.05 ns sampling resolution)
for i=1:250
 error=sinusoid-sin(.008*pi*(1+i:500+i));
 errorsq(i)=max(error)*max(error);
end
clg
subplot(211),plot(errorsq);title('error squared of cancelled signal, 1deg=0.69 samples')
errorsq=errorsq/max(errorsq);
subplot(212),semilogy(errorsq(1:20));title('magnification of error squared')
label= sprintf('Rel power at 1.44deg = %6.5f, at 2.88deg = %6.5f, at 4.32deg =
%6.5f',errorsq(1),errorsq(2),errorsq(3));
text(0.1,0.5,label,'sc')

end
```

```
%program AOTDL
axis([67500000 92500000 -3 1]);
%k=43;
%b=zeros(1:k);
%b=[1,b,1];
%[h,w]=freqz(b,1,8192);
%mm=abs(h);
%ww=1000000000*w/pi;
%k=172;
%b=zeros(1:k);
%b=[1,b,1];
%[h,w]=freqz(b,1,8192);
%mmm=abs(h);
%www=1000000000*w/pi;
%k=344;
%b=zeros(1:k);
%b=[1,b,1];
%[h,w]=freqz(b,1,8192);
%mmmm=abs(h);
%wwww=1000000000*w/pi;
%semilogy(ww,mm,'-',www,mmm,'—',wwww,mmmm,':')
k=688;
b=zeros(1:k);
b=[1,b,1];
[h,w]=freqz(b,1,8192);
mm=abs(h);
ww=1000000000*w/pi;
k=1118;
b=zeros(1:k);
b=[1,b,1];
[h,w]=freqz(b,1,8192);
mmm=abs(h);
www=1000000000*w/pi;
semilogy(ww,mm,'-',www,mmm,'—')
```

```
%program corrfilt
%takes a carrier-modulated waveform and smooths it to attain a peak
%assume 50 cycles of carrier across array
clg
window=[];
%select a waveform type: 1=dsb-sc two-tone; 2=sinx/x pulse
waveform=2;
%select a filter type: 1=convolution with truncated sinx/x;
% 2=square filter in frequency domain; 3=butterworth filter
filttype=2;
%add a phase shift to carrier
phserr=0;
if waveform==1
% Assumes 6.5 cycles of waveform
  phs=0;
  R=sin(2*pi*([1:512]+phs)./78.77).*sin(2*pi*([1:512]+phserr)./10.24);
else
%define sinc width and position
  k=20;
  offset=240;
  pulse=(k/pi)*sin(pi*((1:512)-offset)/k)./((1:512)-offset);
  pulse(offset)=1;
  R=pulse.*sin(2*pi*([1:512]+phserr)./10.24);
end
R=abs(R);
subplot(221),plot(R);title('correlator output')
if filttype==1
%length of window is 2*N+1
  N=10;
  K=abs(fft([ones(1:50),zeros(1:462)]));
  window=[K(512-N+1:512),K(1:N+1)];
  Rfilt=conv(R,window);
end
if filttype==2
%define width of filter
  W=50;
  Rfftfilt=fft(R).*[ones(1:W),zeros(1:512-2*W),ones(1:W)];
  Rfilt=abs(ifft([Rfftfilt(1:256),zeros(1:512),Rfftfilt(257:512)]));
end
if filttype==3
  [b1,a1]=butter(5,2/10);
  Rfilt=filtfilt(b1,a1,R);
end
subplot(222),plot(Rfilt);title('filtered correlator output')
%subplot(223),plot(abs(fft(R)));title('spectrum of correlator output')
%wind=[window,zeros(1:512-2*N)];
%subplot(224),plot(abs(fft(wind)));title('spectrum of window function')
%subplot(224),plot([ones(1:50),zeros(1:412),ones(1:50)]);title('spectrum of
window function')

%select peak and perform tri-fit
[Rmax,indx]=max(Rfilt);
%calculate the slopes for the two lines going through the highest peak and the
%other peaks, and select the one having the largest slope magnitude
 slope1=abs((Rmax-Rfilt(indx-1)));
 slope2=abs((Rmax-Rfilt(indx+1)));
 if(slope2>slope1),
  y1=Rmax;
  x1=indx;
  y2=Rfilt(indx+1);
```

```
  x2=indx+1;
  y3=Rfilt(indx-1);
  x3=indx-1;
 else
  y1=Rmax;
  x1=indx;
  y2=Rfilt(indx-1);
  x2=indx-1;
  y3=Rfilt(indx+1);
  x3=indx+1;
 end
%calculate the position, x, and amplitude, y, for the equilateral triangle fit
%to the three points, and display the position and amplitude
 x=(x2*y1-x1*y2+y1*x3-y2*x3+y3*x1-y3*x2)/(2*y1-2*y2);
 y=(y1-y2)*x/(x1-x2)+(x1*y2-x2*y1)/(x1-x2);
 label= sprintf('peak amplitude =%6.3f, peak position =%6.3f',y,x/2);
 text(0.5,0.5,label,'sc')

%iterate through a number of carrier phases to determine sensitivity to carrier
for i=1:100
  phserr=i/10;
 if waveform==1
   R=sin(2*pi*([1:512]+phs)./78.77).*sin(2*pi*([1:512]+phserr)./10.24);
 else
   R=pulse.*sin(2*pi*([1:512]+phserr)./10.24);
 end
 R=abs(R);
 if filttype==1
   Rfilt=conv(R,window);
 end
 if filttype==2
   Rfftfilt=fft(R).*[ones(1:W),zeros(1:512-2*W),ones(1:W)];
   Rfilt=abs(ifft([Rfftfilt(1:256),zeros(1:512),Rfftfilt(257:512)]));
 end
 if filttype==3
   Rfilt=filtfilt(bl,al,R);
 end
 [Rmax,indx]=max(Rfilt);
 slope1=abs((Rmax-Rfilt(indx-1)));
 slope2=abs((Rmax-Rfilt(indx+1)));
 if(slope2>slope1),
  y1=Rmax;
  x1=indx;
  y2=Rfilt(indx+1);
  x2=indx+1;
  y3=Rfilt(indx-1);
  x3=indx-1;
 else
  y1=Rmax;
  x1=indx;
  y2=Rfilt(indx-1);
  x2=indx-1;
  y3=Rfilt(indx+1);
  x3=indx+1;
 end
 x=(x2*y1-x1*y2+y1*x3-y2*x3+y3*x1-y3*x2)/(2*y1-2*y2);
 y=(y1-y2)*x/(x1-x2)+(x1*y2-x2*y1)/(x1-x2);
 ampl(i)=y*2;
 pos(i)=x/2;
end
```

```
subplot(223),plot(ampl);title('tap amplitude vs. phase error')
subplot(224),plot(pos);title('tap position vs. phase error')
```

```
%program SLC
%this program makes phase of carrier equal at output of AOTDL to the carrier
%of the main channel using adaptive feedback
clg
%select a waveform type: 1=dsb-sc two-tone; 2=sinx/x pulse
waveform=2;
%select a filter type: 1=convolution with truncated sinx/x;
% 2=square filter in frequency domain; 3=butterworth filter
filttype=3;
%create the main channel signal
%add a phase shift to carrier
phserr=0;
if waveform==1
% Assumes 6.5 cycles of waveform
  phs=0;
  R1=sin(2*pi*([1:512]+phs)./78.77).*sin(2*pi*([1:512]+phserr)./10.24);
else
%define sinc width and position
  k=40;
  offset=240;
  pulse=(k/pi)*sin(pi*((1:512)-offset)/k)./((1:512)-offset);
  pulse(offset)=1;
  R1=pulse.*sin(2*pi*([1:512]+phserr)./10.24);
end

%begin loop to calculate results for various carrier phases
%create the AOTDL output signal
for i=1:100
%add a phase shift to carrier
  phserr=i/10;
  if waveform==1
    R2=sin(2*pi*([1:512]+phs)./78.77).*sin(2*pi*([1:512]+phserr)./10.24);
  else
    R2=pulse.*sin(2*pi*([1:512]+phserr)./10.24);
  end
%obtain cancelled signal
  S=R1-R2;
  detS=S.*S;
%filter the signal
  [b1,a1]=butter(5,1/50);
  detSfilt=filtfilt(b1,a1,detS);
%plot results for first iteration
  if i==1
    subplot(221),plot(R1);title('main channel signal')
    subplot(222),plot(detS);title('detected cancelled signal')
    subplot(223),plot(detSfilt);title('filtered residue')
  end
  voltage(i)=mean(detSfilt);
end
subplot(224),plot(voltage);title('output control voltage vs. phase')
```

```
%program SLCfilters
%this program makes phase of carrier equal at output of AOTDL to the carrier
%of the main channel using adaptive feedback
clg
%select a waveform type: 1=dsb-sc two-tone; 2=sinx/x pulse
waveform=2;
%select a filter type: 1=convolution with truncated sinx/x;
% 2=square filter in frequency domain; 3=butterworth filter
filttype=3;
%create the main channel signal
%add a phase shift to carrier
phserr=0;
if waveform==1
% Assumes 6.5 cycles of waveform
  phs=0;
  R1=sin(2*pi*([1:512]+phs)./78.77).*sin(2*pi*([1:512]+phserr)./10.24);
else
%define sinc width and position
  k=40;
  offset=240;
  pulse=(k/pi)*sin(pi*((1:512)-offset)/k)./((1:512)-offset);
  pulse(offset)=1;
  pulse=[pulse,pulse,pulse,pulse];
  R1=pulse.*sin(2*pi*([1:2048]+phserr)./10.24);
end
  subplot(221),plot(R1);title('main channel signal')

%begin loop to calculate results for various carrier phases
%create the AOTDL output signal
for i=1:3
%add a phase shift to carrier
  phserr=(i-1)*2.5;
  if waveform==1
    R2=sin(2*pi*([1:512]+phs)./78.77).*sin(2*pi*([1:512]+phserr)./10.24);
  else
    R2=pulse.*sin(2*pi*([1:2048]+phserr)./10.24);
  end
%obtain cancelled signal
  S=R1-R2;
  detS=S.*S;
%filter the signal
   [b1,a1]=butter(5,1/100);
   detSfilt=filtfilt(b1,a1,detS);
   if i==1
    subplot(222),plot(detSfilt);title('filtered residue,phserr=0')
   end
   if i==2
    subplot(223),plot(detSfilt);title('filtered residue,phserr=2.5')
   end
   if i==3
    subplot(224),plot(detSfilt);title('filtered residue,phserr=5')
  end
end
```

REFERENCES

1. Budge, M. C., R. J. Berinato, M. C. Zari, "Acousto-Optic Applications for Multichannel Adaptive Optical Processor," Final Technical Report, RL-TR-92-160, June 1992.

2. Ward, M. C., C. W. Keefer, and S. T. Welstead, "Adaptive Optical Processor," In-House Report, RL-TR-91-270, August 1991.

3. Welstead, S. T., and M. J. Ward,"Hybrid Electro-Optic Processor," Final Technical Report, RL-TR-91-164, July 1991.

4. Welstead, S. T., "Optical Processor Evaluation," Final Technical Report, RL-TR-91-34, March 1991.

5. Zari, M.C., R.J. Berinato, M.J. Ward, H.G. Andrews, "Multichannel Optical Time-Integrating Correlator for Adaptive Jamming Cancellation," SPIE Vol. 1704, Advances in Optical Information Processing V, p. 88, 1992.

6. Haykin, S., Adaptive Filter Theory, Prentice Hall, 1986.

7. Compton, R. T., Jr., Adaptive Antennas: Concepts and Performance, Prentice Hall, 1988

8. National Semiconductor, "Data Acquisition Linear Devices Databook," 1989.

9. National Semiconductor, "General Purpose Linear Devices Databook," 1989.

☆U.S. GOVERNMENT PRINTING OFFICE 1993-710-091-60259

MISSION

OF

ROME LABORATORY

Rome Laboratory plans and executes an interdisciplinary program in research, development, test, and technology transition in support of Air Force Command, Control, Communications and Intelligence (C^3I) activities for all Air Force platforms. It also executes selected acquisition programs in several areas of expertise. Technical and engineering support within areas of competence is provided to ESD Program Offices (POs) and other ESD elements to perform effective acquisition of C^3I systems. In addition, Rome Laboratory's technology supports other AFSC Product Divisions, the Air Force user community, and other DOD and non-DOD agencies. Rome Laboratory maintains technical competence and research programs in areas including, but not limited to, communications, command and control, battle management, intelligence information processing, computational sciences and software producibility, wide area surveillance/sensors, signal processing, solid state sciences, photonics, electromagnetic technology, superconductivity, and electronic reliability/maintainability and testability.